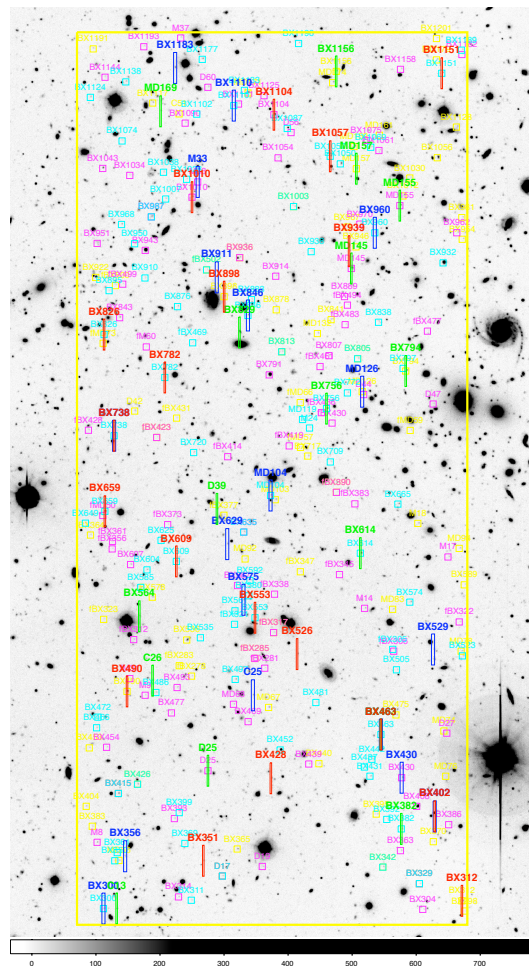


MOBIE Operational Concepts Definition Document (v1.7)

TMT.INS.DRD.08.004.DRF01

Charles Steidel (Caltech), Roberto Abraham (U.of Toronto),
Jarle Brinchmann (Leiden), Rebecca Bernstein (UCSC),
Judith Cohen (Caltech), Sandra Faber (UCSC),
Raja Guhathakurta (UCSC), Jasonjot Kalirai (STScI),
Gerry Luppino (UH/IfA), Jason X. Prochaska (UCSC),
Connie Rockosi (UCSC), Alice Shapley (UCLA)



December 5, 2008

Revision	Date	Author	Description
0.0	Nov 20 2008	CCS	Initial draft
0.1	Nov 26 2008	CCS	Added new science cases, re-did intro, requirements section, began revising old science cases
1.3	Dec 1 2008	CCS	Edited science cases, requirements sec., intro
1.5	Dec 3 2008	CCS	First complete version; distributed for comment
1.6	Dec 3 2008	CCS	Incorp. changes/fixes from JLC, B. Bigelow
1.7	Dec 5 2008	CCS	Incorp. comments from JXP, fixed some refs

Contents

1	Introduction	4
1.1	Acronyms	5
1.2	Acknowledgments	5
2	MOBIE Concept: Instrument Description	6
2.1	Scientific Priorities and Practical Considerations	6
2.2	MOBIE Concept Overview	6
2.3	Summary of Requirements	9
2.3.1	Modes of operation	9
2.3.2	Instrument Control	9
2.3.3	Mask System	9
2.3.4	Multi-slit mask Target Acquisition	9
2.3.5	Slit-viewing and Single-object Target Acquisition	9
2.3.6	Additional Modes	10
2.3.7	Wavelength Range	10
2.3.8	Dichroic Beam-Splitter	10
2.3.9	Filter System	10
2.3.10	Field of view	10
2.3.11	Spectral Resolution	11
2.3.12	Wavelength coverage	11
2.3.13	Image quality	12
2.3.14	Atmospheric Dispersion Corrector	12
2.3.15	PSF uniformity and stability	12
2.3.16	Field distortion	12
2.3.17	Throughput	12
2.3.18	Observing efficiency	12
2.3.19	Guiding and Wavefront Sensing	13
2.3.20	Instrument Rotator Performance	13
2.3.21	Instrument Flexure	13
2.3.22	Sensitivity	13
2.3.23	Stray Light Control	13
2.3.24	Detector Characteristics and Special Observing Modes	13
2.3.25	Requirements Related to Direct Imaging	14
2.3.26	Facility Requirements	14
3	Sample Observing Scenarios	15
3.1	Stellar Evolution and White Dwarfs	15
3.1.1	Background	15
3.1.2	Specific science goals	17
3.1.3	Observations and Targets	17
3.1.4	Pre-imaging	18
3.1.5	Technical Remarks and Mask Design	18
3.1.6	Path to Science	18
3.2	Metal Poor Stars: Galaxy Formation from the Stellar Halo of the Milky Way	21
3.2.1	Key Observable: Chemical Abundance Patterns in Distant Metal Poor Stars	21
3.2.2	Sample Selection	21
3.2.3	Pre-imaging	22
3.2.4	Mask Design	22
3.2.5	Required Integration Time	22
3.2.6	Target Acquisition	23
3.2.7	Calibration Data Acquisition	23

3.2.8	Facility Requirements	23
3.3	Resolved Stellar Populations in the Local Group	24
3.3.1	Background	24
3.3.2	Planning of observations	24
3.3.3	Pre-imaging	26
3.3.4	Mask design	26
3.3.5	Procedures during the day	26
3.3.6	Procedures during twilight	26
3.3.7	Target acquisition	26
3.3.8	Target science data acquisition	26
3.3.9	Calibration data acquisition	26
3.3.10	Facility requirements	27
3.4	The Dark Matter Distribution in Nearby Elliptical Galaxies	31
3.4.1	Background	31
3.4.2	Planning of observations	32
3.4.3	Pre-imaging	34
3.4.4	Mask design	34
3.4.5	Procedures during the day	35
3.4.6	Procedures during twilight	35
3.4.7	Target acquisition	35
3.4.8	Target science data acquisition	35
3.4.9	Calibration data acquisition	35
3.4.10	Facility requirements	35
3.5	Three-Dimensional Baryonic Structure During the Epoch of Galaxy Formation	38
3.5.1	Background	38
3.5.2	Specific science goals	39
3.5.3	Planning of observations	40
3.5.4	Pre-imaging	41
3.5.5	Mask design	42
3.5.6	Procedures during the day	43
3.5.7	Procedures during twilight	43
3.5.8	Target acquisition	43
3.5.9	Target science data acquisition	43
3.5.10	Calibration data acquisition	43
3.5.11	Additional requirements	43
3.6	The Stellar and Gaseous Content of L^* Galaxies at $z \sim 2 - 5$	47
3.6.1	Specific Science Goals	47
3.6.2	Planning of Observations	48
3.6.3	Target Selection	48
3.6.4	Spectral resolution	48
3.6.5	Wavelength coverage	49
3.6.6	Required integration time	49
3.6.7	Mask design	49
3.7	QSO Pairs: Revealing AGN and Massive Galaxy Formation at $z > 2$	50
3.7.1	Scientific Justification and Background	50
3.7.2	Key observable: Absorption-line spectroscopy of metal-line transitions	51
3.7.3	Sample selection	51
3.7.4	Pre-imaging	51
3.7.5	Mask design	51
3.7.6	Required integration time	51
3.7.7	Target acquisition	51
3.7.8	Calibration data acquisition	51

3.7.9	Facility requirements	52
3.8	Transients: Studying things that go bump in the night	53
3.8.1	Scientific Justification and Background	53
3.8.2	Key observable	54
3.8.3	Sample selection	54
3.8.4	Pre-imaging	54
3.8.5	Mask design	54
3.8.6	Required integration time	55
3.8.7	Target acquisition	55
3.8.8	Calibration data acquisition	55
3.8.9	Facility requirements	55
4	General Calibration Procedures	56
4.1	Sky subtraction with MOBIE	56
4.2	Geometric distortion	57
4.3	Flat-field and bias	57
4.4	Wavelength calibration	57
4.5	Flux calibration	58
4.6	Linearity	58
4.7	Dark current	58
4.8	Telluric absorption	58
5	Additional Observing Modes for MOBIE	59
5.1	A Tunable Narrow-Band Filter for TMT/MOBIE	59
5.1.1	Basic description of the tunable filter	59
5.1.2	Observing Scenario: The Topology of Reionization	59
5.1.3	Sample selection	59
5.1.4	Spectral Resolution	60
5.1.5	Integration Time	60
5.1.6	Procedures during the day	61
5.1.7	Procedures during twilight	61
5.1.8	Target acquisition	61
5.1.9	Calibration data acquisition	61
5.1.10	Facility requirements	61
5.1.11	Options for a more versatile filter	61
5.2	Image Slicer/Integral Field Unit	62
5.3	Ground Layer Adaptive Optics	62
6	Summary	65
7	References	66

1 Introduction

This document presents selected science drivers for a proposed Wide-Field Optical Spectrograph (WFOS) for the Thirty Meter Telescope (TMT). It relates the science requirements to the instrument concepts under consideration. It also identifies the key operational scenarios, outlines observation procedures, and describes the required interactions between WFOS/MOBIE, the telescope system, and the observatory. This document's structure, as well as a significant fraction of the science cases, is based on the WFOS OCDD presented as part of a previous feasibility study (Abraham et al 2005, TMT.INS.DRD.05.002.DRF01), completed in September 2005.

Since the time of the previous WFOS study, some of the scientific requirements have been either clarified or changed to reflect better knowledge of the notional budget allocated for a WFOS instrument within the TMT construction budget, since WFOS has been selected by the Science Advisory Committee (SAC) as one of the 3 initial ("Early Light") instruments and was included in the overall TMT construction budget determined in 2006. The new WFOS concept is called "MOBIE", to distinguish it from the WFOS/HIA concept from the fall of 2005. Considerable emphasis has been placed on avoiding mechanical and optical complexity whenever possible, as well as on producing an instrument concept whose science reach accounts for the fact that a high-resolution echelle spectrometer will not be available at first light. In fact, MOBIE will be the only instrument designed for seeing-limited use in the optical that will be available for at least the first several years of TMT operations.

The operational scenarios are described in sufficient detail so that a technical judgment on their feasibility can be made. The cases are presented at a level that is intended to be intelligible to a non-astronomically-expert but scientifically literate systems engineer (our target audience).

A brief description of the main features of the MOBIE concept is given in § 2, with a summary of requirements that flow down from the consideration of the WFOS/MOBIE science cases. More detailed descriptions can be found in the FPRD and MOBIE Feasibility Study Report.

The sample observing scenarios which form the heart of this document are given in § 3. It is important to note that the science cases in this Section were purposely chosen to stretch the design envelope for MOBIE and to exercise most of the modes of the instrument, rather than attempting to anticipate all of the most important science that will be undertaken with MOBIE ten years in the future. In choosing science cases an attempt was also made to select example programs that are unlikely to be achievable in the next decade with any existing (or planned) ground-based or space-based facility. To avoid needless repetition, those aspects of the observing scenarios that are common to all science cases (such as global calibrations) are dealt with in § 4. Discussion of possible "add-on" modes of operation, including GLAO, tunable filters, and IFUs, is contained in § 5. An attempt to summarize Sections 3 and 4 into a requirements flow-down is presented in Section 6.

MOBIE has been designed as a general purpose instrument with a broad range of capabilities, but of course the design of any large spectrograph requires that choices be made when optimizing the instrument. Several optical layouts have been considered as part of the MOBIE feasibility study, including a design supporting multiple field barrels with all-refractive collimator and camera optics. For definiteness, the science team is focusing on the MOBIE concept considered by the MST to offer the best combination of simplicity, capability, and affordability given the known cost constraints.

1.1 Acronyms

AGN	Active Galactic Nuclei
ADC	Atmospheric Dispersion Compensator
AO	Adaptive Optics
CFHT	Canada France Hawaii Telescope
CDM	Cold Dark Matter
CMD	Color Magnitude Diagram
DEIMOS	Keck Deep Extragalactic Imager and Multi-Object Spectrometer
DHS	Data Handling System
DM	Deformable Mirror
ECH	Echelle Mode (cross-dispersed, multi-order)
EE	Encircled Energy
ESI	Keck Echelle Spectrometer and Imager
FOV	Field of View
FPRD	Functional and Performance Requirements Document
FSR	Feasibility Study Report
FWHM	Full Width Half Maximum
GC	Globular Cluster
GLAO	Ground-Layer Adaptive Optics
GMOS	Gemini Multi-Object Spectrograph
HST	Hubble Space Telescope
IGM	Intergalactic Medium
IR	Infrared
LGS	Laser Guider Star
LRIS	Keck Low Resolution Imaging Spectrometer
MOBIE	Multi-Object Broadband Imaging Echelle
MST	MOBIE Science Team
NIFS	Near-Infrared Integral-Field Spectrograph
OCDD	Operational Concept Definition Document (this document)
OCS	Observatory Control System
OICS	On-instrument Control System
OIWFS	On-instrument Wavefront Sensor
PN	Planetary Nebula
PSF	Point-Spread Function
QSO	Quasi Stellar Object
RMS	Root Mean Square
SDSS	Sloan Digital Sky Survey
SRD	Scientific Requirements Document
TCS	Telescope Control System
TMT	Thirty Meter Telescope
WFOS	Wide-Field Optical Spectrograph
WMAP	Wilkinson Microwave Anisotropy Probe

1.2 Acknowledgments

The MOBIE team would like to thank all participants of the initial WFOS-HIA feasibility study, which clarified many issues to our benefit.

2 MOBIE Concept: Instrument Description

2.1 Scientific Priorities and Practical Considerations

In considering the overall capabilities of MOBIE, in addition to the WFOS requirements in the TMT Science-based Requirements Document (SRDv17.5), the MST carefully considered issues that drive the cost and technical risk of WFOS-like instruments on large telescopes. These include the following:

- Avoidance of components requiring significant technology development. For example, the very large VPH gratings needed for the previous WFOS-HIA concept have not yet been successfully manufactured, and mosaicing VPH gratings is considered to be a technical risk. Either VPH gratings must be avoided altogether, or the beam size of the spectrograph must be reduced to conform to the largest currently-feasible grating size. Similarly, the spectrograph optics should require no glass or crystal dimensions that are beyond the present capabilities of viable vendors.
- Provide flexible capability with the minimum number of mechanisms. For example, if the field of view requirement for WFOS can be achieved with a single contiguous field, rather than with multiple field barrels that may require independent alignment/flexure control, then this would be desirable. Similarly, if one can avoid remotely selectable dichroics or other optical components, cost savings and avoidance of down-time due to mechanism failures can be realized. The need for camera articulation in the case of VPH-based optical systems is an obvious complexity that is better avoided if the requirements on throughput and spectral resolution can be achieved in a different way. In general, the fewer possible observing modes, the simpler and more robust the instrument.

While the requirements for WFOS were taken very seriously (these are discussed further below), the MST considered some requirements to be more crucial than others. These are, in rough order of priority:

- *Spectral Resolution+Spectral Coverage:* The initial WFOS-HIA concept study clearly identified moderately high resolution ($R \gtrsim 5000$) as important to many, if not most, of the science case studies in the OCDD, and as a result pushed the resolution achieved by the instrument concept to $R \sim 7500$. Such a high resolution was beneficial to both the blue and the red ends of the spectral range. However, many of the projects would simultaneously benefit from much greater wavelength coverage than afforded by the spectrograph optics, designed for a single spectral order for each of two wavelength channels. Because of these considerations, a way of increasing wavelength coverage in the higher resolution modes, without compromising spectral resolution, was a key driver.
- *High Throughput at all wavelengths:* The MST has been acutely aware that cost savings would result if the requirement for throughput versus wavelength were relaxed, so as to lead to a single-wavelength-channel design. The MST believes strongly that this would be a very large compromise scientifically; a single wavelength channel would also compromise wavelength coverage and multiplexing capabilities when both are needed simultaneously.
- *Spectroscopy of single targets:* WFOS will be the only instrument capable of obtaining spectra at optical wavelengths for at least the first several years of TMT operations. We anticipate that it will often be used as the highest sensitivity spectroscopic capability for the purpose of either initial identification or high-quality follow-up of new discoveries, including targets (such as gamma ray bursts) where speed and efficiency of acquisition can make substantial differences in the quality of the data obtained. Thus, the MOBIE concept includes a slit-viewing target acquisition mode and spectroscopic capability that allows for complete wavelength coverage ($0.33\text{--}1.0\ \mu\text{m}$) in a single exposure at every spectral resolution offered, from $R \simeq 1000$ to $R \simeq 7500$.

2.2 MOBIE Concept Overview

MOBIE is an imaging spectrograph designed to perform multi-object spectroscopy, single object spectroscopy, or direct imaging, of very faint sources throughout the optical waveband ($0.31\text{--}1.0\ \mu\text{m}$) using seeing-limited images delivered by TMT. It is designed to have very high throughput ($> 30\%$ at all wavelengths, from slit to detector) in

order to preserve the aperture advantage of TMT relative to current-generation multi-object spectrographs on 8m-class telescopes. MOBIE obtains images or spectra over a contiguous rectangular field of view of 9.6 by 4.2 arcmin (Fig. 1), for a total field area of 40.3 arcmin². The MOBIE structure will occupy a fixed location on one of the TMT Nasmyth platforms, and will be fed directly at the f/15 Ritchey-Chrétien focus by the telescope tertiary mirror, which is articulated to provide access to other permanently mounted instruments on either Nasmyth platform. The entire MOBIE instrument will rotate about a horizontal axis in order to compensate for field rotation and to attain arbitrary position angles of the MOBIE field on the plane of the sky.

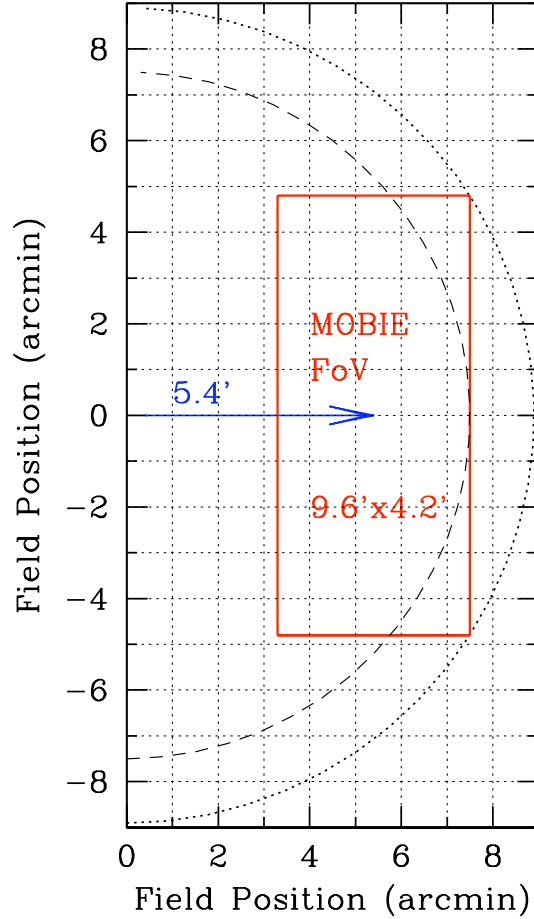


Figure 1: The MOBIE field of view in the f/15 TMT focal plane. Labels correspond to dimensions projected onto the plane of the sky in units of arc minutes, with the origin at the optical axis of the telescope. The center of the MOBIE field is located 5.4 arcmin from the telescope axis. The dashed curve shows the region within which there is no vignetting of the TMT field, at a field radius of 7.5 arcmin; the dotted curve indicates the maximum field angle in the outer corners of the MOBIE field, 8.9 arcmin. The outer corners of the MOBIE field are vignettted by < 5%, due to the telescope optics.

MOBIE will be equipped with two guider/wavefront sensing cameras placed just outside the instrument field of view, as well as a deployable slit-viewing camera to be used for single-object observations or as an additional option for guiding/wavefront sensing. It is envisioned that one of these cameras will be used for guiding, and another for maintaining telescope focus using low-order wavefront sensing signals, and will communicate with the telescope control system and the secondary mirror control system, respectively.

MOBIE will include an atmospheric dispersion corrector (ADC) that adjusts automatically to account for zenith distance of the telescope pointing to ensure that the positions of targets are achromatic over the 0.31-1.0 μ m wavelength range. The instrument will include a closed-loop flexure compensation system that removes any instrument-rotator-

dependent flexure at the required level to maintain image quality and the effectiveness of calibrations.

The MOBIE optical design makes use of a field centered at a position 5.4 arcmin from the telescope optical axis in order to allow for the use of a reflective paraboloidal (achromatic) collimator that functions over the whole design wavelength of the instrument. The 300mm collimated beam is then separated into blue (0.31-0.55 μm) and red (0.55-1.0 μm) channels using a dichroic beam-splitter, forming two separate beams optimized over these wavelength ranges, with separate dispersers, filters, cameras, and detectors. An illustration of one possible MOBIE optical layout is given in Fig. 2.

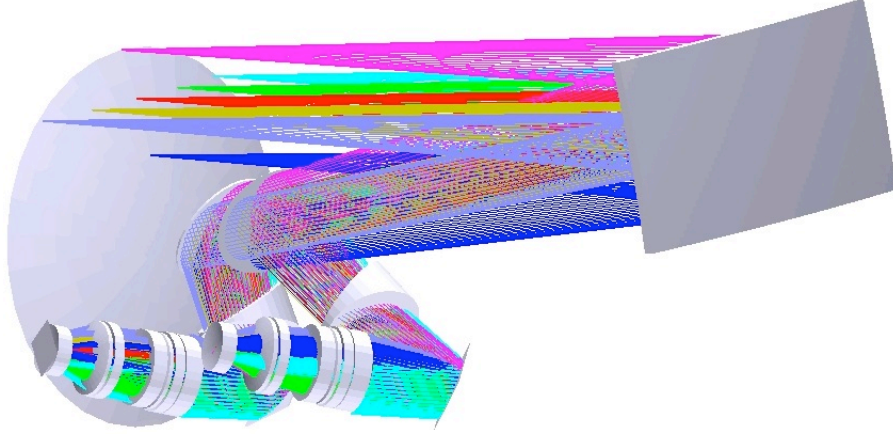


Figure 2: Optical layout example for the MOBIE design with reflective collimator and off-axis field of view. The telescope field of view is indicated with the shaded circle on the left, with the collimator mirror on the right.

MOBIE will provide a highly versatile range of spectral resolution and multiplexing capability through the use of conventional ruled reflection gratings on each wavelength channel of the instrument. In the lowest-dispersion mode ($\mathcal{R} \simeq 1000$) the necessary wavelength coverage is obtained with a single spectral order for each wavelength channel, so that simultaneous spectroscopic observation of $\gtrsim 100$ targets within the MOBIE will be possible with complete wavelength coverage. In higher resolution modes, a different reflection grating, together with a cross-dispersing prism, is used to obtain complete wavelength coverage on each spectral channel in a single exposure of $\simeq 20 - 40$ objects in an “echellette” format (ECH), where the number of targets which can be observed simultaneously depends on the number of spectral orders needed. At a given spectral resolution, smaller wavelength coverage and greater multiplexing is accommodated through the use of order-sorting filters in the beam of each spectral channel, to select one or more orders of interest. If only a single spectral order is needed on each channel (i.e., no cross-dispersion is needed), then slits of arbitrary length up to the full field length of 9.6 arcmin may be used. Thus, the astronomer can select whatever combination of spectral coverage and multiplexing is required by the science, at a given spectral resolution.

MOBIE will incorporate a robust structure to support the various components of the instrument and minimize instrument flexure. In addition, it will incorporate an enclosure to protect its components and provide a light tight environment for the optical elements. The basic design of the support structure and enclosure will also offer ready access to all configurable portions of the instrument, such as the ADC, slit masks, dichroics, filters, gratings, and detectors to facilitate set-up and maintenance.

MOBIE is being designed so as not to preclude additional functionality such as an integral field unit, a tunable filter for narrow-band imaging, and an interface to a possible future Ground-Layer Adaptive Optics system for improving the images delivered to the instrument, and thus allowing for higher-sensitivity observations. These options are discussed further in § 5.

2.3 Summary of Requirements

2.3.1 Modes of operation

MOBIE has three modes of operation: direct imaging, single-object spectroscopy¹ and multi-object spectroscopy. To achieve the maximum observing efficiency and maintain TMT’s aperture advantage over current telescopes, it must be possible to switch between modes with minimal overhead, < 30 seconds for changing the disperser to a mirror (for imaging), or to change reflection grating and (if in ECH mode) cross-dispersing prism.

2.3.2 Instrument Control

MOBIE must provide the means for remote configuration and control of multi-slit masks, single-object slit viewing module, reflection gratings and flat mirrors (for imaging) [both red and blue channels], cross-dispersing prisms [red and blue channels], and filters [red and blue]. The instrument control system must also provide the means for remote configuration of readout modes (e.g., binning, windowing, readout speed) of the detectors [red and blue channels].

The instrument control system for MOBIE must provide information on the status of all remotely configurable components. It must also be capable of supporting remote operations of the instrument, from any site with properly-configured computer systems, with the same features as would be available at the observatory. MOBIE configurations should have the capability of being “scripted”, so that users may save configurations that may then be executed during daytime or night-time use of the instrument.

2.3.3 Mask System

The MOBIE slitmask system must be capable of accommodating at least 10 masks, which would typically be loaded into the mask exchange system by observatory staff during the daytime prior to a night of observing. It should not be necessary to interact manually with the mask system during night-time observing.

Software tools must be available to astronomers for the design of slitmasks given a list of potential targets with accurate celestial coordinates; the resulting mask design files would be submitted to the observatory at least ~ 2 weeks before the start of an observing run, to provide flexibility to the observatory staff in planning the work necessary to manufacture them.

Mask fabrication should be done at a facility that is located as near to the observatory as possible, and it should be possible to manufacture masks on short notice (a few hours) for cases where a very fast turnaround is justified scientifically.

A database of mask design files should be maintained by the observatory, which will include the celestial coordinates of each target on the mask. The same information should be encoded on the mask, read by the MOBIE mask server, and ingested into the FITS header of any mask used for any calibration or science observation with MOBIE, in the interest of supplying meta-data necessary for useful archiving.

2.3.4 Multi-slit mask Target Acquisition

Very efficient field acquisition is required in multi-object spectroscopy mode; it should be possible to go from initial telescope pointing, through coarse and fine mask alignment, to the start of a science integration in < 3 minutes. This efficiency is achieved by making guide star selection part of the mask design process, and by tying the MOBIE science and guide fields to the same local coordinate system. More details on the suggested acquisition process are given in § 4 below (see also § 3.5).

2.3.5 Slit-viewing and Single-object Target Acquisition

Acquisition of single spectroscopic targets should be even more efficient, with a requirement of < 1 minute from telescope pointing to the start of a scientific integration. A slit-viewing capability with a field of view of $\simeq 1$ arcmin or greater should make this easily achievable. The current MOBIE concept is to use a deployable slit-viewing camera

¹One might think of this mode as “long-slit spectroscopy”, but because the user may choose the ECH mode for single-target observations (where the slit may be as short as 2”), we will continue to use “single-object” to distinguish it.

module that is moved to a position near the center of the MOBIE field and which includes selectable slits and deckers for single-target observations using any of the MOBIE spectroscopic modes.

2.3.6 Additional Modes

Additional modes of operation provided by the addition of sub-systems such as an IFU, a tunable filter (or other narrow-band imaging capability), or facilitating GLAO should not be precluded by the MOBIE design. Some example science cases and suggested means of implementation of a tunable filter system are given in § 5 below.

2.3.7 Wavelength Range

The MOBIE optics will meet the image quality and throughput requirements over the 0.31-1.0 μm wavelength range (ORD requirement is 0.33-1.0 μm). While the baseline/early-light coatings on the telescope optics may not perform well shortward of 0.33-0.34 μm , the MOBIE optics will work well to the atmospheric UV cut-off near 0.31 μm . The reflective collimator can be coated with a multi-layer coating that achieves $> 95\%$ reflectivity over the design wavelength range of MOBIE. This performance is achieved, e.g., by the coating on the 0.5m LRIS collimator mirror at the Keck Observatory. The MOBIE camera optics are being optimized for a dichroic split near 0.55 μm , but both cameras will perform well over larger wavelength ranges (i.e., larger than 0.31-0.55 μm for the blue camera and 0.55-1.0 μm for the red camera), should additional dichroics be implemented in the future (or if single channel wavelength operation becomes necessary or desired at any point).

2.3.8 Dichroic Beam-Splitter

Because MOBIE allows for complete wavelength coverage of the entire optical waveband for any of its spectral resolution options, the dichroic beam-splitter need not be remotely selectable. However, it is required that the dichroic be accessible enough to allow for occasional manual removal/replacement.

2.3.9 Filter System

Remotely deployable filters are required on both the red and blue sides of MOBIE; an initial filter complement would include interference filters to isolate the free spectral range (FSR) of each order in ECH mode for applications not requiring complete wavelength coverage (or for which the use of longer slits is desirable), and filters which isolate approximately half of the total wavelength range of either spectral channel (i.e., 2 filters per spectral channel, each including \simeq half the number of spectral orders) to allow greater multiplexing. The exact filter specifications will depend on the grating combinations selected for initial construction; some example configurations are given in Table 1. In the case of the $\mathcal{R} \simeq 5000$ ECH mode, a total of 6 or 7 filters would be required for each spectral channel. The filter system need not hold all of the filters simultaneously, but at least 6 must be available for use on a given night on each wavelength channel. It should be possible for filters to be easily changed during the daytime, to load the filters needed for the coming night.

At present, it is assumed that the suite of filters provided for spectroscopy would be adequate for direct imaging as well. Of course, in direct imaging mode, images of the same 9.6 by 4.2 arcmin field could be obtained in 2 bands simultaneously— one on the blue side, and one on the red.

2.3.10 Field of view

The field of view requirement for WFOS is $\geq 40 \text{ arcmin}^2$. The current (reflective collimator) MOBIE concept delivers a field of view of 40.3 arcmin^2 , arranged in a rectangular configuration as shown in Fig. 1. The slit length requirement for WFOS is $> 500 \text{ arcsec}$; MOBIE provides a total slit length of 576 arcsec. While WFOS is not required to achieve these goals in a single contiguous field, it is advantageous from both a practical and scientific standpoint to do so if the optical design allows for it. Placing the MOBIE field off-axis allows for the use of a reflective collimator, which translates into cost savings, and benefits overall instrumental throughput because it eliminates a large number of air/glass surfaces. A similar reflecting collimator arrangement has been used successfully in current-generation imaging spectrometers, such as LRIS and DEIMOS on the Keck telescopes.

Table 1: Example Spectral Resolution Options*

\mathcal{R}	Order	FSR	Length	\mathcal{R}	Order	FSR	Length
Blue				Red			
985	2	0.308-0.554	136	1077	1	0.550-1.000	131
2600	6	0.308-0.365	92	2480	6	0.536-0.635	88
	5	0.365-0.447	112		5	0.635-0.779	107
	4	0.447-0.580	145		4	0.779-1.010	138
5040	11	0.311-0.341	95	4860	11	0.558-0.611	91
	10	0.341-0.377	105		10	0.611-0.676	101
	9	0.377-0.421	117		9	0.676-0.756	113
	8	0.421-0.478	133		8	0.756-0.857	128
	7	0.478-0.552	154		7	0.857-0.991	148
7900	18	0.313-0.330	89	7780	18	0.565-0.597	89
	17	0.330-0.351	94		17	0.597-0.633	94
	16	0.351-0.373	100		16	0.633-0.674	100
	15	0.373-0.399	107		15	0.674-0.721	107
	14	0.399-0.429	115		14	0.721-0.774	115
	13	0.429-0.463	124		13	0.774-0.836	125
	12	0.463-0.503	136		12	0.836-0.909	136
	11	0.503-0.552	149		11	0.909-0.996	149

* – All resolution values are for a 0.75 arcsec entrance slit; order lengths in mm, at the detector. Each configuration is designed for use with a dichroic beam-splitter at 0.55 μm . The camera field of view corresponds to $\simeq 220$ mm.

2.3.11 Spectral Resolution

The science cases for TMT outlined in both the “Detailed Science Case” (DSC) and both the WFOS-HIA and the current OCDDs OCDDs have spectral resolution requirements in the range $\mathcal{R} = 1000 - 7500$. MOBIE is being designed with at least three spectral resolution options, $\mathcal{R} \simeq 1000$, $\mathcal{R} \simeq 5000$, and $\mathcal{R} \simeq 8000$ (all for a 0.75 arcsec slit). Additional resolution options can be achieved by adding new grating/prism combinations. Four examples, ranging from $\mathcal{R} \simeq 1000 - 8000$, are given in Table 1; the lowest-dispersion mode uses one spectral order per wavelength channel, while the highest resolution example uses 8 spectral orders.

2.3.12 Wavelength coverage

The science drivers for WFOS call for wavelength coverage over the entire range 0.31 – 1.0 μm , where the low-resolution mode is required to cover the whole range simultaneously (i.e., in a single exposure for a given object). The highest efficiency and scientific flexibility is achieved by dividing the wavelength range in two near the center of the full waveband using a dichroic beam-splitter, so that optical materials and coatings, spectral dispersers, filters, and detectors can be optimized over a single octave in wavelength instead of two.

A goal for the SRD WFOS instrument is to cover as much of the full optical waveband as possible, even at moderate dispersion. The MOBIE design allows for full simultaneous wavelength coverage in both low-dispersion (single-order) and moderate dispersion ECH modes. By using short slits ($\simeq 2 - 6$ arcsec) and carefully optimized prism cross-dispersers, MOBIE can capture the entire wavelength range in a given spectral channel at (e.g.) $\mathcal{R} \simeq 5000$ using as little as $\simeq 15''$ of slit-length. Thus, even in ECH mode with full wavelength coverage, a multiplex factor of up to 40 could be achieved².

One of the distinct benefits of the ECH mode is that every wavelength within the range desired is close to the effective reflection grating blaze peak, resulting in high throughput and relatively uniform sensitivity at all wavelengths. This is particularly important for science which benefits from large bandwidth, such as the identification or characterization of transient phenomena (§ 3.8) or IGM tomography (§ 3.5).

²Possibly more typical cases would have $\simeq 20$; see § 3.5

2.3.13 Image quality

The SRD requirement for WFOS in imaging mode is $\leq 0''.2$ FWHM over any $0.1\mu\text{m}$ interval; in spectrograph mode, the image quality requirement is $\leq 0''.2$ FWHM at every wavelength. These requirements are intended to preserve the image quality delivered to the telescope focal plane at the focal plane of WFOS. There is clearly a trade between surpassing the image quality requirement with additional corrective optics, and overall cost, complexity, and end-to-end throughput. We believe that the current MOBIE optical design concept achieves a good balance between simplicity and performance.

2.3.14 Atmospheric Dispersion Corrector

Because MOBIE is designed to operate over a large wavelength range simultaneously using focal plane slitmasks, an atmospheric dispersion corrector (ADC) is essential. It is scientifically important that the images of spectroscopic targets relative to spectroscopic slits be as wavelength-independent as possible. The WFOS SRD requirement for the ADC is that it must maintain centroid positions to $< 0.05''$ rms for any zenith distance of 60 degrees or less, over the wavelength range $0.31 - 1.0\mu\text{m}$.

2.3.15 PSF uniformity and stability

The PSF uniformity over the field is affected by both telescope (optics, guiding errors) and instrumental aberrations. If the variations in PSF shape or FWHM are significant compared to the image size (in spectroscopic mode), errors in wavelength calibration (and decreased slit throughput) result. Such systematic errors can be exacerbated when the seeing is especially good. It is required that the PSF in the instrument focal plane should be uniform over the full field at the level of $\lesssim 5\%$ in FWHM for median seeing conditions (assume $0.63''$ FWHM at 500nm) over the $0.31 - 1.0\mu\text{m}$ range.

2.3.16 Field distortion

Field distortion at the camera image must be small enough so as not to contribute to instrument inefficiency. To satisfy this requirement, the distortion must be characterizable so that the mapping of the telescope focal plane (including the guiders/WFSs) to instrument focal plane is consistent at the 0.1% level in direct imaging mode. This guarantees the “predictability” of image positions at the science detector to an accuracy of $\simeq 0.5$ arcsec, making field acquisition and data reduction significantly more efficient. It is assumed that the portion of the TMT telescope focal surface used by MOBIE is similarly predictable and consistent.

2.3.17 Throughput

For MOBIE to capitalize on the aperture advantage of TMT compared to existing facilities, it must achieve a minimum throughput (not including slit or telescope losses, the fraction of photons incident on the TMT primary detected at science focal plane) of 30% over the $0.31-1.0\mu\text{m}$ wavelength range. The current MOBIE optical design concept is estimated to exceed the throughput requirement for $\lambda \geq 0.34\mu\text{m}$.

2.3.18 Observing efficiency

As a general-purpose instrument, MOBIE will be used for many different science programs over its lifetime, many of which will be surveys of one sort or another. Observing efficiency is therefore crucial. It is expected that MOBIE may be required to switch between observing modes and perform field acquisitions many times on a typical night. It must be possible to use calibrations obtained during the afternoon, or using the twilight sky, so that the entire useful night time may be used for science integrations for most applications. This implies that reconfigurations must be possible without altering the subsequent calibrations of a given mode, which has implications for the repeatability of mask, slit, and disperser insertion, instrument flexure, and internal spectrograph alignment. To minimize the impact on efficiency, all mechanisms must be operable simultaneously during reconfigurations, and no single mechanism movement shall require more than 30 seconds.

2.3.19 Guiding and Wavefront Sensing

The available field of view for guide star selection must be such that the probability of finding a guide star in one or more of the guide regions is $> 95\%$ at the Galactic poles assuming guide star limiting magnitude of $V = 23$, appropriate for accurate centroiding ($0.05''$ rms) in < 10 s integrations with bright moon conditions. The cumulative surface density of stars with $V \leq 23$ at the Galactic poles is $\simeq 1.1 \text{ arcmin}^{-2}$, so that the probability of finding no guide star is 5% when the guide field area is $\sim 1.2 \text{ arcmin}^2$ (assuming Poisson statistics). Thus, the guide/WFS area must have a total area that exceeds this number. A similar field size would be appropriate for the slit-viewing area for the acquisition of single targets.

2.3.20 Instrument Rotator Performance

The field de-rotation must be accurate enough so as not to significantly degrade alignment or image quality at all zenith distances > 0.5 degrees. The rotator system must be calibrated to provide field position angles accurate to 0.1 degrees (absolute, open loop), and it must be possible to make fine adjustments to the PA accurate to 0.01 degrees (which would change the extreme positions on full-field MOBIE mask by $\simeq 0.1''$) during fine alignment of slit masks.

2.3.21 Instrument Flexure

Instrument flexure must be controlled at the level of $< 0.1''$ at the detector. This ensures that calibrations may be obtained during the daytime in most cases, that an accurate mapping between telescope focal surface and detector position can be maintained, and that spectral resolution and calibration are not degraded. Meeting this requirement probably implies a closed-loop flexure correction system.

2.3.22 Sensitivity

The SRD requirement for WFOS is that sensitivity must be limited by Poisson counting statistics for any integration time longer than 300 seconds. This requirement flows down to the ability to flat-field accurately in the high S/N regime, and to perform extremely accurate background subtraction for very faint objects, well below the level of the night sky background.

The MOBIE concept, relying as it does on the use of short slits for multi-order wavelength coverage in ECH mode, may require special observing techniques to achieve this requirement. In general, the most accurate background subtraction is achieved when fast beam-switching techniques are used, in which “object” and “sky” are observed essentially simultaneously on the same regions of a detector³. Such techniques should be possible with slits as short as $\simeq 3''$, where nods would move objects from one side of the slit to the other on a short timescale. Alternatives to short slits would be beam-switching between pairs of short slits (reducing the multiplex factor by $\simeq 2$) for each target, and observing at lower resolution and/or with single-order ECH mode. Simple telescope nodding using short individual exposures would work if the duty cycle of nod and read-out could be kept below $\simeq 10\%$ of the exposure time and read noise is negligible (see § 4.1).

2.3.23 Stray Light Control

Because TMT will not be baffled, elimination of stray light must be accomplished within the instrument. MOBIE will require field-stop baffling at the telescope focal surface, and control of the pupil within the spectrograph to reduce the effects of scattered/stray light. These controls must reduce stray light to $< 3\%$ of the dispersed night-sky continuum brightness averaged over the field of view, to ensure that it does not compromise background subtraction for very faint targets.

2.3.24 Detector Characteristics and Special Observing Modes

Aside from low read noise and dark current, and high QE over the whole design range (optimized for red or blue), the sensitivity issues discussed above would benefit significantly from red detectors with zero or negligible fringing

³Nod-and-shuffle techniques are one implementation of such a scheme, where small telescope moves (nods) are coordinated with the clocking of charge on CCD detectors (shuffles).

(to preserve accurate flat fielding and sky subtraction even after small amounts of instrumental flexure), and generally from very fast readout speed for both blue and red CCD mosaics. It is quite likely that CCDs will generally be binned 2x2 or even 4x4 given the final plate scale (ignoring anamorphic magnification) of $\simeq 0.054''/\text{pixel}$ at the MOBIE detectors. In any case, several binning options will be essential, without compromising the detector useful dynamic range.

If nod and shuffle capability is desired, it may require (e.g.) the long axis of 2kx4k detectors to lie along the spatial, rather than spectral, direction; nod/shuffle may also impose additional requirements on the charge transfer efficiency and low-level charge traps in the detectors. Any type of beam switching (with cadence in the range 20-30s) will require very efficient communication between the telescope control system and the instrument.

2.3.25 Requirements Related to Direct Imaging

Direct imaging through broad-band filters will be extremely inefficient unless the readout speed of the detector mosaics is made significantly shorter than the typical exposure during which the background would exceed 50% full well. For example, the I-band detection rate of photons from the sky with TMT/MOBIE is expected to be $> 500,000 \text{ e- s}^{-1} \text{ arcsec}^{-2}$, or $> 1500 \text{ e- s}^{-1} \text{ pix}^{-1}$ for no CCD binning, assuming $15\mu\text{m}$ pixels. Typical CCDs would accumulate $> 50\%$ full-well in less than 1 minute.

Similarly, some calibration exposures (e.g., spectrophotometric standards) may require very short exposures using a 30m aperture, so camera shutters that remain accurate and allow for exposures $\ll 1$ second may be beneficial.

2.3.26 Facility Requirements

As discussed in § 4.3, useful spectroscopic flat fields with MOBIE must include the telescope optics (illumination produced internal to the instrument will not be adequate for such a wide field instrument). Much more effective flat fields are obtained using white light illumination of the inside of the telescope enclosure, to allow flat-field calibrations to be obtained during the daytime and including all of the telescope optics. Even if many users elect to obtain spectroscopic flat fields using the twilight sky, dome flats must be available as a backup. The illumination source must produce light across the full MOBIE wavelength range simultaneously, and ideally would provide the means to adjust the color temperature of the illumination. The region used on the enclosure should be slightly larger than the primary mirror in diameter, and should be illuminated as uniformly as possible.

3 Sample Observing Scenarios

In this section we analyze the following set of representative observing scenarios:

- (1) Age dating of the first structures that formed within the Milky Way from intermediate-resolution ($\mathcal{R} \approx 2000$), UV/optical (0.34–0.5 μm) spectroscopy of white dwarfs in globular clusters.
- (2) Studying the chemistry and kinematics of metal poor stars in the extreme halo of the Milky Way as a means of understanding the early evolution of the Galaxy, using $\mathcal{R} \simeq 8000$, broad-band spectroscopy. .
- (3) Reconstruction of the history of star formation, chemical enrichment and hierarchical merging in Local Group galaxies from intermediate- and high-resolution ($\mathcal{R} \approx 3000, 5000$) optical/near-IR (0.43–0.53 μm , 0.8–0.9 μm) spectroscopy of their halo field stars.
- (4) Mapping of the structure of dark matter halos in elliptical galaxies from high- and intermediate-resolution ($\mathcal{R} \approx 2000, 5000$) near-UV/optical/near-IR (0.36–0.54 μm , 0.6–0.9 μm) spectroscopy for thousands of star clusters and planetary nebulae.
- (5) Tomographic reconstruction of intergalactic medium and an exploration of galaxy-IGM connection at redshifts of $2.0 \lesssim z \lesssim 3.5$ from low- and high-resolution multiplexed ECH spectra ($\mathcal{R} \approx 1000, 5000$) near-UV/optical spectroscopy of background Lyman break galaxies across the entire wavelength interval covered by MOBIE.
- (6) Using high quality $\mathcal{R} \simeq 5000$ MOBIE/ECH spectra of galaxies at $z \sim 2 - 5$ to understand the stellar populations, gas-phase kinematics, and chemistry of forming galaxies during the peak epoch of galaxy formation.
- (7) Observing close QSO pairs to study the environments of the sites of massive galaxy and supermassive black hole formation, with multiplexed $\mathcal{R} \simeq 8000$ MOBIE/ECH spectra of faint QSOs at $z > 2$.
- (8) Rapid-response high resolution MOBIE/ECH and/or $\mathcal{R} \simeq 1000$ wide-bandwidth spectra of transients identified with the next generation of wide-area surveys on the ground and in space.

As described in Section 1, these science cases have been chosen partially on the basis of perceived scientific importance, and partially on the basis that they collectively push the requirements of the instrument. Most of these sciences cases have been explored, and optimal observing scenarios devised, with the aid of relatively details simulations of TMT/MOBIE performance. Each subsection is structured along the lines of an observing proposal, with a science justification followed by a technical description. For the sake of descriptive efficiency, calibration steps common to many observing scenarios are described separately in §4.

3.1 Stellar Evolution and White Dwarfs

3.1.1 Background

Photometric and spectroscopic studies of Galactic star clusters have served as the observational foundation for our understanding of stellar evolution, structure, and star formation. The co-spatial and coeval characteristics of these resolved stellar populations make them ideal astrophysical laboratories for such studies. Open clusters are valuable as they span wide ranges of age, metallicity, and location from the Galactic center; their older and more massive counterparts, the globular clusters, are equally important as they provide fundamental estimates for the age of our Galaxy, and with a mild extrapolation, the universe. These ages have typically been measured by comparing theoretical models to the morphology of the main sequence and turnoff in cluster color-magnitude diagrams (CMDs). However, such comparisons are difficult given the many degeneracies and uncertainties in the theoretical isochrones (e.g., the age-metallicity degeneracy). D’Antona (2001) examines this and various other uncertainties in the models (e.g., color-transformations, diffusion processes, sedimentation of heavy elements, convective efficiency, and overshooting) as well as distance uncertainties and concludes that the absolute age of any Galactic globular cluster is only known to within ± 3 Gyrs accuracy (see also Krauss and Chaboyer 2003).

Having been amongst the first objects to form in our Galaxy, all stars in Galactic globular clusters with masses $\gtrsim 0.8 M_{\odot}$ have by now extinguished their nuclear fuel and are therefore no longer on the cluster main sequence. Devoid of any remaining energy sources, the cores of these stars have cooled over billions of years producing a large population of white dwarfs within these clusters. Recently, very deep observations with the Hubble Space Telescope (HST) have unveiled hundreds of these stellar cinders in several of the nearest globular star clusters, such as NGC 6397 (Richer et al. 2005), M4 (Hansen et al. 2004; see also Figure 3), and ω Centauri (Monelli et al. 2005). Although preliminary age estimates can be derived from modeling the luminosity function of white dwarfs in these systems (Hansen et al. 2002; 2004), the key missing ingredient to calibrate the age measurement is a determination of the masses of the white dwarfs along the cooling sequence. In fact, no direct measurement of the mass of a Population II white dwarf has ever been made (i.e., through the fitting of spectral models to observed hydrogen Balmer line profiles).

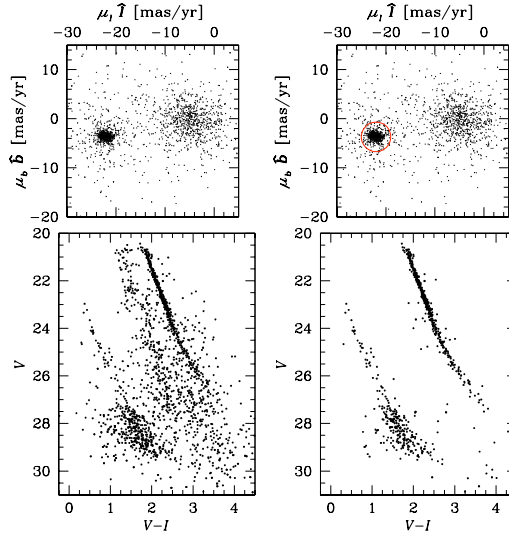


Figure 3: *Left* - The proper motion (top) and color-magnitude diagram (bottom) are shown for all stars detected in a 123 orbit *HST* exposure of the globular cluster M4. The proper motions have been measured by observing the cluster at two different epochs, separated by 6 years. The photometry shows a very tightly constrained M4 main-sequence down to very low main-sequence masses ($0.09 M_{\odot}$) as well as a rich white dwarf cooling sequence. Galactic disk and bulge stars along the line of sight are also seen. *Right* - Isolating just the cluster stars in the proper-motion diagram (top), gives a very clean color-magnitude diagram (bottom) showing a rich white dwarf cooling sequence.

Equally important to measuring the masses of white dwarfs in globular clusters are mass determination of white dwarfs in open clusters. Open clusters range in age from a few tens of Myrs to 10 Gyrs. Therefore, young clusters still contain very massive main-sequence stars whereas old clusters are nearly as evolved as the globular clusters. Consequently, the white dwarf populations in open clusters vary drastically from one system to another.

An aggressive program to study white dwarfs in a sample of nearby open clusters over a range of ages is now underway at the Keck Telescope (Williams, Bolte & Koester 2008 and references therein). Detailed Balmer line profile fitting is used to measure the masses of the cluster white dwarfs from which one can deduce the relationship between the initial to final stellar mass which defines the the amount of mass lost by low to intermediate mass stars during main sequence and advanced stages of evolution. This is a required input for constraining chemical evolution in galaxies, determining supernova rates (van den Bergh & Tammann 1991), understanding feedback processes and star formation in galaxies (e.g., Somerville & Primack 1999), and determining distances and ages of globular clusters from modeling their white dwarf cooling sequences (Hansen et al. 2004). Such studies also reveal the upper limit to the mass of a star that evolves into a white dwarf, equivalent to determining a lower limit to the mass of a star that can ignite carbon burning in its core. They calibrate and test our understanding of the details of stellar evolution.

3.1.2 Specific science goals

The combination of 1) a 30-meter telescope, 2) a wide-field multi-object optical spectrograph, and 3) CCDs with the high sensitivity in the blue present us with the first opportunity to measure the temperatures, gravities, cooling ages, and masses of faint white dwarfs in globular clusters. These observations will accomplish several scientific goals:

1. Calibrate the white dwarf cooling sequences in globular clusters and provide us with an entirely independent method for determining the ages of the first structures to form in our Galaxy. The method offers several advantages over canonical techniques for determining these ages. For example, the age-metallicity relation is removed in white dwarfs (all metals have sunk due to the high gravities) and therefore the age spread among the Galactic globular cluster system can be investigated in an unbiased way.
2. The combination of having an accurate initial-to-final mass relationship and the age of a globular cluster provides us with an excellent probe of the now evolved upper main sequence of a Population II system. The masses of white dwarfs in globular clusters can be used to determine the progenitor initial mass function of the system (given a good initial-to-final mass relationship).
3. The spectral classification of these WDs will yield important insights into the physics that determines whether white dwarfs are DA (H-rich) or DB (He-rich). Recently, Rubin et al (2008) have found that almost all massive WDs in open star clusters are DA type.

3.1.3 Observations and Targets

Direct mass measurements of white dwarfs require moderate/high signal-to-noise spectra in the blue. Specifically, the shapes of the highest order hydrogen Balmer lines (H7 at 3970Å [He], H8 at 3889Å, H9 at 3835Å, etc.⁴) are very sensitive to changes in the temperature and gravity of the star (Bergeron, Saffer, & Liebert 1992). Therefore, this program is ideally suited for a large-aperture telescope with blue-sensitive CCDs.

White Dwarfs in Globular Clusters

The nearby Galactic globular star clusters M4 and NGC 6397 are ideal targets for this study. These clusters are nearby (~ 2200 pc) and large (angular diameters of ~ 30 arcmin) and have both been imaged many times, including multiple ultra-deep *HST* observations, and very rich white dwarf populations have already been photometrically identified within them. Figure 3 (bottom-right) shows that within a single *HST* WFPC2 field (≈ 5.5 arcmin²), M4 contains ~ 30 white dwarfs with $V < 26$. With the increased field of view of MOBIE ($4.2' \times 9.6'$), we will observe at least 150 white dwarfs to this limit in this cluster, per pointing. A similar number of white dwarfs are also seen in a preliminary CMD for NGC 6397, for which ultra-deep *HST* observations are also available. These clusters have been specifically targeted by *HST* due to their different environments. For example, NGC 6397 is much more metal-poor than M4 ($[\text{Fe}/\text{H}] = -2.0$ vs -1.3) and has a collapsed core⁵. TMT+MOBIE will allow us to directly test if NGC 6397 is older than M4 by comparing both the masses of white dwarfs on the cooling sequence (progenitor ages and masses would vary) and by comparing the observed white dwarf luminosity functions in a relative sense. Current generation telescope/instrument combinations (e.g., Keck/LRIS) are unable to reach these scientific goals as reliable mass measurements are limited to white dwarfs with $V < 24$. At this bright limit, very few white dwarfs are present on the observed globular cluster cooling sequences (and they would have no appreciable mass difference).

⁴See <http://chinadoll.as.arizona.edu/~schmidt/spol/features.html> for a convenient list which focuses on lines with obvious relevance to astronomy. See http://physics.nist.gov/cgi-bin/AtData/main_asd for a more comprehensive list.

⁵For readers without a background in astronomy: the bracket notation in this section is a convenient shorthand commonly used to compare the abundance ratios of chemical elements to the corresponding ratios in the sun. $[A/B]$ is defined as the base-10 logarithmic ratio of the chemical abundance of A to B relative to ratio in the sun, i.e. $[\text{Fe}/\text{H}] = \log_{10}(\text{Fe}/\text{H}) - \log_{10}(\text{Fe}/\text{H})_{\odot}$. For example, $[\text{Fe}/\text{H}] = -2.0$ means that the ratio of iron to hydrogen is 1% of that in the sun.

3.1.4 Pre-imaging

We will require pre-imaging for all of our targets at least 3–4 weeks before the spectroscopy is scheduled. For the two globular clusters, pre-imaging is necessary to increase target selection over a larger area than that for which HST imaging already exists from earlier projects as well as from the ongoing ACS Survey of Globular Clusters, a uniform survey with HST of the central fields of 65 targeted clusters.

The largest contamination in the faint-blue end of the CMD comes from faint galaxies. Adaptive optics is desirable as it would greatly help discriminate white dwarfs from galaxies using morphology criteria. We will eliminate unresolved galaxies by measuring their colors and plotting these on a two-color diagram, $U - B$ vs. $B - V$ or $g - r$ vs. $r - i$. Photometry in such broad band filters is also advantageous as it allows us to fit white dwarf cooling models to the observed white dwarf cooling sequence on the cluster CMDs.

Since only the highest S/N spectra will be fit to models, it is not necessary to obtain ultra-deep imaging. We set our limit at $V = 27$, one magnitude below the faintest targets for which we will obtain a spectrum. Therefore, the imaging aspect of this program represents a small cost to the overall project.

3.1.5 Technical Remarks and Mask Design

Multi-object spectroscopic masks will be constructed in each field using the astrometry from the pre-imaging. The relevant spectral region in order to determine white dwarf parameters from hydrogen Balmer line spectroscopy is 3700–5000Å (H10 to H β). However, extending this spectral coverage to even bluer wavelengths (i.e., down to the atmospheric cutoff) is desirable in order to determine temperatures of the hotter white dwarfs independently from continuum fitting. This will be especially valuable in other white dwarf related studies with TMT/MOBIE. A low resolution ($\mathcal{R} \sim 2000$) configuration with the above spectral coverage will be necessary for this project. We also recommend the use of an atmospheric dispersion corrector to minimize slit light losses. We will set exposure times depending on several factors although we anticipate spending at least half a night on each cluster to maximize the S/N. Masks will be prepared for multiple slit widths to accommodate seeing variations. Although not essential for this project, overall overhead will be greatly reduced if the mask making process could accept astrometry from other telescopes.

In Figure 4 (top) we simulate spectra (P. Bergeron et al. 2004, private communication) of white dwarfs with various S/N assuming roughly the configuration above. Only a portion of the spectra are shown for clarity (H8 to H β). In the bottom panel, we present results from fitting white dwarf models to 500 simulated spectra with S/N = 20 (shown as the fourth spectrum in the top panel). At this S/N, we find that we will be able to accurately determine the mass of a white dwarf to within $0.05 M_{\odot}$. We expect this to be the quality of the worst spectrum that we obtain in this project.

In Figure 5 we present real spectra of white dwarfs obtained with Keck/LRIS in the Galactic open cluster NGC 2099 (see Kalirai et al. 2001b). In just 2 hours, we are able to obtain S/N = 15–20 spectra of $V = 23.7$ magnitude stars. Considering the larger aperture and increase in exposure time (0.5–1 night per target), this suggests that we can conservatively set $V = 26$ as our magnitude limit for the spectroscopic program. This limit is faint enough that we will be able to measure masses of white dwarfs at the end of the cooling sequence in all of our open clusters, except NGC 6791 (see Bedin et al. 2005). For this old open cluster, and for the globular clusters, we will constrain masses several magnitudes below the tip of the white dwarf cooling sequence. Those masses will then be used to calibrate the lower cooling sequence given the cluster mass function.

3.1.6 Path to Science

We anticipate that no other data will be required to complete the goals of this project. White dwarf cooling models can be directly used to age date the globular clusters by comparing the distribution of white dwarfs along the cooling sequence via a luminosity or color function (or both), once the masses of the stars are known. By doing this in two clusters such as M4 and NGC 6397, a relative comparison of the ages yields powerful constraints on the formation timescales of the Galactic globular cluster population. It provides an independent measure from the extensive CMD analysis of the ACS Survey of Globular Clusters, a key project with HST, where metallicity effects and uncertainties may blur our ability to measure reliable relative ages.

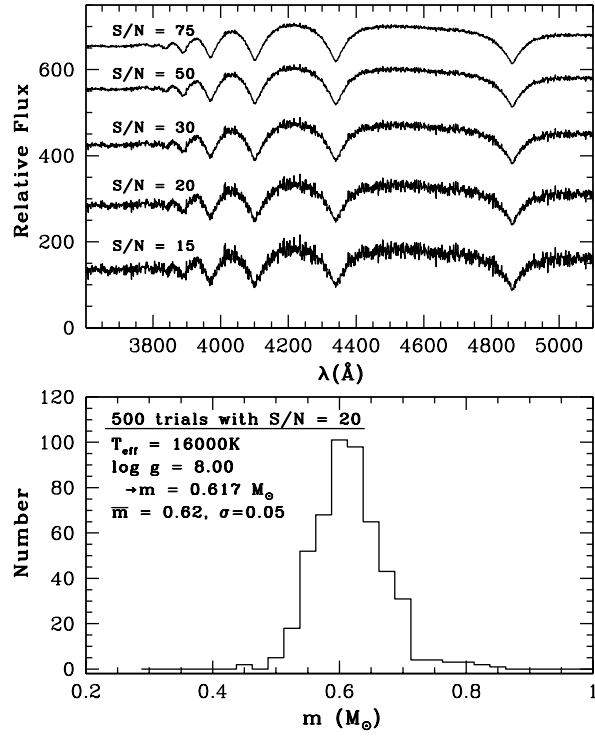


Figure 4: *Top* - Simulated spectra of various S/N are shown. *Bottom* A 500 trial simulation of a WD with S/N = 20. The mean output mass is found to be $M = 0.62 \mathcal{M}_{\odot}$ with a dispersion of $0.05 \mathcal{M}_{\odot}$ for an input mass of $0.617 \mathcal{M}_{\odot}$. This will be the quality of the worst spectra that we obtain in this project. The uncertainty in the mass for brighter stars will be much less.

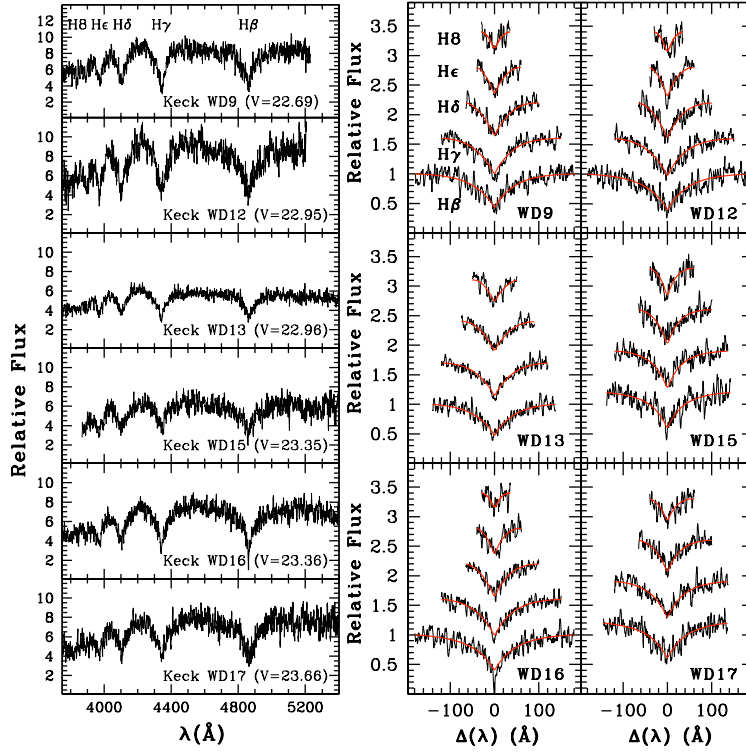


Figure 5: *Left* - Examples of six faint white dwarf spectra are shown ranging from $V \sim 22.7$ to $V \sim 23.7$ (all from Keck/LRIS NGC 2099 data - 2 hours of exp. time). *Right* - The spectral fits of these stars to Balmer line absorption models (Bergeron, Wesemael, & Beauchamp, 1995) is shown. For WD9, we indicate H β , H γ , H δ , H ϵ , and H8. See Kalirai et al. (2005a) for more information.

3.2 Metal Poor Stars: Galaxy Formation from the Stellar Halo of the Milky Way

The chemical abundances of metal poor stars in the halo are imprinted with residual evidence of the hierarchical galaxy formation process, providing a rare opportunity to test Λ CDM and galaxy formation simulations on small scales. We now have robust observational evidence that some fraction of the Galactic stellar halo was acquired through multiple accretion events. In addition to the identification of specific recent or ongoing mergers like the Sagittarius dSph (e.g., Majewski et al. 2003), Bell et al. (2008) use SDSS photometry over 8000 square degrees to quantify the statistical variation of stellar density and find significant deviations from a smooth halo. Their results are in agreement with the fraction and radial distribution of distant substructure from the simulations of Bullock & Johnston (2005). However, maps of spatial overdensity are only sensitive to the recently accreted substructure, whereas most merger activity is expected to have been early in the Galaxy's history. The addition of line of sight velocity information can extend the search for substructure to events further in the past (e.g., Chiba & Beers 2000, Carollo et al. 2007), and with full six dimensional phase space information it may be possible to identify the members of individual accretion events (Helmi et al. 2006).

3.2.1 Key Observable: Chemical Abundance Patterns in Distant Metal Poor Stars

By finding substructure in the halo we can identify stars that formed in systems that later merged with the Milky Way. If we can recover information about the mass and star formation histories of the progenitor systems, we can learn about galaxy formation. The link between stars in present day halo substructure and their original environments is stellar chemical abundance information.

Nearby halo stars seem to show little evidence of substructure in phase space and are rather homogeneous in abundance space. The outer halo ($r > 20$ kpc) shows the most significant and promising signs of recent accretion events. That distance is also where simulations suggest that the fraction of recently accreted stars should increase (Bullock & Johnston 2005). Stars from recent accretion events are likely to have formed in environments with different star formation, and therefore chemical evolution histories, from stars in the nearby halo region. For example, as shown in Figure 6, if the outer halo was built by accreting dSph galaxies like the ones we see today, abundance ratios in the α -elements may be noticeably different in substructure in the outer halo as compared with local samples.

To assemble the large sample of outer halo stars required for statistical analysis of the accreted population requires significant investment in observing time on 10m class telescopes, and can only reach to $\sim 50\%$ of the extent of the stellar halo.

Using targets obtained from the SEGUE survey, a program has recently begun at UCSC to measure chemical abundances in the 'nearby' outer halo (distances between 20 to 50 kpc) using the ESI instrument on Keck. While it is prohibitively expensive to obtain a statistically significant sample ($N \sim 50$) of high resolution ($R \sim 40,000$) spectra of objects at this distance, it is possible to use the moderate resolution ESI spectra ($R = 7,000$) to measure a number of abundance ratios in metal-poor stars, including C, Mg, Ca, Ti, Fe, Sr, and Ba (Lai et al. 2004; Lai et al. 2007). A red giant at ~ 30 kpc needs about a 1.5 hour exposure using ESI to get the desired S/N of 75 to 100 per pixel to carry out these abundance ratio measurements.

A similar program would be a perfect fit to MOBIE used in echellette mode. For this study the most interesting spectral lines span from the CN band at 3880 Å to the oxygen triplet at 7770 Å. A narrower wavelength range would also be acceptable, though it should span at least from 4000 to 7000 Å to get multiple absorption lines. $R \geq 7000$ will be needed to measure the desired absorption features.

The combination of TMT+MOBIE would enable explorations of red giants out to far greater distances, probing regions where accretion may play an even more important role, and allowing for a true census of chemical abundances throughout the halo.

3.2.2 Sample Selection

Spectroscopic surveys like SEGUE can target stars for kinematics and bulk metallicities much fainter than can be used for detailed abundance determinations on existing telescopes. The fainter candidates from these surveys can provide targets for TMT+MOBIE.

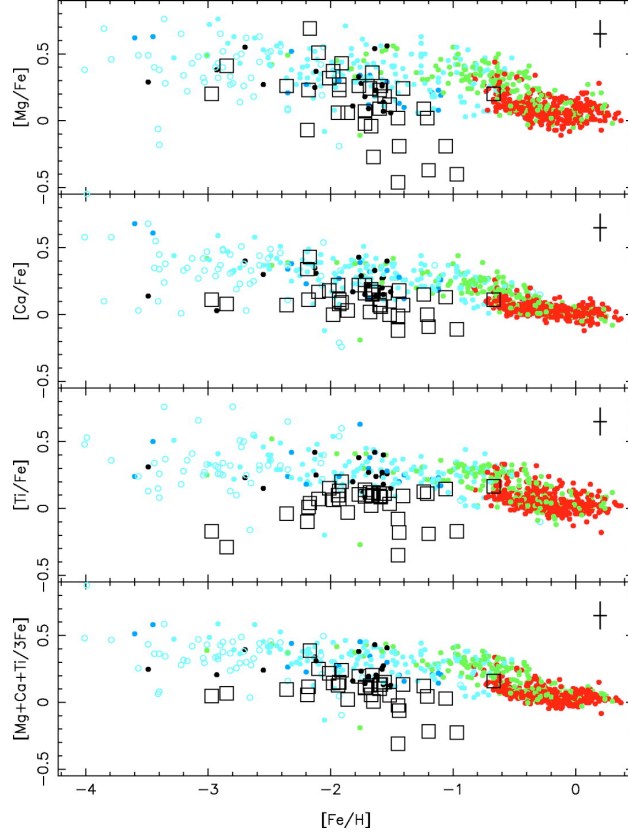


Figure 6: In this figure taken from Venn et al. (2004), abundances of nearby stars are shown as the colored circles, and abundances from individual dSph stars as the squares. It is clear that the abundance ratios of these metal-poor dSph stars are offset from the nearby sample.

3.2.3 Pre-imaging

None required.

3.2.4 Mask Design

Very metal poor stars are extremely rare, so we would have at most a few of these objects per MOBIE field of view. We can also target fields with known halo substructure discovered in the kinematic surveys. The substructure metallicity distributions are likely to have some overlap with that of the smooth halo, making it difficult to unambiguously determine membership. The best tracers of distant substructure for this project are rare, evolved red giant stars, so there will be less than 10 good candidate members per MOBIE field of view.

3.2.5 Required Integration Time

According to the ETC, a star that takes a 2 hour ESI exposure would only need 15 minutes on MOBIE to obtain equivalent S/N. An exposure time of two hours, similar to that required to obtain equivalent S/N as ESI at 20 kpc, would allow MOBIE to probe out to distances of 70 - 100 kpc. This would make it possible to collect a sample of $N \approx 50$ stars in this halo region in a modest amount of observing time.

3.2.6 Target Acquisition

No special requirements beyond normal slitmask or longslit observing procedures.

3.2.7 Calibration Data Acquisition

Standard arc and flat lamp exposures.

3.2.8 Facility Requirements

No special constraints.

3.3 Resolved Stellar Populations in the Local Group

3.3.1 Background

Over the last decade or so, individual red giant branch (RGB) stars in distant Local Group galaxies, including the Andromeda spiral galaxy (M31) and its dwarf satellites, have been targeted for moderate- to high-resolution ($\mathcal{R} \lesssim 8000$) spectroscopy with multi-object spectrographs on 8m-class telescopes. At the distance of M31, $d \approx 800$ kpc, the brightest RGB stars have apparent magnitudes in the range $20 \lesssim I \lesssim 22$ and are thus within reach of current large telescopes and their spectrographs: e.g., DEIMOS, LRIS, and ESI on Keck, FORS on VLT, and IMACS on the Magellan telescope (Côté, Oke & Cohen 1999; Reitzel & Guhathakurta 2002; Reitzel et al. 2004; Ibata et al. 2004; Guhathakurta et al. 2005ab). Spectroscopy of RGB stars in Local Group galaxies has allowed astronomers to broadly characterize the halo dynamics of the parent galaxies and to place rough constraints on their chemical abundance distribution. For years to come, observations of this sort will continue to offer our best hope of reconstructing the history of past mergers, star formation and chemical enrichment in the local universe. However, further progress in these key areas is now becoming limited by the light-collecting power of existing telescopes.

The brightest RGB stars have relatively low effective temperatures so it makes sense that the spectroscopy to date has tended to be carried out in the $0.6 - 0.9\mu\text{m}$ wavelength range. The near infrared Ca II absorption triplet feature at $\sim 0.85\mu\text{m}$ is the most prominent spectral features for cool stars in this wavelength range. In most spectroscopic experiments, one can trade off spectral resolution for signal-to-noise. Such a trade-off is not possible in the Ca II triplet region: the veritable “forest” of bright telluric emission lines would render the spectrum useless at low resolution. The path to progress for such projects involves improving the signal-to-noise ratio at a fixed (high) spectral resolution by increasing the light collecting area of the telescope. Thus, TMT and MOBIE will allow a giant leap forward compared to present-day telescopes and instruments.

Current hierarchical structure formation models predict that the halos of large galaxies are assembled via the merging/accretion of small stellar subsystems over a substantial fraction of the Hubble time (e.g., Bullock, Kravtsov, & Weinberg 2001; Bullock & Johnston 2005; Font, Johnston & Bullock 2005). There is unmistakable evidence for the ongoing tidal disruption of dwarf satellite galaxies in both the Milky Way and M31 (see, e.g., Ferguson et al. 2002). While our internal perspective makes it difficult to study the structure within our own Galaxy, M31 is ideal because: (1) we have a global external view; (2) its disk is close to edge-on; and (3) it is close enough for us to study individual stars in detail. Wide-field photometric and spectroscopic studies have revealed a substantial amount of substructure in the region within ~ 30 kpc of M31’s center (Ferguson et al. 2002), including a giant tidal stream whose progenitor remains unknown (Ibata et al. 2004; Guhathakurta et al. 2005b), and the existence of a stellar halo extending out to a projected radius of ~ 150 kpc (Guhathakurta et al. 2005a). A detailed characterization of the dynamics and metallicity of these substructures will provide key tests of structure formation theories on sub-galactic scales. Indeed, state-of-the-art numerical simulations of halo assembly predict a wealth of kinematic and chemical substructure within the halos of massive galaxies such M31, with the recent simulations of Fardal et al (2008) able to reproduce a multitude of observed features in the outer parts of M31 through the accretion of a single galaxy. If this is valid, it would remove the concern of why the merger activity recently in M31 seems to be much more active than it does in the Milky Way, but extracting the history of mergers, star formation and chemical enrichment will likely require spectroscopy for many thousands of of RGB stars (see also Figure 7).

3.3.2 Planning of observations

At present, spectroscopic observations are limited by the fact that even long exposures on the largest telescopes and most efficient spectrographs (e.g., Keck+DEIMOS) can reach only about two magnitudes below the tip of the RGB population in M31, to $I \sim 22.5$. By maintaining a throughput of $\geq 30\%$ over the $0.34 - 1.0\mu\text{m}$ region, TMT and MOBIE will be able to reach ~ 2.5 mag deeper in the same exposure time, reaching down to the level of the horizontal branch (HB) and allowing an extensive spectroscopic campaign to study the dynamics and metallicities of stars in the outer halo of M31. The steep rise in the RGB luminosity function to faint magnitudes, and the presence of a well-populated HB, means that the surface density of possible targets will be at least ten times higher than is available at present. Figure 8 shows CMDs for three halo fields based on V/I imaging from Keck+LRIS. For these particular field locations — at projected distances of $\approx 2^\circ \approx 27$ kpc from the center of M31 — the surface density of RGB stars within the reach of 8m-class telescopes is $\Sigma_{\text{RGB}} \sim 10 \text{ arcmin}^{-2}$. By contrast, with a limiting magnitude of

$I \sim 25.5$, we expect $\Sigma_{\text{RGB}} \sim 100 \text{ arcmin}^{-2}$ for MOBIE, or roughly 4,000 accessible RGB stars per MOBIE field (see Table 3.3.2).

Table 2: RGB Candidates in M31

I (mag)	$\langle I \rangle$ (mag)	$N(I)^\dagger$	$\Sigma_{\text{RGB}}(I)$ (arcmin^{-2})	$N(\leq I)^\dagger$	$\Sigma_{\text{RGB}}(\leq I)$ (arcmin^{-2})
20.5-21.0	20.75	48	1.2	48	1.2
21.0-21.5	21.25	96	2.3	144	3.5
21.5-22.0	21.75	107	2.6	251	6.1
22.0-22.5	22.25	173	4.2	424	10.2
22.5-23.0	22.75	266	6.4	690	16.6
23.0-23.5	23.25	385	9.3	1075	25.9
23.5-24.0	23.75	484	11.6	1559	37.5
24.0-24.5	24.25	645	15.5	2204	53.0
24.5-25.0	24.75	831	20.0	3035	73.0
25.0-25.5	25.25	1052	25.3	4087	98.3

† – Number RGB stars per MOBIE field, for locations of $(\pm 22, \pm 15)$ kpc along the disk major and minor axes, respectively.

Detailed studies of the elemental abundance patterns in Milky Way stars have taught us a great deal about the star formation history of our Galaxy. With MOBIE, we are on the brink of being able to make similar measurements in another large spiral galaxy, M31. But even with the world’s largest optical telescope (Keck 10m), one of the most efficient spectrographs available (DEIMOS), and relative long integration times (1–3 hr), it is difficult to achieve signal-to-noise ratios greater than about 15 per \AA for M31’s RGB stars. This S/N is simply not high enough to permit a detailed chemical abundance analysis. In order to improve the S/N ratio, it is necessary to add spectra for RGB stars deemed to be similar based on their location within the CMD. This approach, unfortunately, greatly complicates the interpretation of the spectra because there is no guarantee that the stars had identical physical properties. With TMT+MOBIE, this problem will be solved by allowing us to obtain spectra of *individual* RGB stars in M31 with $S/N \gtrsim 40$ per \AA (see Figure 9).

As a demonstration of the scope of Local Group project which MOBIE will make possible, we consider an ambitious survey of the M31 halo. The aim of this program is to explore the history of mergers, star formation and chemical enrichment in the M31 halo from radial velocities (accurate to $5\text{--}10 \text{ km s}^{-1}$) for 20,000 RGB stars (covering a 3 deg^2 field) and high-quality abundances for a subset of 4,000 stars (over a 0.9 deg^2 field).

Abundances:

Elemental abundances measurements at the maximum spectral resolution of MOBIE (~ 7800) require a minimum signal-to-noise (S/N) ratio of ~ 40 per \AA in order to be useful for abundance analyses extending beyond just a determination of overall metallicity. The richness of the field is in relative abundances, hence the high maximum resolution of MOBIE will be crucial. At this resolution, the target S/N ratio is reached (in both the red and blue arms) in exposure times of 4 hours for RGB stars with $I = 21.3$. For a typical halo field, the surface density of RGB stars brighter than this is $\Sigma_{\text{RGB}} \sim 2.6 \text{ arcmin}^{-2}$, or ~ 110 per MOBIE field. If a nod and shuffle approach is implemented so that most of these stars can be observed during a single setup (single-order mode with the highest resolution), then a total of $(4,000/110) \times 3 = 110$ hours (≈ 17 nights) would be required to amass a sample of 4,000 stars. Because the spectra have roughly the same S/N in both arms, it will be possible to measure abundances for both the red and blue spectra. To do so most efficaciously, we target the $0.46 - 0.52 \mu\text{m}$ and $0.8 - 0.9 \mu\text{m}$ spectral regions which contain numerous strong absorption lines. These calculations assume a slit width of $0''.8$ and seeing of $0''.8$ (FWHM) at $0.52 \mu\text{m}$ and $0''.6$ at $0.85 \mu\text{m}$. Gilbert et al (2007) have demonstrated that it is possible to efficiently separate M31 giants from foreground Galactic stars and background galaxies, while Kirby, Guhathakurta & Sneden (2008) have developed and demonstrated new techniques to extract metallicity from moderate resolution spectra of M31 giants taken by DEIMOS.

Dynamics:

Unlike the chemical abundances portion of the survey, which focuses on long (4 hour) exposures of bright ($I \leq$

21.3) RGB stars, the radial velocity survey targets fainter stars ($I \leq 23$), using shorter exposures (1 hour) to cover a wider area (3 deg^2). The spectral resolution will be reduced to ~ 5000 as the primary science goal in this case is the measurement of radial velocities. A signal-to-noise ratio of $S/N \gtrsim 5$ per \AA is adequate to measure velocities good to $\epsilon_v \approx 6 \text{ km s}^{-1}$, which should allow the identification of moving groups, tidal streams and other sub-structures, as well as mass modeling of the dark matter distribution within the M31 halo. The surface density of suitable ($I \leq 23$) RGB stars is $\Sigma_{\text{RGB}} \sim 16.6 \text{ arcmin}^{-2}$, or ~ 670 per MOBIE field. If a nod and shuffle technique can be used to provide a slit length of $4''$ or less, then each 1 hour exposure should yield red and blue spectra for $(380''/4'') = 140$ stars per field. Measuring velocities for 16,000 stars (to be added to the 4,000 observed as part of the abundance program) would require $(16,000/140) \times 1 = 114$ hours (≈ 16 nights) assuming that 7 fields could be observed during a typical night. As above, we target the $0.46 - 0.52 \mu\text{m}$ and $0.8 - 0.9 \mu\text{m}$ spectral regions simultaneously. These calculations assume a slit width of $0''.8$ and seeing of $0''.8$ (FWHM) at $0.52 \mu\text{m}$ and $0''.6$ at $0.85 \mu\text{m}$. The abundance survey makes good use of the highest spectral resolution mode that MOBIE can achieve.

3.3.3 Pre-imaging

Pre-imaging should be taken with MOBIE only as a last resort: target RGB stars can be identified, and their coordinates measured, using multi-color imaging from 8m-class telescopes. If the targets must be selected from MOBIE images, then standard broadband filters (Johnson, SDSS) or order-sorting filters would be adequate for this purpose.

3.3.4 Mask design

The observations are not time critical, so there is no need to fabricate masks on short timescales. In fact, the pre-imaging should be taken well in advance to ensure that ample time is available for mask design. Since even the faintest RGBs targeted in this program are well within the reach of optical/IR cameras on 8m-class telescopes, it is essential that the mask design software/hardware be flexible enough to use astrometry from other facilities.

3.3.5 Procedures during the day

There are no special requirements, aside from the need to efficiently measure the positions of the alignment boxes and slit positions in several different masks. In some cases, seven or more fields will be observed each night, so it is important that this procedure should take no more than a few minutes per mask.

3.3.6 Procedures during twilight

No special twilight procedures necessary.

3.3.7 Target acquisition

Field acquisition should rely on the usual approach of positioning and aligning each mask with the aid of a half dozen or so bright reference stars. Many stars of suitable brightness should be available in the direction of M31, which has a Galactic latitude of $b_{\text{II}} \approx -22^\circ$. The slitmask alignment procedures must be optimized to minimize the time lost as up to seven slitmasks will be used per night.

3.3.8 Target science data acquisition

The two components of the survey require roughly equal allocations of observing time: about 15 nights each. Thus, one month of observing time is needed to observe the full sample of 20,000 RGB stars, distributed over the complete 3 deg^2 field, with accurate abundances for a subset of 4,000 of the brightest stars.

3.3.9 Calibration data acquisition

No special calibrations are required, apart from radial velocity standard stars to establish and monitor the zero-point of the velocities. The portion of the program which requires abundances will require reasonably good relative flux calibration, which may entail observing a few spectrophotometric standard stars.

3.3.10 Facility requirements

No special facility requirement necessary.

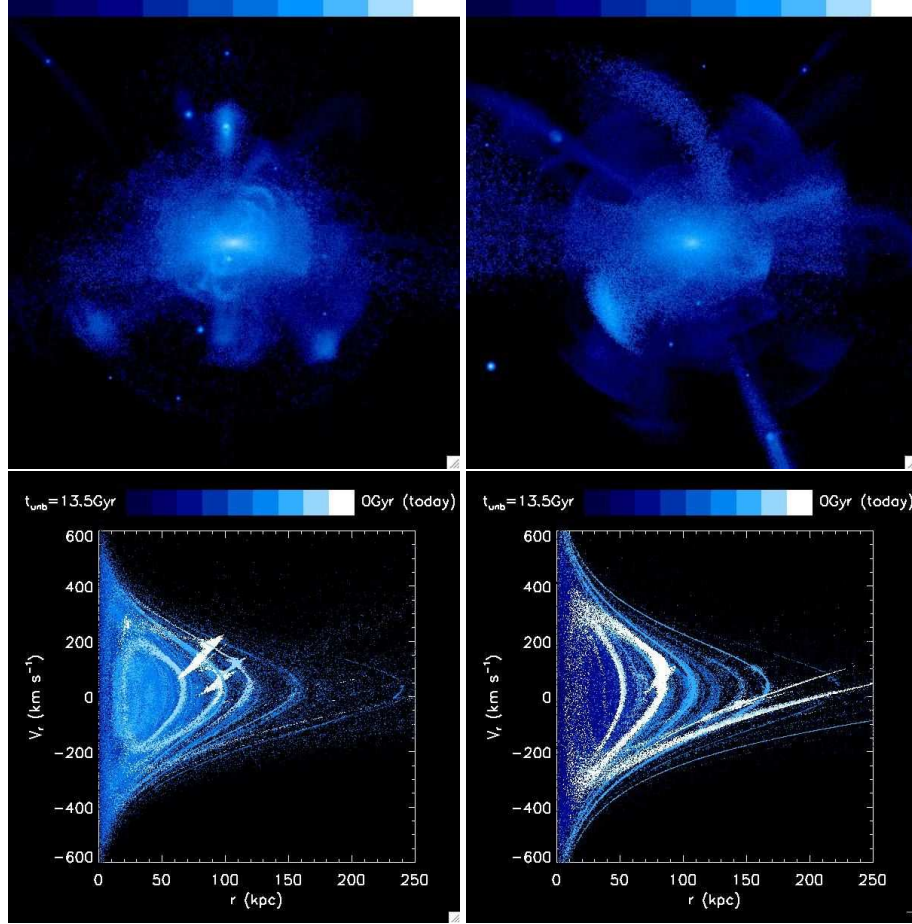


Figure 7: (*Upper Panels*) Two different halo simulations generated using a semi-analytic plus N-body approach. Each box measures 300×300 kpc. The blue/white color scale indicates surface brightness: $23 \text{ mag arcsec}^{-2}$ (white) to $38 \text{ mag arcsec}^{-2}$ (dark blue). (*Lower Panels*) Radial phase space diagrams (v_r vs r relative to the host halo center) for the two halos shown above. Each point represents 1000 solar luminosities. The color code reflects the time each particle became unbound to its parent satellite. White points are either bound or became unbound in the last 1.5 Gyr, while dark blue points became unbound more than 12 Gyr ago. The radial color gradient reflects the tendency for inner halo stars to be accreted (and stripped) early in the galaxy's history. The white feature at $r \sim 80$ kpc in the right panel represents a massive, and very recent, disruption event. Figures and description from Bullock & Johnston (2005).

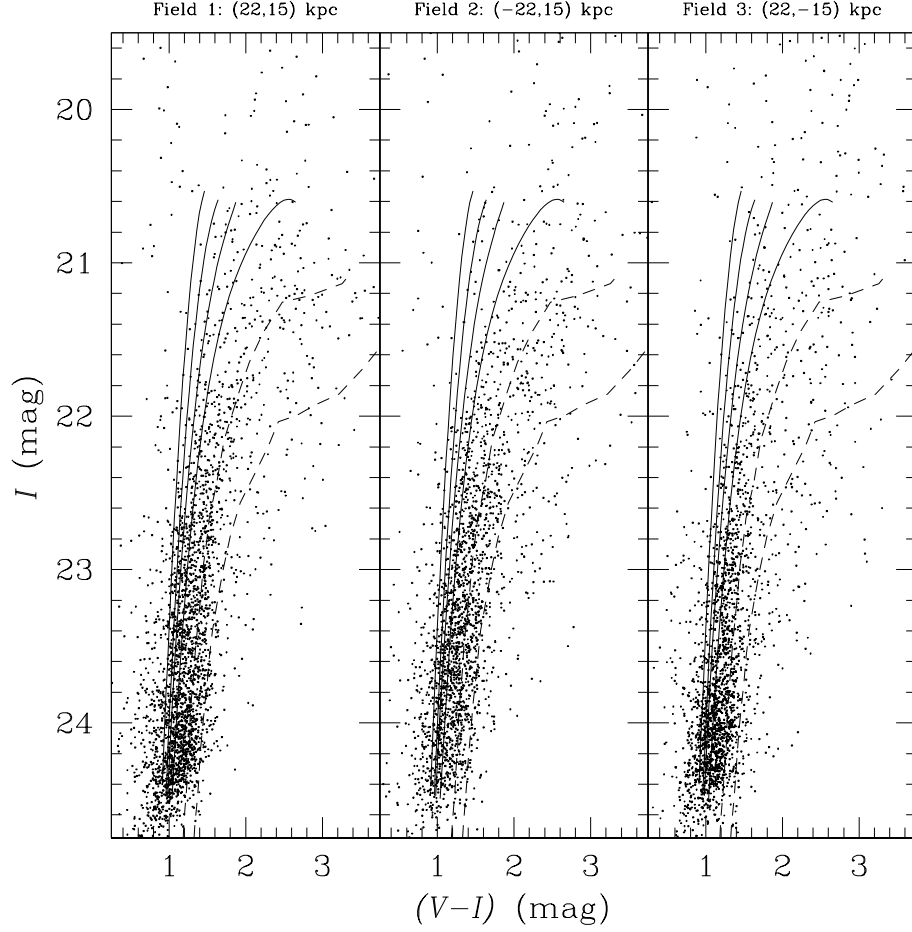


Figure 8: Color magnitude diagrams for three Keck/LRIS fields in the halo of M31. Distances along the major and minor axes are labeled at the top of each panel. The solid curves show fiducial sequences for Galactic globular clusters of metallicity $[\text{Fe}/\text{H}] = -2.12, -1.62, -1.26$ and -0.76 . The dashed curves show 14 Gyr isochrones from Bertelli et al. (1994) with $[\text{Fe}/\text{H}] = -0.4$ and 0.0 . Each of these sightlines contains ≈ 500 RGB stars brighter than $I \sim 22$ within an area of $\sim 80 \text{ arcmin}^2$, the appropriate values for Keck+DEIMOS. TMT+WFOS will reach $I \sim 25.5$, giving a total of 4,000 accessible RGB stars within its $\sim 40 \text{ arcmin}^2$ field of view.

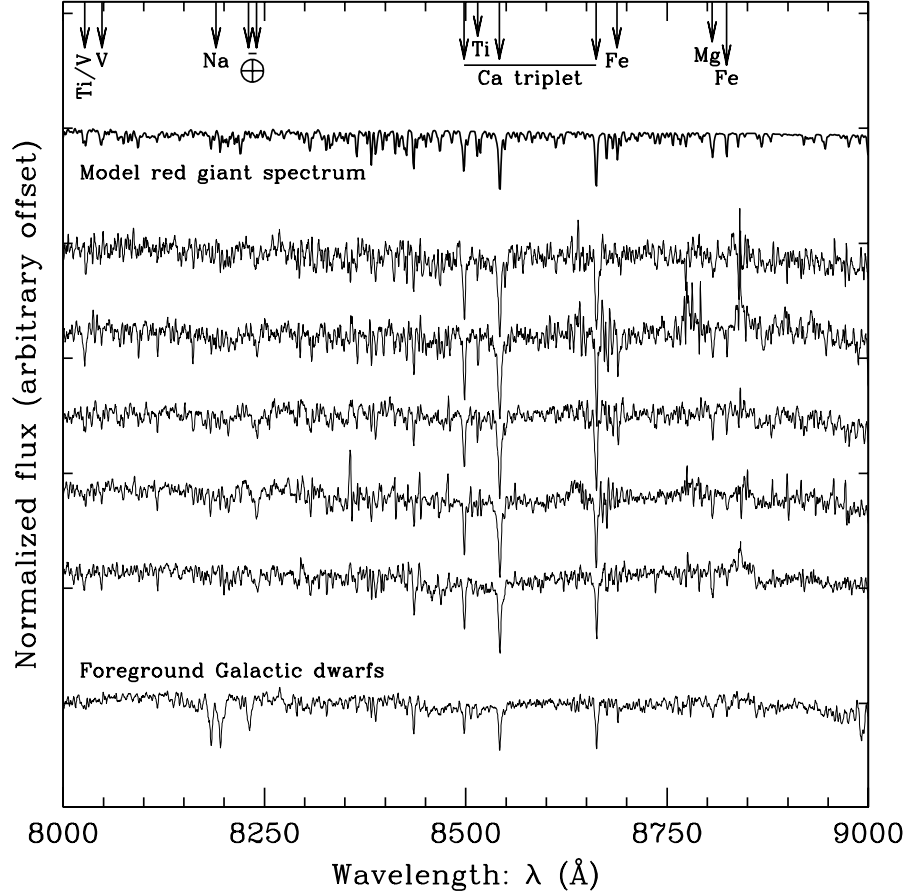


Figure 9: Montage of co-added Keck 10-m/DEIMOS spectra (thin solid lines) showing the region around the Ca II triplet, normalized and shifted to rest-frame wavelength and smoothed with a 1.7\AA weighted boxcar. The bottom spectrum is a co-add of 16 foreground Galactic dwarf stars, each with an exposure time of 1 hr. The next five spectra are co-adds of about a dozen M31 RGB stars each, again each with an exposure time of 1 hr, grouped and ordered by predicted Ca II line strength (increasing upward) as estimated from the CMD-based photometric metallicity and luminosity. The bold line at the top is a model red giant spectrum with $T_{\text{eff}} = 4000\text{ K}$, $\log(g) = 1.5$, and $[\text{Fe}/\text{H}] = -0.3$ from Schiavon & Barbuy (1999). A few prominent spectral features of RGB stars are identified along with the $\lambda 8190\text{\AA}$ Na I doublet, which is strong in dwarfs. The S/N in the co-added spectra, typically 50 per \AA , is barely adequate for abundance analysis and the interpretation is complicated by the fact that these are co-added spectra. The TMT+MOBIE combination will produce much higher quality spectra for *individual* M31 RGB stars of this apparent magnitude ($I \sim 21$) in 2–3 hour exposures, allowing the determination of elemental abundances (e.g., $[\alpha/\text{Fe}]$ constraints) for many thousands of M31 halo field stars.

3.4 The Dark Matter Distribution in Nearby Elliptical Galaxies

3.4.1 Background

Cosmology has entered a new era, highlighted by recent satellite and balloon missions to study the cosmic microwave background radiation. Boomerang, WMAP, and the upcoming Planck mission, have probed (or will soon probe) temperature fluctuations in the radiation field down to a millionth of a degree or less. The fluctuations observed by WMAP provide a spectacular confirmation of the standard cosmological model, in which a spatially flat, isotropic and homogeneous universe is composed of ordinary matter, dark energy and dark matter.

The existence of this latter component, which may comprise as much as 90% of the mass in the universe, gained widespread acceptance by the astronomical community in the mid 1970s. But despite three decades of study, dark matter remains a mystery. It is detectable only through its gravitational effects, and through gravity it controls the formation of virtually all structures in the universe, from super-clusters down to the smallest galaxies. At present, the dominant paradigm for structure formation is the family of cold dark matter (CDM) models, in which the random motions of the dark matter particles are assumed to be much slower than the speed of light. These models provide a remarkably accurate description of the universe on scales larger than ~ 1 Mpc.

However, these same models fail by a wide margin to match observations on the much smaller scales of galaxies. According to the models, the Milky Way should be enveloped in a swarm of several hundred low-mass galaxies, yet exhaustive searches have uncovered only one or two dozen such companions. It is only with the aid of the Sloan Digital Sky Survey that very recently evidence for a substantial number of new satellites to the Milky Way has emerged (see, e.g. Belokurov et al 2006). If one multiplies the new discoveries by the fraction of the sky not surveyed by the SDSS, taking into account the detection efficiency for finding a low luminosity satellite in the SDSS data as a function of distance and total luminosity of the satellite quantified by Koposov et al (2008), this problem may finally be on the way to solution.

Equally perplexing, kinematic observations of galaxies suggest that the inner density profiles of their dark matter halos are significantly shallower than the model predictions. It is unclear if this latter discrepancy represents a failure of the models or limitations in the observations. Very recently Romano-Diaz et al (2008) have suggested a mechanism previously neglected in the models that may erase the previously predicted dark matter cusps at the centers of galactic halos with baryons.

It is certainly true that attempts to measure dark matter mass profiles for galaxies have produced strongly conflicting results, with claims ranging from dark matter halos that fall steeply with distance from the galaxy center (as expected in CDM models) to dark matter halos with constant-density cores (at odds with the theoretical predictions). But almost all conclusions on the structure of dark matter halos rest on observations of the same *kind* of galaxies: flattened, gas-rich spirals. Very little is known about the dark matter distribution in elliptical galaxies, which are common in the field and which dominate rich galaxy clusters found in the low-redshift universe. The reason is simple: unlike spirals, ellipticals contain little or no cold gas, making the measurement of HI rotation curves impossible. In this section we describe a program designed to measure the distribution of dark matter in nearby elliptical galaxies by determining the radial (i.e., line-of-sight) velocities for dynamical test particles orbiting in their gravitational potential wells. The properties of the dark matter halos can then be studied through their gravitational influence on the motions of the embedded test particles.

It is unclear if this latter discrepancy represents a failure of the models or limitations in the observations. It is certainly true that attempts to measure dark matter mass profiles for galaxies have produced strongly conflicting results, with claims ranging from dark matter halos that fall steeply with distance from the galaxy center (as expected in CDM models) to dark matter halos with constant-density cores (at odds with the theoretical predictions). But almost all conclusions on the structure of dark matter halos rest on observations of the same *kind* of galaxies: flattened, gas-rich spirals. Very little is known about the dark matter distribution in elliptical galaxies, which are common in the field and which dominate rich galaxy clusters found in the low-redshift universe. The reason is simple: unlike spirals, ellipticals contain little or no cold gas, making the measurement of HI rotation curves impossible. In this section we describe a program designed to measure the distribution of dark matter in nearby elliptical galaxies by determining the radial (i.e., line-of-sight) velocities for dynamical test particles orbiting in their gravitational potential wells. The properties of the dark matter halos can then be studied through their gravitational influence on the motions of the embedded test particles.

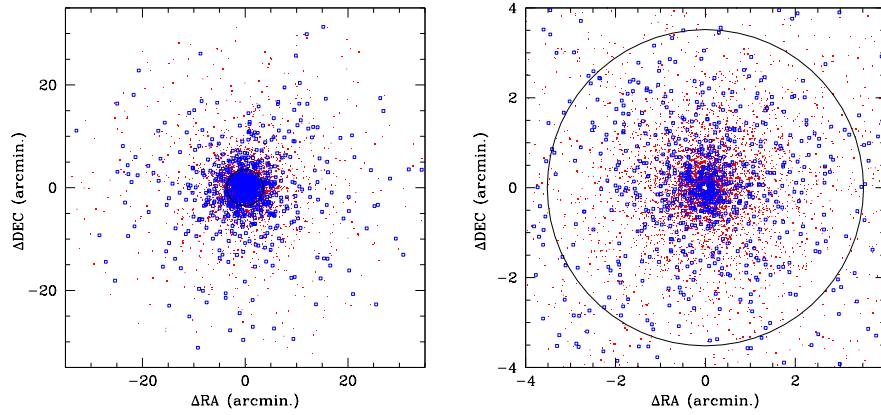


Figure 10: (Left Panel) Simulated spatial distribution of ≈ 6000 globular clusters (red points) and ≈ 1100 planetary nebulae (open blue squares) in M49, the brightest elliptical galaxy in the nearby Virgo Cluster. The circle shows the galaxy’s effective radius of $r_e = 3'.5$. (Right Panel) A magnified view of the central region of M49. Inside the effective radius (large circle), the mean surface density of globular clusters brighter than $V \approx 25$ is $\langle \Sigma_{GC} \rangle = 90 \text{ arcmin}^{-2}$. The mean surface density for planetary nebulae brighter than $m_{5007} \approx 31$ in this same region is $\langle \Sigma_{PNe} \rangle = 16 \text{ arcmin}^{-2}$.

3.4.2 Planning of observations

Reconstruction of the mass distribution in nearby elliptical relies on radial velocity measurements for two independent sets of dynamical test particles: globular clusters (GCs) and planetary nebulae (PNe).

To map out the radial profile of the dark matter mass density, $\rho(r)$, using a system test particles, one must solve simultaneously for the orbital anisotropy of the system of test particles used in the dynamical analysis: $\beta(r) = 1 - \sigma_\theta(r)^2/\sigma_r(r)^2$.⁶ This requires a *minimum* sample of ≈ 1000 radial velocities. If one is willing make some assumptions about the orbital distribution (e.g., that the orbits are isotropic, $\beta \equiv 0$), then this requirement can be relaxed to ≈ 250 velocities (Merritt & Tremblay 1993).

At present, radial velocities for ≥ 250 GCs have been amassed for just three elliptical galaxies: M49, M87 and NGC1399 (Côté et al. 2001, 2003; Richtler et al. 2003). These were obvious first targets for multi-object spectrographs on 8m-class telescopes since they are the nearest ellipticals with rich GC systems. But for these same reasons, they constitute a biased sample in terms of luminosity and environment: *i.e.*, they are among the brightest galaxies in the Local super-cluster and occupy unique locations in the highest density regions of the Virgo and Fornax Clusters. The situation is even more limited in the case of PNe: in only a single galaxy (NGC5128) does a sample of more than 250 PNe velocities exist (Peng et al. 2004).

The existing observations for these galaxies — along with those for a handful of other galaxies having still smaller radial velocity samples of GCs and PNe — paint a confusing picture about the structure of dark matter halos. Some galaxies appear to be dark matter dominated at their effective radius, r_e , while others seem to show no evidence at all for dark matter out to $r \lesssim 4r_e$ (Napolitano et al. 2005). To elucidate the shape and extent of the dark matter halos in elliptical galaxies, and to examine the dependence of halo properties on galaxy environment, a radial velocity survey of thousands of GCs and PNe in a much expanded sample of galaxies is required.

Table 3 compares the number of elliptical galaxies from the Catalog of Nearby Galaxies (Tully & Fisher 1988) for which radial velocity surveys to a limiting magnitude of $V_{\text{lim}} = 22.7$ would yield minimum radial velocity samples of 250 and 1000 GCs. Note that this is the approximate limiting magnitude for GC radial velocity surveys with 8-10m telescopes. Table 3 shows that, at the present time, samples of this size can be collected for 18 and 4 ellipticals, respectively. With the limiting magnitude of $V_{\text{lim}} \approx 25.5$ expected with MOBIE (see below), these samples increase by an order of magnitude: to 179 and 49 galaxies, respectively. Similarly dramatic gains are found for PNe. In short, MOBIE opens a realm of study which will never be accessible with multi-object spectrographs on 8-10m class telescopes.

⁶Here $\sigma_\theta(r)$ and $\sigma_r(r)$ are the intrinsic velocity dispersions in the tangential and radial directions relative to the galaxy center.

Table 3: aGlobular Clusters in Elliptical Galaxies

V_{lim} (mag)	$N_{\text{GC}} \geq 250$	$N_{\text{GC}} \geq 1000$	$\langle \sigma_0 \rangle$ (km s ⁻¹)
22.7	18	4	203±34
25.5	179	49	163±28

Note that the final column of Table 3 gives an estimate of the mean projected central velocity dispersion, $\langle \sigma_0 \rangle$. This sets the required velocity precision: it is important that the uncertainties on individual velocity measurements, ϵ_v , be no more than $\approx 1/10$ th the system’s intrinsic velocity dispersion, or $\epsilon_v \leq 15\text{--}20 \text{ km s}^{-1}$.

Globular Cluster Observations: GC systems have a near-Gaussian magnitude distribution, with $M_V \approx -7.4$ and dispersion $\approx 1.4 \text{ mag}$. At the distance of M49, the GC luminosity function “turns over” at $V \approx 23.8$. With limiting magnitudes of $V_{\text{lim}} \approx 22.7$, existing radial velocity surveys with 8m-class telescopes have sampled only a tiny fraction of the GC luminosity function. Figure 10 shows one simulation of the spatial distribution of the ≈ 6000 GCs which belong to this galaxy. The surface density of GCs varies sharply over the field: from $\Sigma_{\text{GC}} \geq 100 \text{ arcmin}^{-2}$ in the galaxy core, to $\Sigma_{\text{GC}} \sim 1 \text{ arcmin}^{-2}$ beyond $10'$. Since most clusters are found within the central $\sim 40 \text{ arcmin}^2$, and because the simultaneous determination of $\rho(r)$ and $\beta(r)$ requires the measurement of the velocity dispersion profile over the largest possible range in galactocentric distance (see the lower left panel of Figure 12), it is important to achieve the highest possible slit densities to maximize survey efficiency.

The best strategy would be to employ a dual approach of: (1) using nod and shuffle to minimize slit length; and: (2) “stacking” the spectra on the detector with the aid of a band-limiting filter that isolates the spectral region of interest. Since each GC will be observed simultaneously in the blue and red arms, there are two relevant spectral regions: $0.47\text{--}0.54 \mu\text{m}$ in the blue, and $0.83\text{--}0.88 \mu\text{m}$ in the red. In the blue arm, a resolution of $\mathcal{R} \approx 2000$ will provide adequate velocity precision ($\epsilon_v \approx 20 \text{ km s}^{-1}$ or better) and at the same time allow the measurement of GC ages and metallicities. In the red arm, a higher resolution ($\mathcal{R} \approx 5000$) is required to suppress the noise from bright sky lines in the region of the Ca II triplet.

Table 4 lists some of the spectral lines of interest. While the primary goal of this program is the dynamics of the GC system, such spectra would be valuable probes of the history of star formation and chemical enrichment in the host galaxy. Doing so will require good flux calibration, although this is unimportant for radial velocity measurements.

The upper panel of Figure 11 shows blue spectra for a representative sample of simulated GCs, obtained with MOBIE in a single 1 hour exposure. The distribution of velocity errors is shown in the lower panel. For these calculations, the slit width has been matched to the assumed seeing of $\text{FWHM} = 0''.8$.

Table 4: Instrumental Configurations

Arm	Globular Clusters			Planetary Nebulae		
	\mathcal{R}	λ Coverage ^a (μm)	Diagnostics	\mathcal{R}	λ Coverage (μm)	Diagnostics
Blue	2000	0.47–0.54	Mg I 5167, 5172, 5183 H β 4861	2000	0.36–0.51	[O III] 5007, 4959 [O II] 3727 H β 4861, H γ 4342
Red	5000	0.83–0.88	Ca II 8498, 8542, 8662	5000	0.58–0.69	H α 6563 [N II] 6548, 6584

^a - Pre-filters could be used to double the effective slit density, depending on the length of spectra at each resolution.

Planetary Nebula Observations: At the distance of M49, the PN luminosity function shows an abrupt onset at $m_{5007} \approx 26.6$ and rises sharply to fainter magnitudes⁷. Since the distribution of PNe follows the brightness profile of the underlying galaxy, the surface density of sources varies significantly with radius. For sources brighter than $m_{5007} \approx 31$ — the approximate limiting magnitude for TMT+MOBIE in a single 1 hour exposure — the mean

⁷Note that m_{5007} is the magnitude in a narrow-band filter centered on 5007\AA .

surface density is $\Sigma_{\text{PN}} \sim 16 \text{ arcmin}^{-2}$ within the galaxy's effective radius ($r_e = 3'.5$). As with the GCs, short slits are required to maximize slit density and boost observing efficiency.

The PNe observations would be carried out simultaneously with the MOBIE blue and red arms, using the $\mathcal{R} \approx 2000$ and 5000 configurations, respectively. Table 4 summarizes the important spectral features. With this instrumental configuration, the PNe spectra will contain enough lines to discriminate unambiguously between bonafide PNe and background $\text{Ly}\alpha$ galaxies, which are the most severe contaminant in PNe samples. (This would be done by requiring the simultaneous detection of [O III] and $\text{H}\alpha$ in the blue and red arms.) The spectral resolution and large number of emission lines between [O II] 3727Å and [N II] 6548, 6584Å would also allow the measurement of chemical abundances for individual PNe, giving a first glimpse into the dependence of stellar orbits on age and metallicity in elliptical galaxies. Note that, unlike the situation with the GCs, it is important to reach the [O III] 3727 Å line, both to confirm the PNe identification and to measure abundances. For this aspect of the program, good relative flux calibration is a necessity.

Figure 11 shows representative spectra for three simulated PNe in M49, based on a 1 hour integration with TMT+MOBIE. For these calculations, the slit width has been matched to the assumed seeing of $\text{FWHM} = 0''.8$. The difference between the input and measured radial velocity is plotted against S/N in the [O III] line in the lower right panel of this figure. As with the GCs, we conclude that $\text{S/N} \geq 1$ is adequate to measure velocities of the required precision for even the faintest objects.

3.4.3 Pre-imaging

PNe are faint, emission-line objects which are identified using an on-band/off-band approach to isolate the [O III] 5007Å line and the adjacent continuum with the aid of narrow-band filters. If narrow-band imaging is available with MOBIE, it would be possible to identify the PN candidates using images taken on the blue arm of MOBIE; however, such observations are probably more efficient using a wide-field imager on an 8m-class telescope. While the pre-imaging for the GCs can also be done with MOBIE itself, this is not a necessity: in other words, it is important to retain the option of using pre-imaging either from MOBIE, or from some other telescope/camera combination.

At the distance of Virgo, 95% of the GCs will have apparent magnitudes in the range $20.9 \lesssim V \lesssim 26.5$, and are unresolved in typical ground-based seeing conditions. Thus, confusion with foreground stars or compact background galaxies is obviously an issue which needs to be considered. At the bright end of the GC luminosity function, stars are the dominant source of contamination; at the faint end, unresolved galaxies are the primary concern. In practice, the contamination is usually negligible near the peak of the GC luminosity function, at least for the bright galaxies. For fainter galaxies, contamination can be important at all magnitudes. Rejecting stars and galaxies can be done in a two-color diagram, and SDSS or Johnson filters would be adequate for this purpose. A wide color baseline is needed to separate effectively the stars and galaxies from the GCs: $(g - r)$ vs. $(r - i)$ or $(u - r)$ vs. $(r - i)$.

3.4.4 Mask design

The observations are not time critical, so there is no need to fabricate masks on timescales of days or hours. In fact, the selection of targets may be non-trivial so the pre-imaging should be taken well in advance to ensure that ample time is available for mask design. The ability to place a large number of slits within each field — and maintain accurate sky subtraction at the same time — is the essential element of this program.

It is important that the mask fabrication process be flexible enough to accept pre-imaging from MOBIE or some other facility. This would require accurately mapping the geometric distortion in the focal plane during instrument commissioning; indeed, this will be *essential* for the PNe observations (see §6.3.3). Although the choice of slit width will depend on the observing conditions and the requisite velocity precision, it will normally fall in the range $0''.4\text{--}0''.8$.

Due to the high surface densities of GCs in the inner regions of the galaxy (i.e., see Figure 10), it would be advantageous (if possible) to boost the effective slit density by inserting a blocking filter which restricts the wavelength range to $0.47\text{--}0.54\mu\text{m}$, thereby doubling the effective slit density. Depending on the cosmic-ray rate, lunar phase and object magnitude, total exposure times may be as short as ≈ 0.5 hour. It is therefore a requirement that as many as ten masks be available for use on any given night.

3.4.5 Procedures during the day

To minimize field acquisition time, it will be necessary to accurately measure the location of the reference pinholes and slit positions in the various masks. This should be done during the afternoon, after the masks have been loaded, by taking short images of the illuminated masks with no dispersing element in place.

3.4.6 Procedures during twilight

No special twilight procedures necessary.

3.4.7 Target acquisition

The Galactic latitude of M49 is $b_{\text{II}} \approx 70^\circ$, so the number of suitable reference stars may be limited. It should be possible to measure the centroids of these stars on the detector to the 1–2 milliarcsecond level in an exposure of ≈ 10 s. As many as ten masks may be used in a single night, so the acquisition time should be minimal. Once the telescope has slewed to the target field, the alignment process should take no more than 3 minutes.

3.4.8 Target science data acquisition

The upper panels of Figure 12 show the simulated luminosity functions of GCs and PNe in M49 (open histograms). The hatched histograms show all objects for which a single 1 hour exposure with the blue arm of MOBIE would yield $S/N \geq 1$, the minimum needed to ensure a velocity precision of $\epsilon_v = 20 \text{ km s}^{-1}$ or better for both the GCs and PNe (see Figure 11). The lower panels of Figure 12 demonstrate how such large radial velocity samples can be used to measure not only the distribution of dark matter but also the orbital properties, $\beta(r)$, of the different tracer populations.

Measuring velocities for the complete samples of GCs (≈ 4000) and PNe (≈ 1000) in M49 which fall into this category (i.e., $S/N \geq 1$ in 1 hour) would require ~ 12 , 1-hour exposures for the GCs and ~ 7 , 1-hour exposures for the PNe. This estimate assumes that a “nod and shuffle” technique can be used to achieve accurate sky+galaxy subtraction with slit lengths of $4''$. For the GCs, we further assume that a filter isolating the $0.47\text{--}0.54\mu\text{m}$ spectral region within a single order can be used to place two banks of spectra across the MOBIE field. Since the total slit length available in each channel of the spectrograph measures $9'.6$, we expect roughly $2 \times (576''/4'') = 280$ slits per GC mask, and about half this number for the PNe masks. Multiple pointings inside the galaxy’s effective radius will be needed because of the high surface densities in this region.

Table 3 shows that about 50 galaxies with suitably rich GC systems are found in the Catalog of Nearby Galaxies. Thus, a comprehensive study of the structure of dark matter halos in these galaxies, based on radial velocity samples of 1000 or more GCs per galaxy, would require a total “open shutter” integration time of $4 \text{ hours} \times 50 \approx 200 \text{ hours}$ (≈ 22 nights).

3.4.9 Calibration data acquisition

Since the program uses radial velocities of discrete objects to derive M49’s velocity dispersion and its variation with radius, it is important that zero-point be stable and easily tied to a standardized reference frame. This is particularly true since velocities derived from masks taken months or years apart will be combined to map out the velocity field. Because the faintest galaxies in Table 3 have (roughly flat) velocity dispersion profiles of $\approx 150 \text{ km s}^{-1}$, we require velocity uncertainties no larger than 15 km s^{-1} . Spectra for radial velocity standard stars should be undertaken each night, perhaps using masks for multiple radial velocity standard stars located in Galactic open or GC fields.

3.4.10 Facility requirements

No special facility requirement necessary.

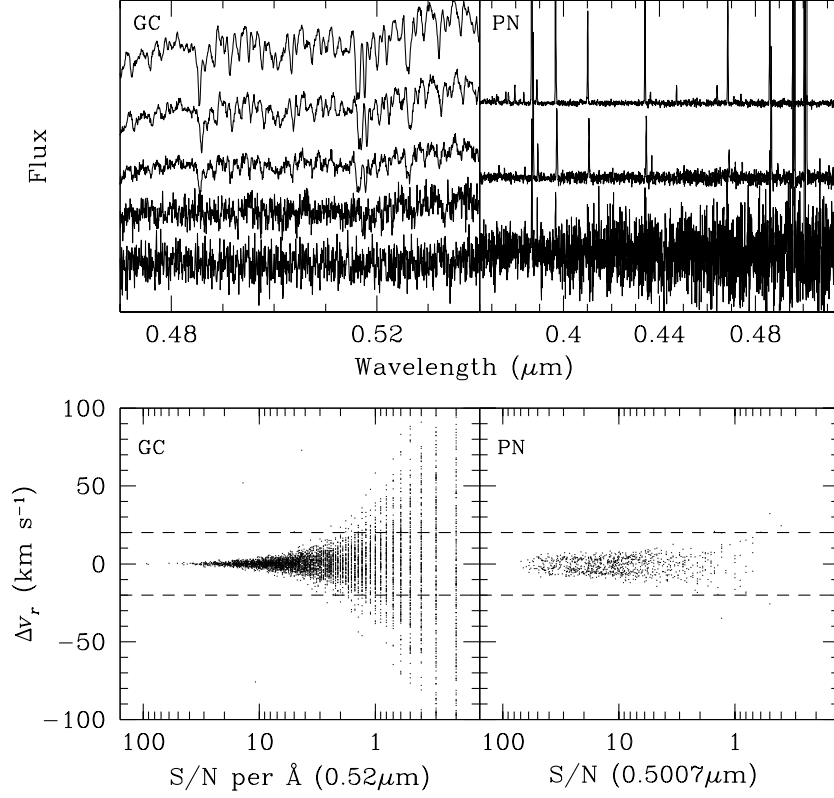


Figure 11: (*Upper Left Panel*) Simulated spectra for five globular clusters in M49, obtained in a 1 hour integration with TMT+MOBIE ($\mathcal{R} \approx 2000$). The plotted spectra show randomly selected GCs with $V = 19.9$ ($S/N = 43$), 21.5 (25), 22.8 (10.5), 23.6 (2.5) and 25.7 (0.9) where the quoted signal-to-noise ratio refers to the mean per \AA near $0.52 \mu\text{m}$. (*Upper Right Panel*) Spectra for three simulated PNe in M49. The spectra have $m_{5007} = 27.0$ ($S/N = 69$), 27.6 (47) and 28.3 (11.5), where the signal-to-noise ratios refer to the central pixel of the $[\text{O III}]$ 5007 \AA line. (*Lower Left Panel*) Difference between input and measured radial velocity for simulated GCs in M49, plotted as a function of signal-to-noise ratio. The dashed lines show the minimum acceptable velocity error. (*Lower Right Panel*) Difference between input and measured radial velocity plotted against signal-to-noise for simulated PNe. The dashed lines show the maximum acceptable velocity error.

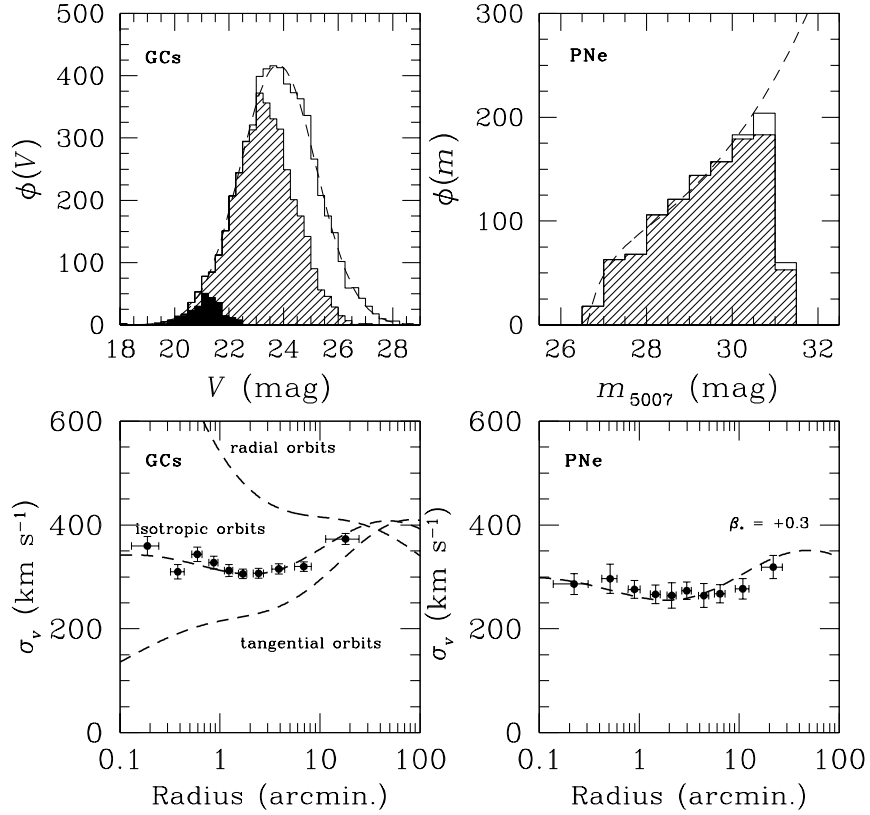


Figure 12: (*Upper Left Panel*) Input luminosity function of GCs belonging to M49 (dashed curve and open histogram). The hatched histogram shows the 4049 GCs for which a 1 hour exposure with MOBIE would yield $S/N \geq 1$. The luminosity function of the 263 GCs with existing velocity measurements from Keck is shown as the shaded histogram. (*Upper Right Panel*) Input luminosity function of PNe in M49 (dashed curve and open histogram). The hatched histogram shows the 1065 PNe for which a 1 hour exposure with MOBIE would yield $S/N \geq 1$. (*Lower Left Panel*) A simulated measurement of the anisotropy parameter, $\beta \equiv 1 - \sigma_\theta^2/\sigma_r^2$, for the globular cluster system of M49. Different anisotropy parameters are shown by the different curves, from strongly radial ($\beta = +0.99$, upper curve), to strongly tangential ($\beta = -0.99$) orbits. The measured velocity dispersion profile recovers the assumed isotropic velocity distribution with high confidence. (*Lower Right Panel*) Same as previous panel, except for PNe. In this case, the dashed curve shows the velocity dispersion profile for the assumed (input) case of mildly radial stellar orbits, $\beta_* = +0.3$.

3.5 Three-Dimensional Baryonic Structure During the Epoch of Galaxy Formation

3.5.1 Background

There have been two very significant developments in understanding the high redshift universe that have emerged in the last decade of 8-10m class telescopes. First, with the advent of high resolution spectrographs on these telescopes (most notably Keck/HIRES and VLT/UVES), quasar absorption line spectroscopy (coupled with increasingly sophisticated numerical simulations of structure formation) has revolutionized our view of the diffuse intergalactic medium. This technique uses distant, albeit luminous, QSOs as background beacons on whose continua the absorption profiles of intervening gas reservoirs are imprinted. The beauty of this approach is that galaxies and other gaseous structures in the IGM are detected independent of their luminosity. Moreover, the information accessible in the absorption line spectra is of extremely high quality, with many orders of magnitude more sensitivity than would be possible if the gas were required to be “self-luminous”. For example, the Ly α line provides such a sensitive probe of neutral hydrogen gas that densities much less than the cosmic mean can be easily detected at redshifts $1.8 \lesssim z \lesssim 3.5$. Through these kinds of studies, we have learned that diffuse gas in the intergalactic medium is a reliable tracer of the initial dark matter power spectrum on small scales that are not measurable using self-luminous objects (because sites of galaxy formation have become much too non-linear by the observable cosmic epochs). We have also learned that much of the intergalactic gas, if not all of it, has been enriched by an early generation of star formation in galaxies. It is estimated that at $z \sim 3$, $\sim 90\%$ of the baryons in the universe reside in the diffuse intergalactic medium; thus, the IGM acts as both a reservoir for fueling the galaxy formation process, and as a sink for receiving its products (e.g., metals, energy). The main limitation of the IGM studies is that QSOs bright enough to act as background beacons are very rare, and the information content along a single line of sight, while of extremely high quality, does not provide three-dimensional information and does not show directly how the absorption signatures relate to luminous objects inhabiting the same (or nearby) regions of space.

Meanwhile, great progress has been made in our ability to routinely study large numbers of galaxies at similar redshifts, thanks to sensitive multi-object optical spectrometers (e.g. Keck/LRIS, Gemini/GMOS, VLT/FORS) on current generation telescopes. Many of these galaxies have spectra that are quite similar to those of QSOs through the rest-frame far-UV, but they are generally much fainter than the QSOs that have been used for the absorption line spectroscopy discussed above (e.g., Shapley et al 2003). Samples of such galaxies have allowed us to understand how they are distributed in space, statistically, and have allowed the construction of their luminosity distributions in various observed wavebands. The statistical study of high redshift galaxies has been truly revolutionized in the last decade, and has given us a crude picture of the global star formation history of the universe, at least over the last $\sim 90\%$ of the age of the universe. The relevant cosmological model has been similarly revolutionized over the same period, to the point that many of the most significant unresolved questions in understanding how galaxies form relate to the physics of the baryons (and not the distribution of dark matter) and how the energy produced by star formation, supernova explosions, and AGN accretion affect the subsequent development of structure on galaxy scales. In short, there is a developing broad-brush picture of *when* galaxy formation is happening, and techniques exist for finding and collecting samples of most of the denizens of the high redshift universe, but we are lacking a detailed physical picture of *how* galaxies form. The answers to the questions related to “gastrophysics” require greater sensitivity and synthesis of techniques, such as we are suggesting below.

A simultaneous study of galaxies and the diffuse intergalactic medium, in the same volumes of space, offers the possibility of combining two powerful lines of investigation that provide complementary information on the state of baryons, both those collapsed into galaxies and those remaining in between the galaxies. The IGM represents a laboratory in which the effects of galaxy formation and AGN accretion (e.g., radiative and hydrodynamical “feedback” and its recent history) can be measured on scales that are not accessible using direct observations of galaxies, and, similarly, the galaxy distribution relative to the lines of sight to background objects tells us more about how the physical information garnered from the absorption line studies should be interpreted.

Here we outline a survey of the high redshift universe that combines absorption line studies with direct observations of galaxies and active galactic nuclei in the same cosmic volumes. Our current understanding of global star formation in galaxies, and also of the evolution of supermassive black hole accretion as inferred from AGN surveys, suggests that the redshift range $1.8 \lesssim z \lesssim 3.5$ includes the most active period in the universe’s history for both processes. It is also the range over which neutral hydrogen in the IGM can be observed with high dynamic range from the ground using both background QSOs and galaxies, as we discuss.

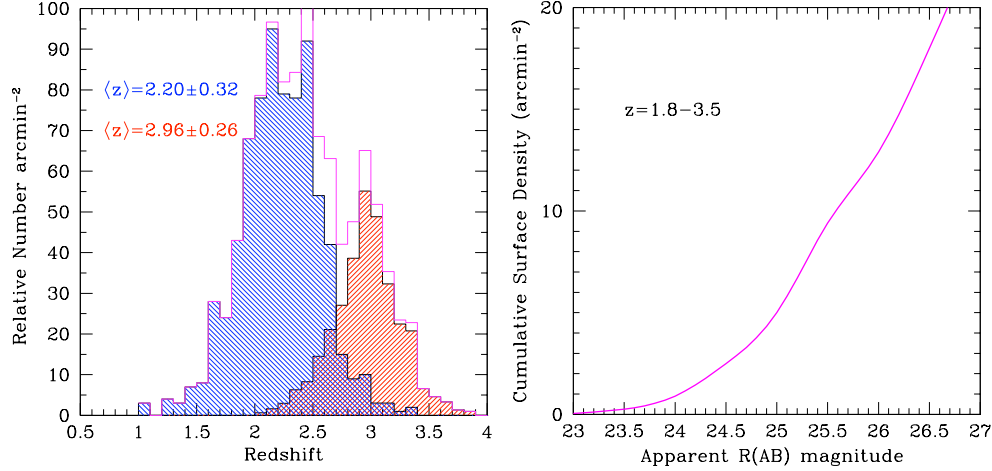


Figure 13: (Left) The relative surface density versus redshift for rest-UV selected galaxy samples to a fixed apparent magnitude limit (based on spectroscopic samples observed to $R(AB) = 25.5$). The relative distribution of objects to $R(AB) = 26.5$ is expected to be similar. The magenta histogram is the sum of the two sub-samples. (Right) The cumulative surface density of galaxies in the targeted redshift range $1.8 \lesssim z \lesssim 3.5$ as a function of apparent magnitude, based on measured rest-frame far-UV luminosity functions obtained from existing large spectroscopic samples (Steidel et al 1999; Reddy et al 2008).

The limitation on the sampling density of sightlines for absorption line studies is overcome through TMT’s large collecting area, the high spectral throughput of MOBIE, and the novel use of background *galaxies* to study HI and metals in the IGM. The surface density on the sky of QSOs of course increases with decreasing brightness, reaching $\sim 100 - 200$ per square degree ($\sim 0.03 \text{ arcmin}^{-2}$). However, as shown in Figure 13, the surface density of UV-bright galaxies is $\sim 100 - 200$ times higher by $R_{AB} \sim 24.5$ (approximately the magnitude at which MOBIE can obtain spectral resolution $\mathcal{R} \sim 5000$ and $S/N \geq 30$ per resolution element.) The observed surface density of UV-bright galaxies to that limit ($2\text{--}3 \text{ arcmin}^{-2}$) translates to a transverse spatial sampling of a few hundred physical kpc (with the currently accepted cosmology). Observing the entire grid of suitably-bright background sources (QSOs and galaxies) thus provides for the first time the possibility of the 3-D “tomographic” reconstruction of the IGM, at a spectral resolution that is adequate to resolve the typical thermal width of intergalactic HI clouds and to discern even relatively weak lines of metallic species whose wavelengths appear longward of Lyman α emission in each probe’s rest frame. The galaxy spectra thus obtained will also allow unprecedentedly detailed spectra of the galaxies, containing information on the chemistry, kinematics, and stellar populations which are currently possible only for rare strongly-gravitationally lensed objects (see, e.g., Pettini et al 2002, and § 3.6).

3.5.2 Specific science goals

Our goal is to execute a TMT+MOBIE program to survey the IGM–galaxy system over a region of the $1.8 < z < 3.5$ universe that is of the same order as that surveyed by the Sloan Digital Sky Survey (SDSS) at $z \sim 0.1$. The SDSS field of view (2.5 degrees in diameter) equates to a transverse scale of $\sim 18 \text{ Mpc}$ at that survey’s median redshift; the same co-moving scale at $z \sim 2.75$ subtends only 10 arcmin, the size of the MOBIE field of view. By the same token, MOBIE could survey the 10^8 Mpc^3 achieved by the SDSS in a solid angle of only ~ 4 square degrees. Here we are proposing to survey a co-moving volume of $\sim 5 \times 10^7 \text{ Mpc}^3$, which would require surveying a total of area of 2 deg^2 . This would most sensibly be done in at least 4 separate survey fields of $\sim 0.5 \text{ deg}^2$ each, well separated in RA but at declinations allowing for long integrations on a given night (i.e., depending on the latitude of the observatory).

The MOBIE galaxy/IGM tomography project consists of two components. The first component is to obtain high S/N ($\gtrsim 25$ per spectral resolution element), $\mathcal{R} \sim 5000$ spectra of objects (QSOs, AGN, and galaxies) with $R < 24.5$. Over the 2 square degree survey area, we expect $\sim 20,000$ such objects which will be used as background sources to trace intervening absorption and as high quality spectra for the evaluation of detailed galaxy properties. We can efficiently sample $\sim 50\%$ of these, as discussed below. We will also obtain lower resolution ($\mathcal{R} \sim 1000$) spectra of

fainter galaxies ($24.5 < R < 26.5$), of which there will be a total of $\sim 10^5$ in the redshift range of interest, of which we would hope to observe $\sim 60\%$ (see below). The survey would simultaneously yield a very detailed map of large scale structure traced by galaxies, as well as the quasi-3D distribution of neutral hydrogen and metals in the diffuse IGM—observations which are impossible at lower redshift and with smaller telescopes. It will allow the measurement of the radiative and hydrodynamic influence of QSOs, AGN, and galaxies on their environments, addressing some of the most crucial remaining questions in understanding galaxy formation, AGN activity, and the nature of the intergalactic medium.

3.5.3 Planning of observations

A key to planning the details of the observations is a good statistical knowledge of the density of targets for each of the two components of the survey. From work completed using 8-10m class telescopes, coupled with very deep imaging surveys, it is well known that simple broad band selection criteria can be used to select star-forming galaxies and AGN in prescribed ranges of redshift, typically with a breadth of the redshift selection function of $\sigma(z) \simeq 0.3 - 0.4$ (e.g., Steidel et al. 2004). Figure 13 shows that, with a combination of two such color-selected galaxy samples, a well-defined range of redshifts matching the cosmic volume targeted in the survey can be assembled, and it allows us to examine issues related to assignment of objects to slit masks and the achievable observing efficiency.

For this science demonstration, we have chosen the field around the QSO HS1700+64 for which wide-field, multi-band photometry already exists, and where significant spectroscopy of the brighter high redshift galaxy candidates satisfying the same photometric selection criteria as the samples in Figure 13 has already been obtained. A single MOBIE footprint of 4.2 by 9.6 is indicated in Figure 14, superposed on an R -band image of the field which reaches the desired $R = 26.5$ depth (the catalogs of galaxy candidates at the faintest magnitudes are incomplete due primarily to the depth in the other two passbands needed to isolate the samples; in practice the required depth is easily achieved even with 4m-class telescopes with long integration times). As can be seen in Figure 13, the surface density of galaxies in the redshift range of interest has reached $\sim 15 \text{ arcmin}^{-2}$ by $R(AB) = 26.5$, so that a typical MOBIE footprint will contain several hundred candidates for the faint survey and $\sim 70 - 80$ candidates for the $\mathcal{R} = 5000$ survey. The outcome of the mask design in the particular footprint shown in Figure 14 is discussed further below.

It is important to note that target selection based on broad-band colors is rather trivial, and is quite clean in the sense that few objects will lie outside the targeted redshift range(s). It is therefore not essential for any spectroscopy to have been done in the survey fields prior the TMT+MOBIE spectroscopic program. However, it may improve the efficiency of mask design either to observe all of the bright candidates first using the $\mathcal{R} = 1000$ configuration described below, or to have measured precise redshifts for the bright sub-sample using 8m class telescopes. Based on experience with long integrations on a 10m telescope, it is not unreasonable to expect 100% spectroscopic completeness for observed galaxies in the suggested integration times (see Figure 16).

The nominal resolution required for high quality tomography of the IGM is $\mathcal{R} = 5000$ (see Figure 15 for the impact of this resolution choice). In round numbers, this is the minimum required to resolve typical Lyman α forest H I lines having Doppler parameters $b \sim 30 \text{ km s}^{-1}$, or $\text{FWHM} \sim 50 \text{ km s}^{-1}$, and is also approximately the minimum resolution required for the detection of relatively weak absorption lines of metallic species, most notably CIV $\lambda\lambda 1548, 1550$. There is of course a trade-off between spectral coverage in a single observation and the achieved spectral resolution, and indeed interesting characteristics of the IGM can be obtained even with resolution as low as $\mathcal{R} \sim 1000$ (so that even the fainter object portion of the program will yield quantitative results on the IGM on still smaller spatial scales than afforded by the higher quality $\mathcal{R} = 5000$ spectra of the brighter sub-sample).

For the higher resolution configuration, the key wavelength range runs from Ly β (1025.7 Å) and O VI $\lambda\lambda 1032, 1037$ to C IV $\lambda\lambda 1548, 1550$ at the emission redshift of the object. The latter two doublets are the strongest lines observed in the relatively low-density IGM, while the region between Ly α and Ly β at the emission redshift of the object provides the most reliable information on the HI optical depth over a redshift range $\Delta z \simeq 0.5$. Table 3.5.3 summarizes the observed wavelengths of some key transitions as a function of redshift, over the targeted redshift range.

If the redshifts of the bright sources are known *a priori*, as may be the case if they have been observed first at $\mathcal{R} = 1000$ or previously with 8-10m class telescopes, one could add a level of complexity to the mask design software (not yet implemented) that would group objects at similar redshifts on the same mask, which might allow higher multiplexing by requiring fewer spectral orders to cover the most important spectral features.

Table 5: Wavelengths of Key Spectral Features vs. Redshift

Redshift	Ly limit (912 Å)	Ly β (1026 Å)	O VI (1032,1037 Å)	Ly α (1216 Å)	C IV (1548,1550 Å)	He II (1640 Å)
2.00	...	3078	3102	3647	4649	4920
2.25	...	3333	3360	3950	5036	5330
2.50	3191	3590	3619	4255	5420	5740
2.75	3419	3846	3878	4559	5810	6150
3.00	3647	4102	4136	4863	6198	6560
3.25	3875	4359	4395	5167	6585	6970
3.50	4103	4615	4653	5470	6973	7380

The wavelength regions outside of these regions are also extremely useful in addressing a number of scientific questions; for example, data obtained at wavelengths shortward of 3650 Å for objects with $z_{em} \simeq 3$ will be able to directly measure the leakage of Lyman continuum radiation from the galaxy (i.e., it would measure the flux of photons with $\lambda_0 < 912$ Å), an extremely challenging observation at present but one which should be quite routine with TMT+MOBIE. Such observations could be used to evaluate the importance of local sources of UV ionizing photons on the physical state of the nearby IGM, one of the many benefits of the simultaneous observation of the IGM and sources of ionizing photons.

We have chosen $\mathcal{R} = 1000$ as the optimal resolution for the faint galaxy portion of the survey for two reasons: (1) the typical intrinsic width of features in the spectra of faint galaxies are $\text{FWHM} \sim 300 - 600 \text{ km s}^{-1}$ (these tend to be interstellar absorption lines widened by the kinematics of outflowing material in galactic superwinds, with weaker lines being narrower) and matching the spectral resolution to the expected line widths provides maximum contrast for features essential to redshift identification; and (2) the resolution is just high enough to resolve the CIV doublet so that at least strong intervening absorption line systems can be identified in many of the galaxy spectra; it is also just high enough that the level of absorption in the Lyman α forest reasonably accurately reflects the mean HI opacity in the corresponding segment of the IGM (see, e.g., Adelberger 2004). There is always a temptation to place multiple tiers of slits in the focal plane and avoid overlap of spectra by using lower dispersion, which works well in the limit of very high object surface density on the sky. Our experiment below suggests that, even with surface densities of $\gtrsim 10 \text{ arcmin}^{-2}$, the multiplexing gain would be considerably smaller than a factor of two for two ranks of slits, and the loss of spectral resolution would have a significant scientific cost (not to mention issues related to scattered light, order blocking, etc.).

For the $\mathcal{R} = 1000$ configuration, it will be possible to cover ~ 1 octave in wavelength with a given spectrometer channel (and thus the entire range 3100-5500 Å on the blue side, and 5500-10000 Å on the red side) for a slit placed anywhere in the MOBIE field). Based on experience, the blue channel wavelength coverage would be more than adequate for redshift identifications for all targeted objects. Information collected on the red side would be very useful for spectral diagnostics (e.g., the C IV and He II emission lines, when present, together with Ly α and N V $\lambda 1240$, are excellent indicators of low-level AGN activity when it is present) but not essential for redshift measurements, and a host of low-ionization interstellar features (as well as stellar photospheric lines) at rest-frame wavelengths of 1800-3000 Å are also quite useful.

3.5.4 Pre-imaging

It is likely that the proposed survey will be conducted in fields that have been imaged to more than adequate depths using current-generation telescopes (e.g., the CFHT Legacy (Deep) Survey fields will have very deep images in passbands allowing very clean photometric pre-selection similar to that described above). It should be possible to use astrometry from these external images to design masks to be used for MOBIE; in other words, it is expected that the TMT focal plane (behind the MOBIE ADC) will be stable and will be mapped out well enough that no images using MOBIE need be taken in order to design slit masks. Although MOBIE will be quite capable as an imager, it is an unnecessary waste of telescope time to obtain “pre-images” in general, unless the imaging cannot be obtained on smaller telescopes (not the case here).

3.5.5 Mask design

In this demonstration, we show example mask designs for one pointing of MOBIE centered on the field shown in Figure 14. The software used for the demonstration is a modified version of “autoslit”, the facility mask design software for the LRIS instrument at the W.M. Keck Observatory. The software is designed to select objects based on their assigned numerical priority, which in this case were all set initially to be equal. For the “faint” masks, slits were allowed to be as short as 4 arcsec (note that this is the minimum space allocated per object even if nod/shuffle techniques are implemented) and to be placed within a rectangular field of dimensions 4.2 by 9.6. For the “bright” masks, we have conservatively assumed that we require complete wavelength coverage at $\mathcal{R} = 5000$, so that each object needs a minimum of 20 arcsec of slit length in order to accommodate 5 spectral orders using a slit height of 3 arcsec. The procedure for both “faint” and “bright” masks was to significantly downgrade the priority of objects already assigned to previous masks before designing the next one, so that an object was repeated only when there was no other object available near the same mask Y position.

The particular pointing shown in Figure 14 has a total of 106 $z = 1.8 - 3.5$ candidates to $R(AB) = 24.5$ and 392 candidates with $24.5 < R(AB) \leq 26.5$. (In fact, 48 of the 106 bright candidates in this patch of sky have spectroscopic redshifts already measured to be in the range $1.8 < z < 3.5$.) These numbers correspond to a surface density within the footprint of $\simeq 2.6$ and $\simeq 9.7$ arcmin $^{-2}$ for the “bright” and “faint” subsamples, respectively.

A total of 6 masks was designed, fixing the location of the footprint and not allowing it to move freely to optimize a given mask. The actual objects assigned to masks are shown in Figure 14. The statistics of these masks are summarized in Table 6. There are several issues to note: first, the number of unique slits assigned is a decreasing function of mask number for a fixed pointing, particularly for the lower-surface-density bright sample. Even for objects with a very high surface density such as those targeted in the faint “F” masks, the number of unique objects assigned slits decreases steadily long before the list of potential targets is near exhaustion; after 3 successive mask iterations, one has still covered only about 60% of the possible targets within the footprint. Another noteworthy fact: even though slits were allowed to become as short as 4 arcsec, even the first mask targeting faint objects could assign slits to only $\simeq 60\%$ of the possible number (i.e., the total slit length of 576 arcsec divided by 4 arcsec is 144, not 87). This is the case in spite of the fact that each 4.2 arcmin by 4 arcsec swath of the field contains an *average* of ~ 3 potential faint targets.

Table 6: Mask design statistics, single MOBIE pointing with fixed footprint

Mask name	#Unassigned objects	#Slits assigned	#Repeats	#Unique
B1	106	19	0	19
B2	87	16	1	15
B3	72	18	3	15
Total				49/106
F1	392	87	0	87
F2	305	86	3	83
F3	222	78	13	65
Total				235/392

The efficiency of assigning unique objects to slits increases if the MOBIE footprint is allowed small dithers in X, Y, or mask position angle. One would almost certainly optimize the mask design scheme to carry out any large survey project.

Conservatively, each MOBIE “faint” mask would include ~ 90 objects (each mask requiring $\simeq 1$ hour of integration), and each “bright” mask would include $\simeq 20$ targets [up to double that number if masks are optimized for particular (smaller) redshift ranges]. Simulations of the expected performance of TMT+MOBIE for the $\mathcal{R} \simeq 5000$ ECH mode are shown in Figure 15; Figure 16 shows simulations of spectra such as would be obtained for typical objects on the “faint” masks.

3.5.6 Procedures during the day

The afternoon before the observations, the masks for the coming night should be loaded into the mask storage magazine and mask images obtained with the flat field lamps turned on (no dispersing element). This procedure allows a map to be made of the slit positions so that alignment can be done on each field. This calibration should take no more than 2 minutes per mask. Since a night dedicated to the “faint” part of the survey could use up to 10 different slitmasks, the minimum number that must be accommodated in the mask delivery system would be 10.

Dispersed flat field images for each mask should also be obtained in the afternoon, if possible. Ideally, there would be a region of the inside of the dome somewhat larger than the telescope primary that could be illuminated with featureless continuum lamps producing light over the full wavelength range of MOBIE. There should also be the fall-back option of flat fields obtained with a quartz lamp internal to the instrument, though careful control of the pupil to mimic illumination through the telescope at $f/15$ may be difficult. The best flat fielding will be obtained using illumination from the twilight sky, with a diffuser placed in the beam to smooth out sharp spectral features. This capability would imply a start to observing immediately after sunset, and ideally flats for each mask to be used would be obtained near the predicted elevation and rotator position of the night-time observation (see § 4).

3.5.7 Procedures during twilight

No special procedures beyond those given in §4.

3.5.8 Target acquisition

Each mask will have at least 4-5 alignment apertures (normally boxes, rather than slits) which can be used for fine alignment by being assigned to stars in the field. Generally stars that are of comparable brightness to the sky background are adequate. Mask alignment with MOBIE should not require a direct image of the field without the mask in place; instead, the guider/WFS position of a known star will be an output of the mask design process. When this guide star is placed at the specified guider position with the instrument rotator set to the nominal mask PA, a short direct image ($\sim 10 - 30$ seconds) through the mask would then provide enough information for the instrument software to solve for any small adjustment in PA and telescope offset. Any rogue reference stars can be rejected interactively by the user through the interface to the alignment software. It should be possible for the entire acquisition to take less than 3 minutes from the completion of telescope slew to the start of a science integration⁸.

3.5.9 Target science data acquisition

Our assumptions for the simulated spectra shown in Figures 15 and 16 are that the spectra are taken under dark conditions, with $0''.8$ seeing, $0''.7$ slits and at airmass $\sec z = 1.0$. The resolution is $\mathcal{R} = 5000$ for the primary set-up and $\mathcal{R} = 1000$ for secondary masks.

Covering 2 deg^2 with MOBIE would require ~ 180 independent MOBIE pointings. Assuming that 2 passes per MOBIE footprint are made with each configuration, a total of 360 hours ($\simeq 40$ nights) would be required for the faint galaxy portion of the survey, while the bright portion would require $\simeq 1080$ hours (~ 120 nights). The survey would then yield $\simeq 32,000$ “faint” spectra, and $\simeq 7,000$ “bright” ones, assuming full wavelength coverage for both configurations. While these would be large investments of observing time with TMT, the survey volume is comparable to any spectroscopic survey obtained to date (at any redshift), and includes information far beyond mere “galaxy mapping”, and unique with respect to any lower-redshift survey.

3.5.10 Calibration data acquisition

No special calibration steps beyond those listed in §4.

3.5.11 Additional requirements

The magazine which houses the masks should be able to store at least 10 pre-cut masks ready for use on a given night.

⁸A similar scheme is used for field acquisition of the DEIMOS instrument on the Keck II telescope.

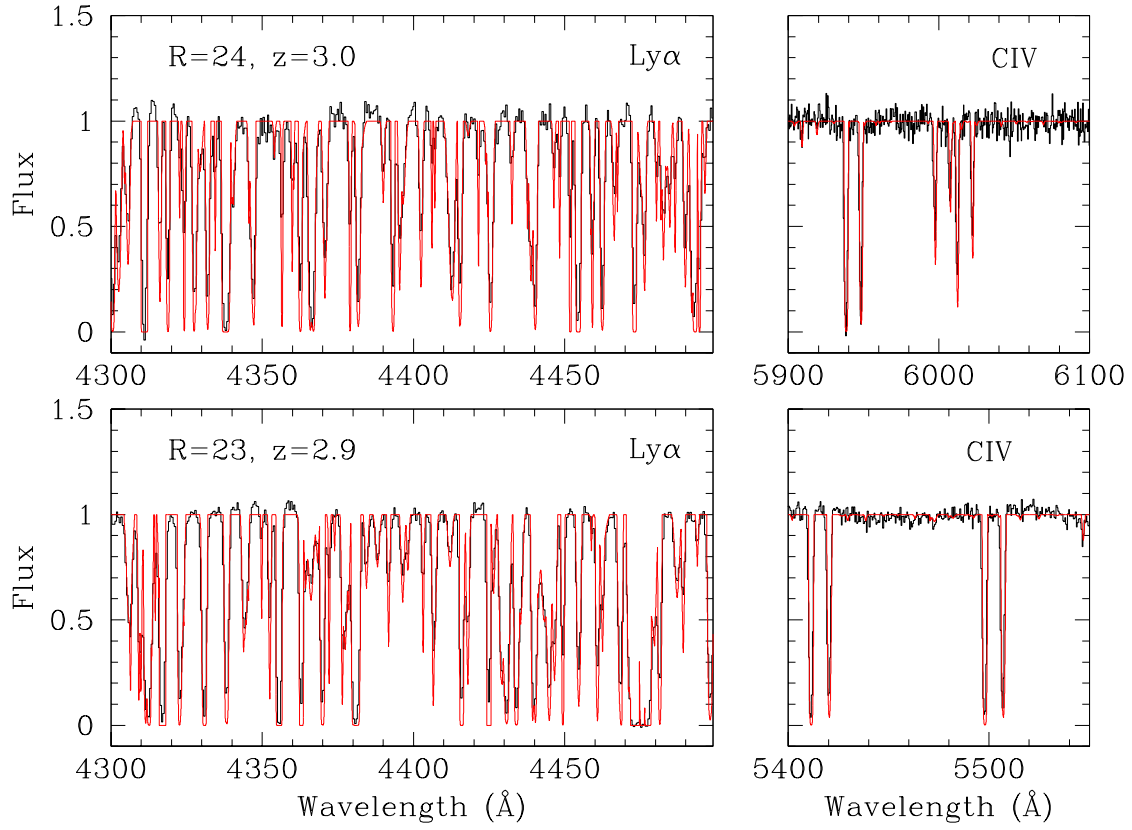


Figure 15: Example sections of simulated spectra for $R(AB) = 23, 24$ $\mathcal{R} = 5000$ configuration. The assumed total integration times were 3 hours. The $\mathcal{R} = 5000$ spectra are black, while the spectra before convolution with the instrumental resolution are shown in red.

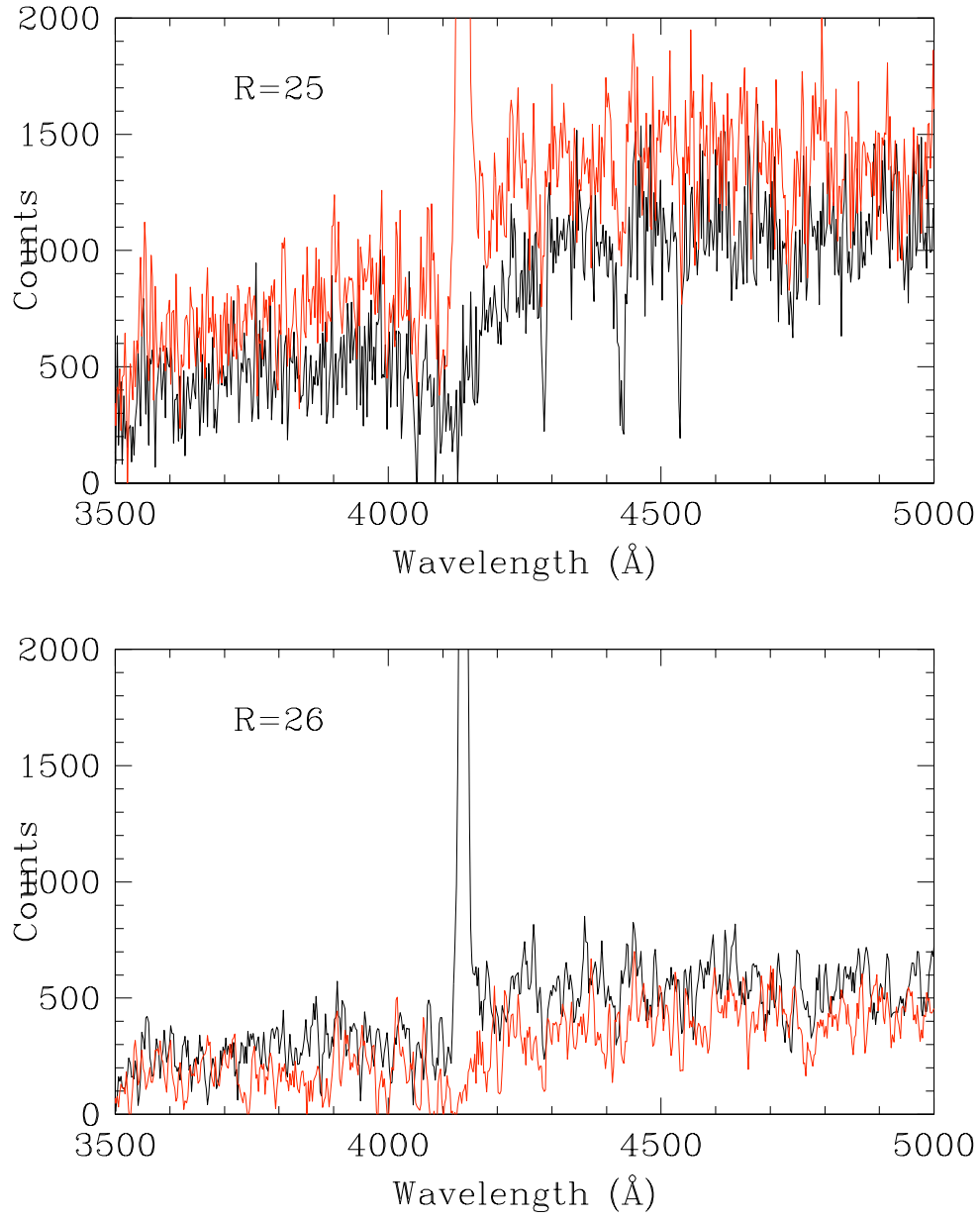


Figure 16: Simulated spectra for $z = 2.4$ galaxies at $R(AB) = 25$ and $R(AB) = 26$, assuming 1 hour total integration time with the blue $\mathcal{R} = 1000$ configuration. The spectra are derived from the composite Lyman break galaxy spectra (Shapley et al. 2003) for the lowest (red) and highest (black) quartiles in Lyman α emission strength. The $R = 26$ spectra will easily yield redshifts even for objects without emission lines. Note that the $R = 26$ spectra have been smoothed with a boxcar filter with a 3 pixel width.

3.6 The Stellar and Gaseous Content of L^* Galaxies at $z \sim 2 - 5$

Over the past several years, statistical samples of star-forming galaxies have been assembled at $z > 2$ (Steidel et al. 2003; Steidel et al. 2004; Daddi et al. 2004; Bouwens et al. 2007). We have learned much about high-redshift star-forming galaxies, in terms of their luminosity function, spatial clustering, stellar masses, dust content, and star-formation rates (Adelberger & Steidel 2000; Bouwens et al. 2007; Adelberger et al. 2005; Papovich et al. 2001; Erb et al. 2006; Reddy et al. 2006). However, the faint magnitudes ($\mathcal{R}_{AB} \geq 24.0$ mag) and small angular sizes ($\leq 1''$) of typical star-forming galaxies at $z > 2$ limit the degree of detail that can be learned about individual objects.

Currently, this limitation can be overcome in the presence of magnification due to strong gravitational lensing. MS1512-cB58 is a typical $\sim L^*$ LBG at $z = 2.73$ which has been magnified by a factor of ~ 30 due to the presence of a foreground cluster at $z = 0.37$ (Seitz et al. 1998). Within the last two years, several additional strongly-lensed star-forming galaxies at $z > 2$ have been identified, both within the Sloan Digital Sky Survey (SDSS) (Allam et al. 2006; Belokurov et al. 2007), and in surveys of the central regions of massive clusters (Smail et al. 2007). In particular, these lensed objects have R-band magnitudes of $19 - 21$ (AB) enabling high resolution and signal-to-noise optical spectroscopy probing the rest-frame UV, using both Keck/LRIS and ESI. These spectroscopic observations have provided truly unique windows into the stellar population and interstellar medium of intrinsically $\sim L^*$ LBGs at $z > 2$. The problem is that only a limited number of such highly magnified systems have been identified and spectroscopically confirmed within the entire SDSS photometric database ($N < 10$ so far). With such a small sample, it is not possible to span a broad range of galaxy spectral parameter space in a systematic, statistical fashion. On the other hand, with the $R = 5000$ multiplexed echellette capability of MOBIE, including full spectral coverage from $\sim 3300\text{\AA} - 1.0\mu\text{m}$, it will be possible to obtain comparable quality spectra ($S/N > 15$ per resolution element) for a sample of $N = 100$ objects at $z > 2$, with $R_{AB} \lesssim 24$.

3.6.1 Specific Science Goals

There are several areas in which a statistical sample of such spectra will lend key insights into the nature of high-redshift star-forming galaxies during the build up of their stellar populations. These include:

- Absorption-line probes of the metal content and abundance pattern of the cool phase of the interstellar medium, and indications of the metallicities of massive stars based on both photospheric and wind features (see Figures 3.6.1 and 3.6.1). In principle, metallicities offer an essential probe of the integrated products of previous star formation, modulated by inflows and outflows of gas. Comparison of observed and simulated galaxy scaling relations between metallicity and mass may offer important insight into the process of star-formation feedback. Currently, however, the metal content of high-redshift most star-forming galaxies is probed with the use of empirically-calibrated nebular emission-line indicators, which are fraught with systematic uncertainties. It is therefore critical to obtain metallicities using independent methods, probing both the metal content of gas and stars.
- Constraints on the stellar population and initial mass function based on the profiles and equivalent widths of P-Cygni (C IV) and pure emission (He II) wind lines from main-sequence and evolved (W-R) massive stars (Pettini et al. 2000; Leitherer et al. 2001; Brinchmann et al. 2008). There is much attention currently being placed on the form of the IMF both at low- and high- masses, in terms of understanding the metal enrichment history of the universe (Nagashima et al. 2005), as well as the relationship between the evolution of the global star-formation and stellar-mass densities (Dave 2007). These rest-frame UV measurements will offer an independent and crucial constraint on the high-mass end of the stellar IMF.
- Detailed kinematic probes of galaxy-scale outflow signatures of the feedback process (see Figure 3.6.1) based on the velocity profiles of interstellar metal absorption lines tracing both neutral and ionized gas, and, in particular, the $\text{Ly}\alpha$ profile from H I. The kinematics of these interstellar features offer some of the strongest evidence in favor of ubiquitous large-scale outflows from star-forming galaxies at high redshift, and must be studied at moderately high spectral resolution in order to discern the physical properties of the absorbing gas (Pettini et al. 2002). Indeed, a statistical sample of $\text{Ly}\alpha$ profiles (both emission and absorption) with $\mathcal{R} = 5000$ will place important constraints on the distribution in physical and velocity space of neutral gas in these star-forming

galaxies (Verhamme et al. 2006), and aid in the interpretation of very high redshift Ly α emitters used to probe the galaxy population at and before the epoch of re-ionization.

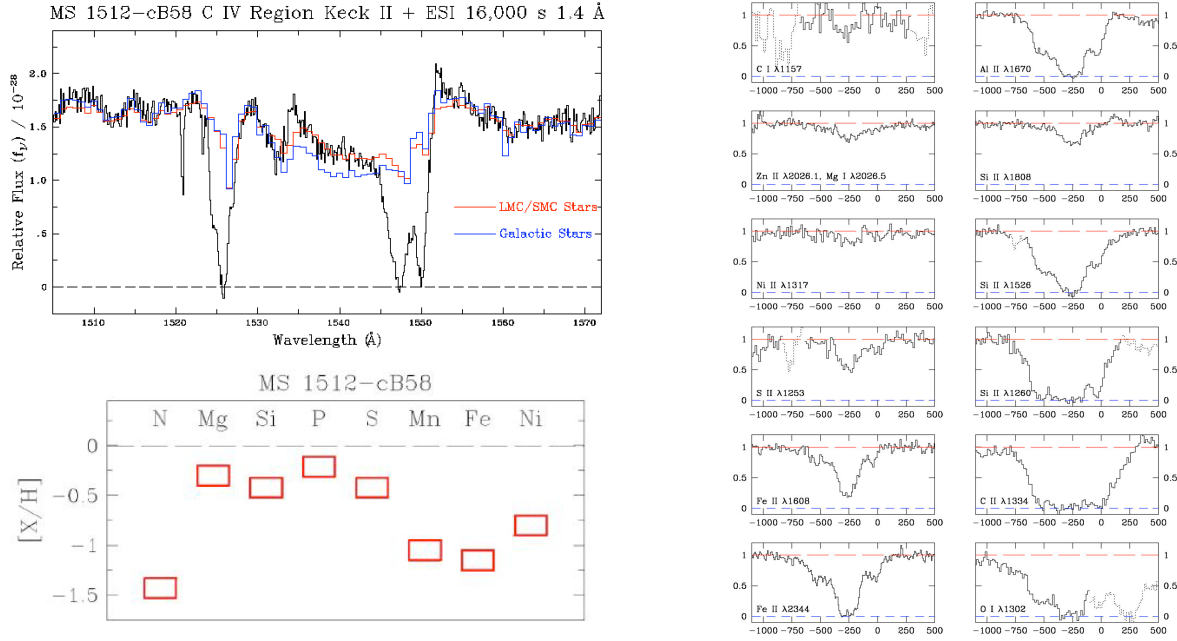


Figure 17: High-resolution ($\mathcal{R} \simeq 5000$) spectroscopy of MS1512-cB58. **(Left, top)** The CIV (1549 Å) P-Cygni profile in the ESI spectrum of cB58. The black line indicates the observed spectrum, while the red and blue lines indicate Starburst99 constant star-formation model fits to the P-Cygni profile using LMC/SMC and solar metallicity stars, respectively. The large absorption doublet within the P-Cygni profile is from interstellar CIV. The P-Cygni profile rules out instantaneous burst models for the star-formation history, as well as favoring a Salpeter IMF at the high-mass extreme (Pettini et al 2000). **(Left, bottom)** The interstellar abundance pattern in cB58. This pattern reveals the enhancement of alpha elements (Mg, Si, P, S) relative to both Fe-peak elements (Mn, Fe, Ni) and nitrogen, indicative of preferential enrichment by Type II supernovae in a young stellar population (from Pettini et al. 2002). **(Right)** Velocity profiles of low-ionization interstellar absorption lines tracing predominantly neutral H I gas. Velocities are plotted relative to the stellar systemic redshift. Outflowing neutral gas extends to velocities of -750 km s^{-1} , indicating that it will most likely escape from the potential well of cB58 (Pettini et al. 2002).

3.6.2 Planning of Observations

3.6.3 Target Selection

Samples of spectroscopically-confirmed UV-selected (i.e. objects with rest-frame UV fluxes brighter than $R_{AB} = 24.0$) galaxies will be the primary targets. The surface density of such objects is $\sim 1 - 2$ per square arc minute integrated between $z \sim 2 - 5$, where the number counts are dominated by the low-redshift end of the range (Steidel et al. 1999, 2004; Bouwens et al. 2007).

3.6.4 Spectral resolution

The goal will be roughly match the ESI spectral resolution for observations of lensed high-redshift objects, i.e. $\mathcal{R} \simeq 5000$ (Pettini et al. 2002). This resolution is required for several purposes. While the strong interstellar metal absorption lines seen in high-redshift galaxies are quite broad ($v_{FWHM} \sim$ several hundred km s^{-1}), they must be highly resolved in order to characterize the full range in velocity space over which gas is absorbing, and the complex velocity structure of the outflowing material. Furthermore, for robust detection and characterization, it is optimal to place multiple resolution elements on weak stellar photospheric features, which typically have $v_{FWHM} \sim 150 - 200 \text{ km s}^{-1}$.

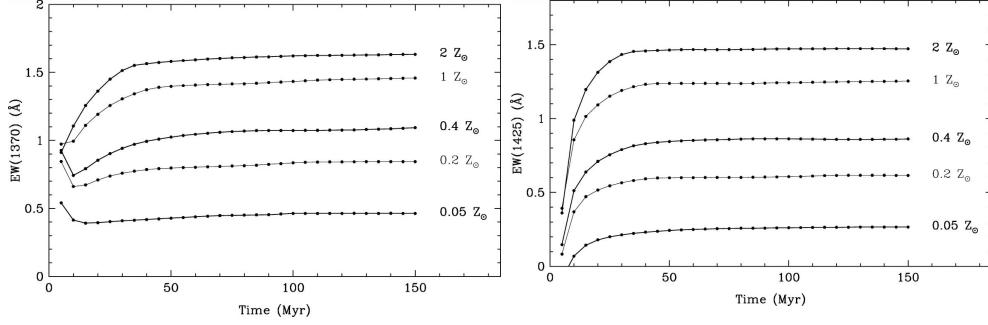


Figure 18: (From Rix et al. 2004) **(Left)** Variation of the 1370 Å stellar (photospheric) chemical abundance index with time and metallicity. **(Right)** Same, but for the 1425 Å index.

Finally, features such as C IV are characterized by complex structure, including both interstellar and stellar wind components. The isolation and robust measurement of these separate components requires the resolution provided by the echellette mode of MOBIE.

3.6.5 Wavelength coverage

The minimum requirement will be to cover features at rest-frame 1216-1640 Å, from $z \sim 2 - 5$. This rest-frame range includes: Ly α , strong low-ionization interstellar absorption lines from Si II, O I, and C II; high-ionization interstellar absorption lines from Si IV and C IV; stellar wind lines from C IV and He II; and multiple stellar photospheric indices between 1300 and 1500 Å. The above minimum requirement translates into an observed wavelength range of 3600 Å to 1 μ m.

3.6.6 Required integration time

In order to detect weak stellar photospheric indices, the most challenging goal outlined above, $S/N > 15$ per resolution element is required. Using a preliminary ETC for MOBIE (v 1.2; courtesy J. Prochaska), we estimate that such S/N can be achieved over the bulk of the desired wavelength range for $R_{AB} = 24.0$ with 8 hour exposure times, within a few days of new moon. With the assumption of a multiplexing factor of 10-15 objects per mask, the sample goal of $N = 100$ would be achieved by observing 8 masks, requiring $\simeq 8$ nights.

3.6.7 Mask design

In a given MOBIE field there will be ~ 50 suitable $R_{AB} \leq 24$ star-forming galaxies at $z \sim 2 - 5$. Since the desired wavelength range is large, the full echellette mode is desired. In this mode of the instrument, slits can be placed on 10 – 15 targets simultaneously. While the details of slit assignment have yet to be worked out, the surface density of suitable targets ensures the masks can be filled. If filler targets are required to fill masks, the optical magnitude limit will be relaxed. Many of the science goals outlined above can be achieved at slightly lower S/N .

3.7 QSO Pairs: Revealing AGN and Massive Galaxy Formation at $z > 2$

3.7.1 Scientific Justification and Background

Several lines of observational and theoretical evidence indicate that the antecedents of modern massive galaxies were formed during the first few Gyr of the universe. The evidence includes inferred properties of the sub-mm and distant-red galaxy (DRG) populations, the prevalence of bright quasars at $z > 5$, and the estimated old ages of the stars in present-day galaxies. Recent numerical simulations predict that high-redshift massive galaxies form primarily through the accretion of ‘cold’ gas traveling at sub-sonic speeds in filamentary structures (e.g. Dekel et al. 2008, arXiv:0808.0553). Aside from the somewhat circumspect approach of comparing integrated mass accretion rates with observed properties of galaxy stellar populations, there are few observational tests of this fundamental picture of galaxy formation. The fundamental, open questions that stand today include: Does the majority of gas shock to the virial temperature of the dark matter halo? Does cold gas condense out of this hot medium or does it primarily reside in filamentary structures? Is feedback from AGN activity or star-formation an essential ingredient to massive galaxy formation?

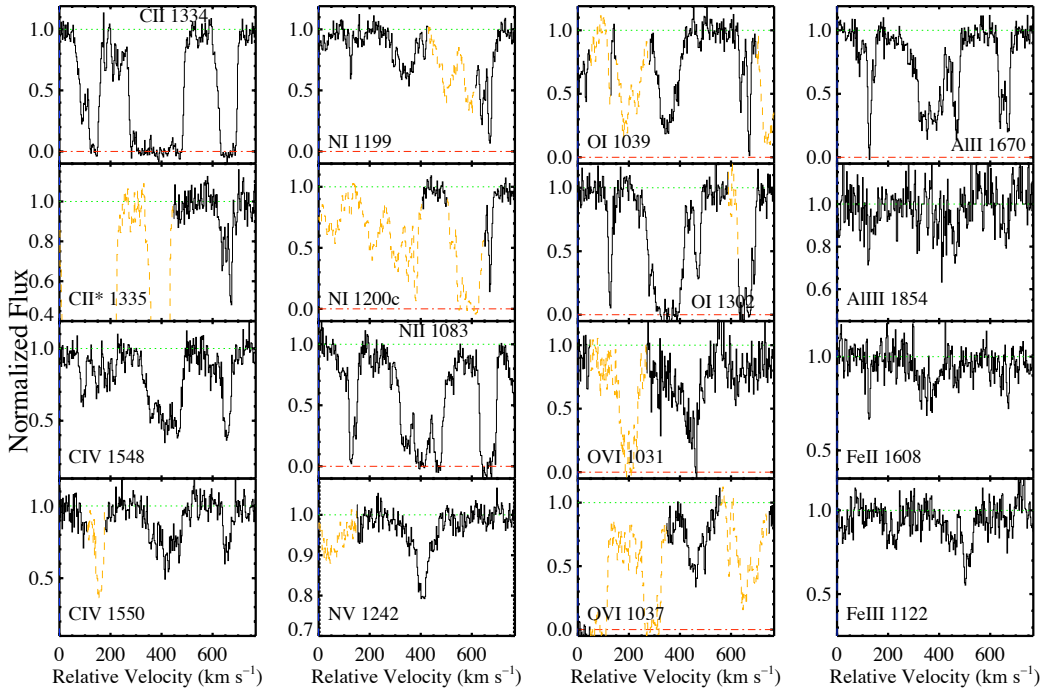


Figure 19: A subset of the metal-line transitions (Keck/HIRES) from an optically thick absorber (Lyman limit system) which lies at the identical redshift and at impact parameter $\rho = 100$ kpc from a $z \approx 2.5$ quasar (Prochaska & Hennawi 2008). These data establish the kinematics, metallicity, ionization state, volume density, relative abundances, and temperature of this gas which very likely lies within the dark matter halo hosting this quasar. Because quasars trace massive galaxies at $z > 2$ (an assertion established by their large clustering correlation length; Porciani et al. 2004), these observations trace gas processes at tens to several hundred kpc and also constrain characteristics of the ionizing radiation and feedback from high z AGN. Data presented as orange dotted lines indicate coincident blends with absorption lines from the $\text{Ly}\alpha$ forest and is to be ignored.

One approach to test scenarios of massive galaxy formation is through spectroscopy of close-projected quasar pairs (Hennawi et al. 2006). The foreground quasar serves as a marker of a probable massive dark matter halo; quasar clustering measurements suggest these are hosted by dark matter halos with $M \sim 10^{12.5} M_{\odot}$. A spectrum of the background quasar reveals the properties of the gas within and nearby this dark matter halo, e.g. Figure 19. With a large sample ($N > 100$) of quasar pairs, one can statistically reveal the surface density of cold gas, its metallicity, velocity field, and ionization state as a function of impact parameter, quasar magnitude, etc. In addition to tracing the

processes of cold gas accretion, one assesses quasar feedback, the distribution of warm gas, and the nature of the AGN activity (e.g. quasar lifetime, beaming).

Presently, J. Hennawi and collaborators have used the SDSS to uncover a sample of over 100 quasar pairs at $z > 2$. This includes a sample of ≈ 50 with impact parameters of less than 200 kpc. Unfortunately, most of these have background quasars with $g > 21$ mag which precludes high-resolution, high S/N observations with 10m-class telescopes. With the echellette mode of MOBIE, observations like those presented in Figure 19 would be easily achieved and one could build a statistical sample $N > 100$ in a modest observing campaign.

3.7.2 Key observable: Absorption-line spectroscopy of metal-line transitions

To probe the physical conditions of the gas in the halos surrounding quasars (i.e. massive galaxies), one requires high S/N, high-resolution observations of UV transitions with rest-frame wavelengths spanning $\lambda_{rest} = 1000 - 3000\text{\AA}$. At $z = 2$, this implies $\lambda_{obs} = 3000 - 9000\text{\AA}$. Because the majority of diagnostics lie at shorter wavelengths (e.g. OVI 1031, Ly α 1215, CII 1334, CIV 1550), high efficiency at bluer wavelengths is especially important.

To derive precise column density measurements and establish the gas kinematics, high spectral resolution is demanded. This program requires $R > 5000$ and, ideally, $R \gtrsim 10000$.

3.7.3 Sample selection

Targets will be drawn from the growing set of quasar pairs discovered from large-sky optical surveys (e.g. SDSS, 2DF). Extrapolating these data sets to future all-sky surveys (Pan-STARRS, LSST) suggest 500 targets with impact parameters less than 300 kpc and $g < 21$. Although one could, in principle, perform the science goals by using background galaxies located at small impact parameters from foreground quasars, there is a greater number of bright targets with quasar pairs.

3.7.4 Pre-imaging

All of the targets will have been discovered in complementary imaging/spectroscopic surveys (e.g. Pan-STARRS). No additional images will be necessary for this program.

3.7.5 Mask design

To derive the ionization state, metallicity, and kinematics of the gas, high-resolution observations are essential. We will observe using the MOBIE/ECH mode. In most cases it will not be possible to observe both members of the quasar pair (projected distances of $< 10''$) but we are primarily interested in high-resolution spectroscopy of the background target. It would, however, be advantageous to populate a mask with additional quasars in the field and/or bright galaxies with photometric redshifts $z > 2$.

3.7.6 Required integration time

To derive precise column densities (≈ 0.1 dex), one demands relatively high S/N when observing at $R \approx 10,000$. A good fiducial value is $S/N > 30$ per 10 km s^{-1} pixel. Using the ETC (v1.2) with a $0.5''$ slit ($R_{FWHM} = 11000$) in the ECH mode with a new moon and $V = 22$ mag, we calculate this S/N criterion is achieved for $\lambda \approx 4000 - 7000\text{\AA}$ in a 4hr total integration. A background $V = 21$ mag quasar, would require only 1hr integration.

3.7.7 Target acquisition

We would plan to use slit masks with guide star boxes for alignment.

3.7.8 Calibration data acquisition

This project has no requirements beyond standard calibrations.

3.7.9 Facility requirements

No special constraints.

3.8 Transients: Studying things that go bump in the night

3.8.1 Scientific Justification and Background

Impending and future synoptic surveys of the night sky (e.g. Pan-STARRS, LSST) are certain to reveal a diverse and exciting zoo of transient events. These will range from exploding massive stars at the edge of the universe to flaring low-mass stars in our local neighborhood. The synoptic surveys will provide colors and light curves of these phenomena, but are unlikely to establish the true nature of an event. Spectroscopy is critical to establish the origin and astrophysics of these phenomena. Because these surveys are at primarily optical pass-bands and one expects faint ($V > 25$) objects to dominate the event rate, an efficient optical spectrometer on a flexibly scheduled 30m-class telescope would lead in the discovery of previously unexplored, transient events. In addition to astronomical transient surveys, high-energy gamma-ray (e.g. HAWC), cosmic-ray, and gravitational-wave experiments (e.g. LIGO+) may record events with optical emission whose nature will only be established by MOBIE on TMT.

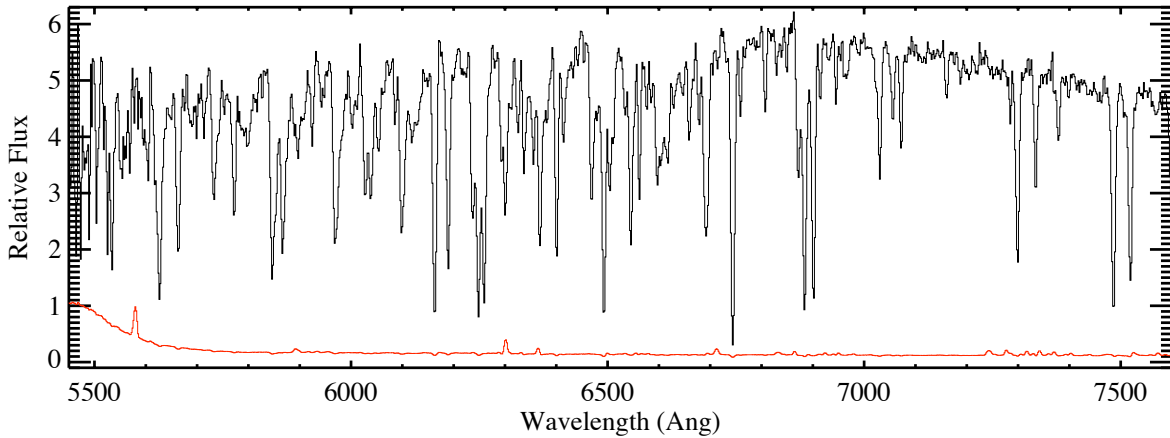


Figure 20: Keck/LRISr spectrum of a series of metal absorption lines, primarily related to gas in the host galaxy of a $z \sim 3$ GRB. This sightline has penetrated a molecular cloud within the host galaxy. These data show strong absorption from CO bandheads and the LRISb spectrum (not shown) reveals strong Lyman-Werner H_2 transitions. The astrophysical impact of these data is limited by the low-resolution; a sequence of high S/N observations with MOBIE/ECH would yield precise column densities (and kinematics) which establish the physical conditions of the gas (metallicity, depletion, molecular fraction, etc.) within the host galaxy.

The transients *du jour* are the gamma-ray bursts (GRBs). Although the optical afterglows of GRB were discovered with 2m-class telescopes (e.g. Castro-Tirado et al. 1997), the extragalactic nature and physical attributes were established through spectroscopy on the largest telescope of this era (Keck; Metzger et al. 1997). Today, 10m-class telescopes are providing high quality spectra of the optical afterglows from long-duration GRBs, these data correspond to a small fraction ($< 15\%$) of the GRBs detected. The majority of afterglows have optical magnitudes $R > 22$ after 1hr and observers generally acquire low-resolution, low S/N spectra which at best establish the redshift of the host galaxy. TMT+MOBIE would permit high resolution ($R \sim 8000 - 10,000$), high S/N observations for the majority of long-duration GRBs discovered. Presently, we await spectroscopic confirmation that the short-duration GRBs have extragalactic origin (Bloom et al. 2006). These GRBs exhibit much fainter optical afterglows and it is conceivable that this discovery awaits the next generation of ground-based facilities.

The prospect for new discoveries in transient science with TMT/MOBIE lie well beyond GRBs. There are predicted to be a host of exotic events (e.g. neutron star mergers, stars accreted onto black holes; Figure 21) that will emit at optical wavelengths and whose origin are encoded in the spectrum, not the light curve nor color of the phenomenon. The keys to observational success are threefold: (i) rapid response; (ii) high throughput; and (iii) wide spectral coverage. The MOBIE design achieves all of these goals and would be the premier instrument for transient spectroscopy on the TMT.

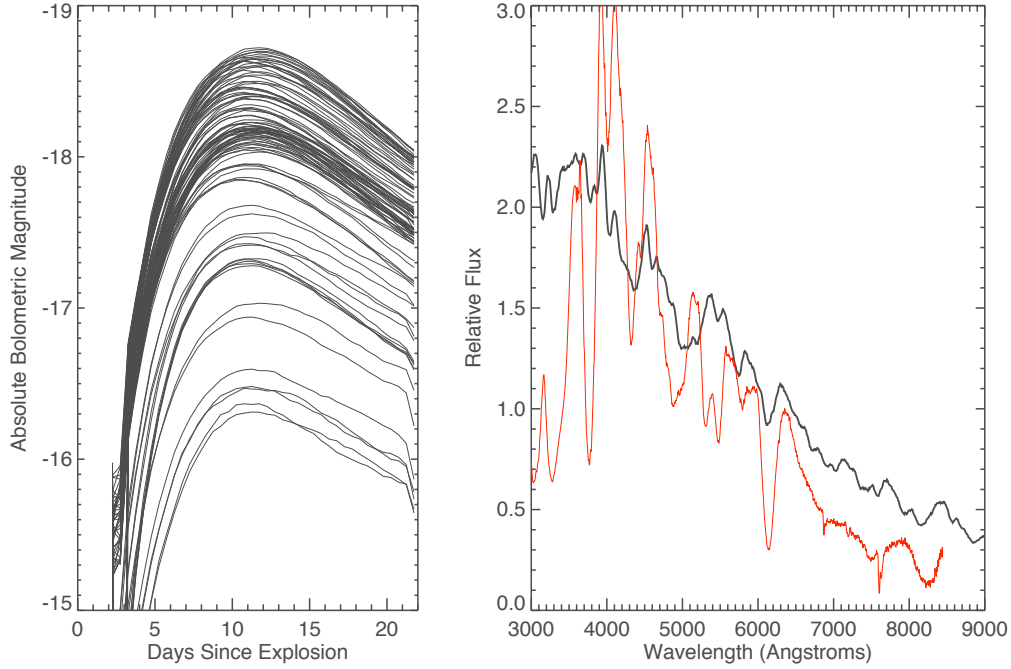


Figure 21: Predicted observables of a $0.6 M_{\odot}$ white dwarf which was tidally disrupted by a $500 M_{\odot}$ intermediate mass black hole. Left: Light curves of the highly asymmetric remnant as seen from various viewing angles. The emission is powered by radioactive isotopes synthesized in the disruption event. Right: Representative spectrum of the remnant near light curve peak, as compared to the spectrum of a Type Ia supernova (red line). Weak lines of silicon and iron are visible. far undetected transient.

3.8.2 Key observable

For faint and/or unknown transients, the key observable is a discovery spectrum to establish the nature and, hopefully, redshift of the event. For brighter targets, a high-resolution $R > 7,500$ spectrum will yield optical depth measurements to a precision of better than 0.1 dex that constrain the physical conditions in gas local to the event.

3.8.3 Sample selection

Targets will be drawn from the growing set of synoptic surveys, high-energy photon detectors, and gravitational-wave experiments. These include but are not limited to Pan-STARRS, LSST, PTF, SNAP, LIGO and HAWC. There will be no shortage of events in the TMT era.

3.8.4 Pre-imaging

It is possible, but unlikely, that TMT/MOBIE will be used to localize a transient event identified at another frequency (e.g. high-energy gamma-ray) or via gravitational-waves. This would only be an efficient use of the telescope for a signal already localized to better than $\approx 100 \text{ arcmin}^2$. A series of exposures may need to be taken to identify a new and variable source.

3.8.5 Mask design

It is likely that all of the targets would be observed through a longslit. To maximize transient science, which is generally performed on a target-of-opportunity basis, it would be ideal to maintain long-slit capability at all times.

Ideally, MOBIE would have a long-slit mode available at all times, with a number of choices of slit width and slit length so that one would have flexibility to match seeing conditions and/or vary the spectral resolution based on the nature of the event.

One would perform transient science using both $\mathcal{R} \simeq 1000$ and ECH spectral modes of MOBIE. Discovery spectra of the faintest transients would dictate the low-dispersion mode whereas ECH spectra of brighter targets would provide estimates of the physical conditions in the gas.

By their nature, transients are generally unknown sources with an unknown origin and distance. For this reason, wide wavelength coverage is essential. This is true for both the low-dispersion and ECH modes.

3.8.6 Required integration time

As noted above, one would pursue transient science using both modes of MOBIE. Consider the discovery space for spectroscopy afforded by TMT+MOBIE. Using the low-dispersion mode and $0.75''$ slit with $\text{FWHM}=0.7''$ seeing, a 1800s exposure on a $V = 24$ mag source will yield a spectrum with $S/N=4$ per 0.8\AA pixel (or $S/N = 9$ per resolution element). In general, this is more than sufficient to establish the nature and redshift of an object with modest spectral features. It would be reasonable to push to $V > 26$ for transients with strong spectral features. Regarding ECH observations, a 3600s exposure on a $V = 23$ mag source using the $0.75''$ slit will give a $S/N \approx 4$ per 8.3 km s^{-1} pixel at 7 days from new moon (ToO observations would be at all moon phases). This pushes nearly 3 mag deeper than what is and will be accomplished with echellette spectrometers on 10m-class telescopes.

3.8.7 Target acquisition

A slit viewing camera is highly desirable for fast acquisition of brighter targets ($V < 22$). For the faintest sources, one would acquire using offsets from a nearby star based on astrometry of previous imaging.

3.8.8 Calibration data acquisition

It is often important to disseminate new information (e.g. redshift) on transients quickly to the community so that other teams with other resources (e.g. Chandra) may trigger their own observations. To this end, one would desire either a suite of archived calibration files to perform or that the observatory provide a new set immediately to enable on-the-spot data reduction.

3.8.9 Facility requirements

For target-of-opportunity science, one would want ready access to MOBIE on every night. This would mean the occasional interruption of observing with other instrumentation. It also demands the ability to slew quickly to rapidly fading targets. At queue-based observatories, the staff are trained in the immediate acquisition of transient targets. Furthermore, procedures have been established to ‘sound alarms’ at the discovery of a new, time-critical transient event. A ToO program at TMT would benefit significantly from these modest investments.

4 General Calibration Procedures

4.1 Sky subtraction with MOBIE

TMT+MOBIE will obtain spectra of the faintest objects possible in the 0.31-1 μm optical window – some as much as 1000 times fainter than the sky background. As such, MOBIE must be optimized to allow extremely accurate background subtraction, which is required to be free of systematic errors. A number of post-observing techniques have been developed in the last several years to minimize the effects of systematic sky subtraction residuals (e.g., Kelson 2003); these techniques rely on producing sky spectra that are over-sampled spectrally compared with the data in a given row or column of the detector, and then this sky spectrum is expanded using accurate mapping of the wavelength solution into a two-dimensional model of the sky for each slit. Such techniques are quite effective in reducing residuals near bright night sky lines (quite relevant longward of 7300 \AA) but they must still interpolate the background in the spatial region occupied by the object on the slit, in the absence of spatial dithering, and are thus very sensitive to the quality of flat fielding, the smoothness of slit edges, changes in vignetting along a slit, etc.

The “cleanest” subtraction of background from two-dimensional spectra, in terms of realizing true photon-noise-limited results, come from fast beam-switching so that “object” and “sky” are recorded quasi-simultaneously on the same region of the detector and through virtually the same optical path. These techniques have been used for many years in IR astronomy, where the backgrounds are much higher, and vary much more rapidly, than at optical wavelengths. If the cadence of the beam-switching is shorter than the characteristic time for variation in the intensity of the background (experiments suggest that cadence of $\simeq 30$ seconds will see sky variations $\Delta\text{Sky}/\text{Sky} < 0.1\%$ at optical wavelengths), then simply subtracting the “background” spectrum from the “object” spectrum should achieve nearly perfect removal of the background. Simple differencing also removes the systematic effects on background removal of non-uniform slits, since the non-uniformities will be precisely the same for both (object+sky) and sky observations.

A solution that has been used successfully to achieve Poisson-limited background subtraction for spectroscopy is the so-called “Nod and Shuffle” technique (Glazebrook & Bland-Hawthorn 2001), which is essentially a method of beam-switching that gets around the problem of paying a read-noise penalty every 20-30 seconds. In Nod/Shuffle, rather than reading out the whole array on the timescale of the beam-switching, the shutter is briefly closed while the telescope is nodded to place either “sky” or “object+sky” onto a slit, and at the same time, the charge is shifted along the parallel direction, alternating between “frame storage” regions that are not being exposed. Thus, every 20-30 seconds, the charge associated with sky or object is moved back and forth to the active (i.e., exposed) region of the detector, with signal accumulating only when in the “active” region (which would therefore mean that exposure on target or on sky is only $\simeq 50\%$ of the elapsed time. This is the obvious disadvantage of Nod/Shuffle (ignoring problems associated with charge traps or diffusion)– one is spending half of the integration time on blank sky, and space on the detector must be reserved for frame storage, and thus is unavailable for science data.

One may clearly obtain all of the advantages of nod/shuffle without the disadvantages if it were possible to read out the detector on the timescale of the desired cadence without paying a significant read noise penalty and without a significant increase in time overhead. In this case, one would simply nod the telescope by a very small amount between exposures, to 2 or more positions on a slit, to accomplish the same background subtraction advantage without ever integrating on background only. With current detectors assumed (2k x 4k, 2 amplifiers per detector, 3e- read noise, 15 μm pixels) one would most likely bin 4x4 (0'21 per pixel in spatial direction) which would mean that with typical low-noise readout speed, the readout time could be as small as $\simeq 3$ seconds, with read noise per binned pixel < 1 e-. In low-dispersion mode, the expected TMT+MOBIE count rate from the sky at $\simeq 7000$ \AA would be ~ 0.6 e- s^{-1} pix^{-1} assuming 3 pixels per spectral resolution element, so that the background signal would be ~ 18 e- pix^{-1} after 30 seconds integration. If read noise < 1 e- pix^{-1} were realized, one could easily read the detector every 30 seconds with no noise penalty, and perhaps with no additional overhead other than the time to nod and settle. At $\mathcal{R} \sim 5000$ or greater, the count rate is lower by a factor $\gtrsim 5$, which would require longer individual integrations or still lower read noise to avoid a penalty. On the other hand, one may not require 0.1% background subtraction for objects observed in the higher dispersion modes.

During the Conceptual Design Phase, we will explore in more detail the various options for background subtraction; here we have shown that there should be multiple options to achieve the desired precision.

4.2 Geometric distortion

For multi-aperture spectroscopy with MOBIE it is important to determine the transformations needed to map sky coordinates to the wavefront sensor position, mask location, and the detector plane. These transformations are required for a number of reasons including: (a) the determination of slit positions from image data to facilitate mask design; (b) the correct calculation of telescope offsets from displacements measured at the guider/WFS and/or science detector to facilitate acquisition and (c) to ensure that the acquisition stars appear within the holes in the mask during the initial telescope pointing. The mask-detector transformation can be verified by taking images through each mask loaded in the mask changer and comparing the expected positions of the apertures with those predicted if the mask and its mounting were perfect (normally be a daytime operation). Efficient alignment of multi-slit masks will depend most critically on the mapping between the guider/WFS and the telescope (mask) focal surface, since initial alignment will use the guider position as a reference. The mapping from telescope focal surface to detector may be determined using a “grid of holes” mask deployed in the MOBIE mask changer, and verified by the observer in the course of obtaining afternoon calibration images. It is important primarily for the fine alignment stage, when the positions of alignment stars relative to alignment box centroids will be used to calculate offsets to PA and telescope position necessary to correctly align the slit mask.

4.3 Flat-field and bias

Flat-field observations calibrate the relative (pixel-to-pixel) response of the each pixel of the detector. The bias is taken with no light incident on the detector to determine the electronic bias level. For spectroscopy, it will be necessary to determine the flat-field correction with dispersed white light for each combination of mask, dichroic, and disperser so that each pixel receives light of the correct wavelength as it experiences in the on-target exposures. In this way, fringing effects can be removed (in the absence of instrument flexure). It also provides a more accurate calibration of the “slit function” provided that the illumination includes the telescope optics. Flat-field exposures will generally be taken during the daytime setup (with flexure compensation turned on); these would be taken using a script to automate the process, cycling through all of the spectrograph and mask configurations to be used during the night. A facility requirement imposed by the need for this calibration procedure is that the interior of the dome must contain a large screen (or at least an area with flat matte white paint-work) and an illumination lamp capable of producing sufficient flux at all wavelengths to which MOBIE is sensitive. Generally, internal illumination will not produce useful flat fields. In addition, for some applications (particularly at UV/blue wavelengths) the best flat fields will be obtained from the twilight sky (for imaging or spectroscopy). For spectroscopic twilight sky flats, the spectrograph must have a diffuser that will smooth over sharp spectral features. Ideally, twilight flats will be obtained at similar elevation and rotator position to the data to be obtained during the night. This would be made more easily achievable if there is a facility software tool that can “preview” these values given target coordinates and estimated time of observation. Since twilight sky time is limited, the ability to change configurations (mask, gratings, prisms) very rapidly will be essential.

Bias frames needed to remove reset pedestal in the visible-wavelength detectors will be constructed by median combining 20-30 zero-second bias frames. These will be obtained regularly during the afternoon using simple scripts. Dark current removal will be described below.

4.4 Wavelength calibration

For most programs, it should not be necessary to obtain wavelength calibration exposures during night-time observations. Generally these should be obtained using arc lamps internal to the spectrograph during the afternoon, for each configuration to be used during the night. The line lamps must provide sufficient density of lines to allow for very accurate two-dimensional wavelength solutions that are sometimes critical to accurate background subtraction. The lamps must provide a range of line density that will serve both the low-resolution and highest resolution modes of MOBIE, covering the full spectral range 0.3-1.0 μm . Wavelength calibrations should be obtained with the active flexure compensation system turned on.

Small zero-point shifts due to illumination changes or small amounts of flexure between calibration exposures and science data may be corrected using night sky emission or telluric absorption features in the science data. The best strategy for a given observation depends critically on the amount of instrument flexure.

4.5 Flux calibration

Flux calibration is needed for some programs to reduce spectra to a relative scale of flux density. For relative flux calibration, it is necessary to observe one or more spectrophotometric standard stars with the same instrumental configuration used for the science observations. The highest quality calibrations would involve stars observed at similar airmass on the same night as the science data to be calibrated, though the observatory should maintain a set of standard star observations (at regular intervals) in various modes as a means of tracking instrument performance. For many programs, a single observation during evening or morning twilight would suffice for approximate relative flux calibration. Even relative flux calibration for multi-slit masks will be challenging, due to blaze shifts and/or small amounts of vignetting resulting from variable field positions of slits. These variations may be calibrated relative to the “single object” or long-slit position using flat fields, if the calibration sources are sufficiently stable. Illumination through the telescope optics would be necessary for such calibrations.

4.6 Linearity

The linearity of the detectors should be verified by taking a series of exposures of a constant flux source at varying exposure times. A requirement on the MOBIE detectors and electronics is that linearity test exposures should not be required to be undertaken more often than a few times per year (i.e., any departures from linearity are stable and may be easily calibrated out).

4.7 Dark current

Dark current is assumed to have a negligible contribution to the total noise in typical MOBIE observations (< 0.01 e-/sec/pixel). The MOBIE shutter must be light-tight enough that dark exposures of up to 3600s may be taken to verify that this is the case.

4.8 Telluric absorption

Many spectroscopic observations require correction for telluric absorption. Such absorption corrections can be obtained from spectra of stars with known spectral type. For programs in which the telluric correction is critically important, observations of calibration stars at the same airmass as the object should bracket the observation of the object. These would have to be obtained using the single-object (long-slit) mode, and would use the same slit width (or narrower) used on the multi-slit mask. Transferring telluric corrections to multi-slit spectra from single-object mode calibration stars will depend on very accurate flat-fielding and on the consistency of image quality (line spread function) over the field, and as a function of wavelength. It may be necessary to convolve calibration spectra with empirically-determined line-spread functions that depend on mask position. To remove intrinsic stellar features the calibration star spectra should be divided by model atmospheres or observed spectra which have been convolved to the same resolution as the MOBIE data. These stellar feature corrected spectra can then be used to correct the object spectra for telluric absorption after convolution with the line-spread function appropriate to each object’s position in the field.

5 Additional Observing Modes for MOBIE

5.1 A Tunable Narrow-Band Filter for TMT/MOBIE

A capability of obtaining narrow-band images with the WFOS instrument is a stated “goal” (as opposed to a “requirement”) in the TMT SRDv17.5. Ideally, a tunable filter is inserted in the collimated beam (recall the MOBIE beam diameter is 300mm) of the instrument. A brief consideration of where a Fabry-Perot etalon might be inserted into either the blue or the red beam of MOBIE suggests that it may be installed in roughly the same location as the cross-dispersing prism used in the ECH mode of MOBIE. A F-P device has the advantage of being “tunable”, as described below. Although conventional narrow-band interference filters can be accommodated at the normal MOBIE filter position, such interference filters will be expensive (but not impossible) to produce. Further development of both the technical feasibility and the scientific application of narrow-band imaging will be pursued during the Conceptual Design phase. Here we briefly outline some applications of a tunable Fabry-Perot device for MOBIE.

5.1.1 Basic description of the tunable filter

This document assumes a conventional tunable filter based on a scanning Fabry-Perot etalon. There are other technologies for tunable filters but they are not explored here. Fabry-Perot etalons are a proven and low-risk technology. An etalon is specified completely by its finesse, which is the ratio of the wavelength spacing of its order peaks to the width of a single peak. The resolution of the etalon is simply the order multiplied by the finesse. The wavelength tuning of the etalon is obtained by gap-scanning. Most modern tunable filters push/pull the plates using piezo-electric transducers in a closed loop system with capacitive displacement sensors giving the needed feedback to keep the plates parallel. The plates have to be quite thick to avoid being distorted by the piezo-electric transducers, so the tunable filter can be quite heavy. A rough estimate is that a tunable filter for MOBIE would weigh a least 20 kg.

Here we assume an etalon with an effective finesse of 30, which is about the best that can be obtained. (Although textbooks imply that finesse is set only by reflectivity of the plates, in practice the finesse is really set by surface figure irregularities, a.k.a. “defect finesse”, and not the reflectivity of the coatings). When one allows for defects from coatings, obtaining a final effective finesse of 30 requires plates polished and coated to an accuracy of $\lambda/100$, which is challenging but quite possible.

5.1.2 Observing Scenario: The Topology of Reionization

Cantalupo, Porciano & Lilly (2008) have recently written an interesting paper which argues that one can directly map the neutral-hydrogen distribution during the epoch of re-ionization by mapping out $\text{Ly}\alpha$ radiation from the ionization front produced by a quasar at $z \sim 6.5$. This emission is extended and originates in the partially ionized intergalactic medium (IGM) before re-ionization is complete. The basic idea is illustrated in cartoon form in Figure 22. Note how the quasar’s ionization front (which can be several Mpc in size) illuminates the interface between the ionized and neutral Universes at the end of the epoch of re-ionization. As the ionization front impacts the neutral background a ‘skin’ of ionized emission occurs, which would appear as an extended low surface-brightness $\text{Ly}\alpha$ glow. Neutral bubbles illuminated by the ionization front would appear as holes in the background glow, giving the emission complex a swiss cheese-like structure.

5.1.3 Sample selection

Ideal candidates for these observations are bright quasars whose redshifts lie near the end of the epoch of re-ionization, at around $6 < z < 7$. Eight quasars with $z > 6.1$ are already known, over twenty additional targets are expected to emerge from the wide-deep component of the UKIDSS survey on UKIRT, and no doubt in the next few years additional candidates will emerge from other surveys. It seems fairly safe to assume that around fifty suitable candidates will be known by the time TMT is on the sky. However, not all quasars will be equally good candidates. The visibility of the ionization front is a fairly strong function of the hardness of the ionization spectrum, and the best quasars for this measurement are those whose ionizing spectra are hard. Also, since the ionization front is expanding into the neutral medium relativistically, older quasars provide better targets. Cantalupo et al. (2008) note:

“For instance, the [Ionization] front behind a bright QSO at $z \sim 6.5$ with t_Q [age] of 5 Myr appears at a proper distance of 1 Mpc. If the opening angle of the QSO emission cone is 45 degrees (with respect of the line of sight), the total projected area covered by the [Ionization] front will extend over $\sim 12 \text{ arcmin}^2$ (or 60 arcmin^2 if the quasar emits isotropically). Therefore, older QSOs provide a larger projected area for detecting the [Ionization] front emission and a better constraint on the properties of both the quasar emission and the surrounding IGM. Moreover, older and luminous QSOs produce HII bubbles that are larger than possible preexisting ionized regions generated from clustered star-forming galaxies.”

These authors summarize the relevant considerations using following approximate relation (good to an order of magnitude only) for the surface brightness in Lyman alpha from the ionization front, as a function of quasar age t_Q , spectral hardness α , initial neutral fraction x_{HI} , local overdensity δ , and ionizing rate \dot{N}_γ :

$$\begin{aligned} \text{SB}_{\text{Ly}\alpha} \sim 10^{-20} x_{\text{HI}}(1 + \delta)^{1/2} \left(\frac{t_Q}{10 \text{ Myr}^{-1}} \right)^{-1} \left(\frac{\dot{N}_\gamma}{10^{57} \text{ s}^{-1}} \right)^{1/3} \times \\ \times \left(\frac{1+z}{7.5} \right)^{-2} \text{ erg s}^{-1} \text{ cm}^{-2} \text{ arcsec}^{-2} \end{aligned} \quad (1)$$

By augmenting this with a sky surface brightness, and using an ETC to provide the flux limit as a function of integration time and spectral resolution, one can determine the signal-to-noise ratio for the observation.

5.1.4 Spectral Resolution

If negligibly small spectral leakage from multiple orders can be tolerated, then in order to be able to scan over the whole wavelength range of MOBIE with the reference list of echellete blocking filters the resolution of the etalon will be relatively low. As shown in Figure 23 the etalon must operate at a low order (say $m = 10$, corresponding to a resolution $R = 300$ with the finesse of 30 assumed here). However, for the present reference observation considerable spectral leakage can be tolerated, and the etalon can operate at higher order with higher resolution. In the present document we will assume $R = 3000$. If $R = 300$ is assumed instead then all integration time estimates in the next sub-section will need to be increased by a factor of three to reach similar signal-to-noise. To some extent this factor of three can then be gained back by having fewer scan steps (at the expense of velocity resolution).

5.1.5 Integration Time

As an example we now consider investigation of a system resembling the $z = 6.419$ SDSS quasar QSO J1148+ 5251. The trough in this system indicates an ionization front of diameter $\sim 5 \text{ Mpc}$ (physical). When projected onto the sky, emission structure is expected over scales of a few arcmin. On the basis of various arguments, Cantalupo et al. (2008) adopt the following parameters for this system, which can be inserted into the previous equation to estimate the surface brightness of the Ly α emission: $8 < t_Q < 30 \text{ Myr}$, $\alpha = -1.7$, $x_{\text{HI}} > 0.1$, and $\dot{N}_\gamma = 2 \times 10^{57} \text{ photon s}^{-1}$. The corresponding surface brightness in Ly α corresponds to $\sim 1 \times 10^{-20} \text{ erg s}^{-1} \text{ cm}^{-2} \text{ arcsec}^{-2}$. For this (admittedly rather optimistic) case, the authors calculate that a 40h integration with a long slit spectrograph on the VLT would yield a 7σ detection. Using the VLT as a reference and scaling from this to other instrumental configurations, and assuming Ly α falls in a region of low sky contamination (such as the atmospheric window around $0.9 \mu\text{m}$), Cantalupo et al. derive the following scaling equation for signal-to-noise:

$$\text{S/N} \sim 7 C_f \left(\frac{D}{8 \text{ m}} \right) \left(\frac{\zeta}{0.8} \right) \left(\frac{f}{0.25} \right)^{1/2} \left(\frac{\Delta_s}{3 \text{ \AA}} \right)^{-1/2} \left(\frac{T}{40 \text{ hr}} \right)^{1/2} \left(\frac{\Delta\Omega}{180 \text{ arcsec}^2} \right)^{1/2}. \quad (2)$$

In this equation C_f is the slit covering factor (i.e., the fraction of the slit where the Ly α emission is present), D is the telescope diameter, ζ the atmospheric transmission, f the system efficiency, Δ_s the spectral bin, T the integration time, and $\Delta\Omega$ the area of the sky covered by the slit. From this equation, using aperture alone, the TMT reduces the expected integration time (relative to the VLT) required to make a seven sigma detection from 40h to 3h, so in

fact a high-resolution slit spectrograph would do for a basic detection (in itself very interesting). The benefits of the tunable filter would be: (a) instead of merely detecting the extended $\text{Ly}\alpha$ signal in one cross-section it would allow the topology of the $\text{Ly}\alpha$ SB to be mapped, its topology to be explored, and the bubble size distribution determined; (b) by taking in the whole extended emitting region it would allow $\text{Ly}\alpha$ to fill the FOV, greatly increasing the covering fraction C_f above and improving the S/N of the detection (a potential huge win if, as is suspected, the case above is rather optimistic); (c) using $A-B$ spectral nodding (a technique being developed with F2T2 on Gemini/FlamingoesII)) systematic errors from sky removal could be minimized.

We conclude that integration times of a minimum of 3h are needed in the most optimistic case for a single scan step. Since several scan steps are likely to be desired (to probe the topology of the structure in the velocity direction) integration times on the order of at least 10h are likely to be needed.

5.1.6 Procedures during the day

Daytime calibration procedures would incorporate the following:

1. Taking a series (20-30 images) of short dark images and measure the rms frame to frame deviations for all pixels. Verify that system noise is nominal.
2. Taking short and long (1/2 full well) exposures of a constant flux source. Verify that well depth and linearity are nominal. Such data should be taken in non-dispersed mode.
3. Taking long dark exposure. Verify nominal dark current.
4. Establish/verify parallelism by using a narrow-band filter and a quartz lamp to mimic a monochromatic beam and center the Jacquinot spot of the etalon on the center of the detector.
5. Obtain flat field images at each scan setting.
6. Establish/verify the wavelength calibration by scanning over an arc lamp.

5.1.7 Procedures during twilight

No special twilight procedures necessary.

5.1.8 Target acquisition

No special acquisition procedures necessary.

5.1.9 Calibration data acquisition

It may be useful to scan over an atmospheric geocoronal emission line (purported to be a relatively stable sources of natural line emission) several times per night to assist in absolute flux calibration.

5.1.10 Facility requirements

An ample supply of laboratory-grade dry nitrogen, supplied at a constant temperature, would be useful for continuously flushing the gap in the etalon. This would minimize systematic variations in the gap optical path length from the changes in atmospheric pressure and temperature.

5.1.11 Options for a more versatile filter

Two options may be worth considering to accommodate observations that require high resolution ($R > 300$) without significant order leakage.

Option 1: Add a filter wheel with a set of filters with a narrower bandwidth. The etalon can then operate at much higher resolution without leakage, simply by using the etalon at a higher order with an appropriate blocker. Note

though that if one wants to operate the filter in both a low-resolution and high-resolution mode then it complicates the design somewhat because piezo-electric transducers will be required with large travel. Alternatively, a mechanical spacer might need to be inserted/removed to change from one mode to another.

Option 2: Another option is to use two etalons which operate in tandem. This also suppresses the wings of the filter transmission profile, which is a large advantage for a device intended for the infrared working in between bright OH lines. However, for a device working at visible wavelengths, unless one wants high resolution with essentially zero leakage over the full wavelength range of MOBIE, this option might be overkill. It certainly adds significant cost and complexity.

5.2 Image Slicer/Integral Field Unit

While no design effort has been directed toward investigating the option of placing an image slicer or integral field unit into MOBIE, there is nothing in the current design that prevents such a sub-system from being added (at the telescope focal surface) in the future.

5.3 Ground Layer Adaptive Optics

A number of the MOBIE science cases presented in this document would benefit from sharper images that may result over some or all of the MOBIE field if a GLAO system were implemented (see the previous WFOS-HIA OCDD document for a detailed discussion of the benefits of GLAO). While the GLAO implementation, should it ever occur, would most likely depend on an adaptive secondary mirror, there would have to be room near the telescope focal surface for additional wavefront sensors needed by GLAO. Since most of the telescope focal surface is unused by the current MOBIE optical design concept, there should be no obvious problem with adding GLAO “hooks” in the future.

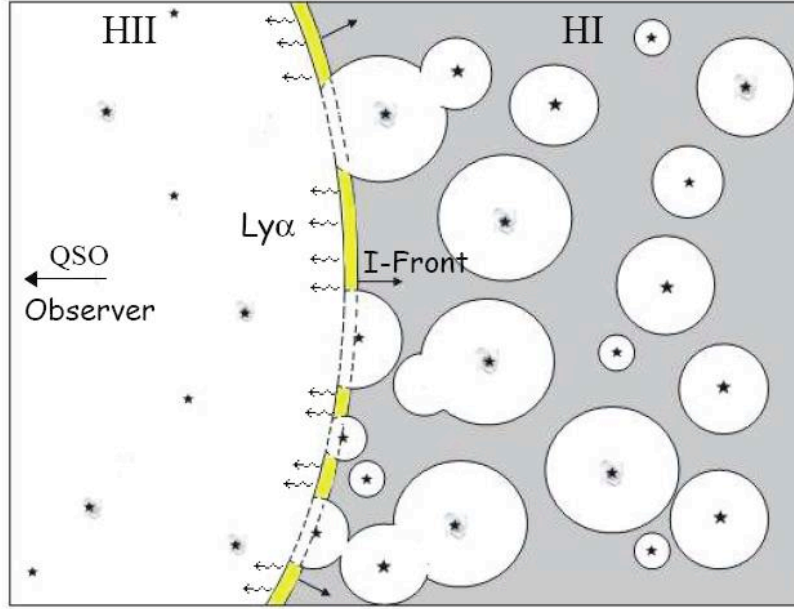


FIG. 2.—Schematic cartoon illustrates how to map the $H\text{ I}$ distribution using the $\text{Ly}\alpha$ emission from the I-front of a high- z QSO. The QSO and the observer are on the left side. The ionizing photons, in the plane of the figure, propagate from left to right and create an I-front wherever they encounter a partially neutral region. Within the I-front, the interactions between neutral hydrogen and the energetic electron released by photoionization produce $\text{Ly}\alpha$ photons via collisional excitation (*yellow stripes*). The $\text{Ly}\alpha$ emission escapes the I-front through the $H\text{ II}$ region in the direction of the observer. The regions already ionized by local sources (*bounded by the dashed lines*) do not produce $\text{Ly}\alpha$ via collisional excitations and will appear as holes in the two-dimensional $\text{Ly}\alpha$ map, similarly to a 21 cm tomography. This strictly applies to a young QSO with a relativistically expanding I-front. For older quasars, the entire boundary of the $H\text{ I}$ region can emit $\text{Ly}\alpha$ photons.

Figure 22: Cartoon illustration of the proposed measurement, taken from Cantalupo, Porciano & Lilly (2008), ApJ, 672, 48. As noted in the text, the ionization front observed (yellow region) will exhibit holes corresponding to ionized pockets of hydrogen embedded within the ambient neutral medium. The goal of the proposed observations is to measure the size distribution and topology of these ionized regions.

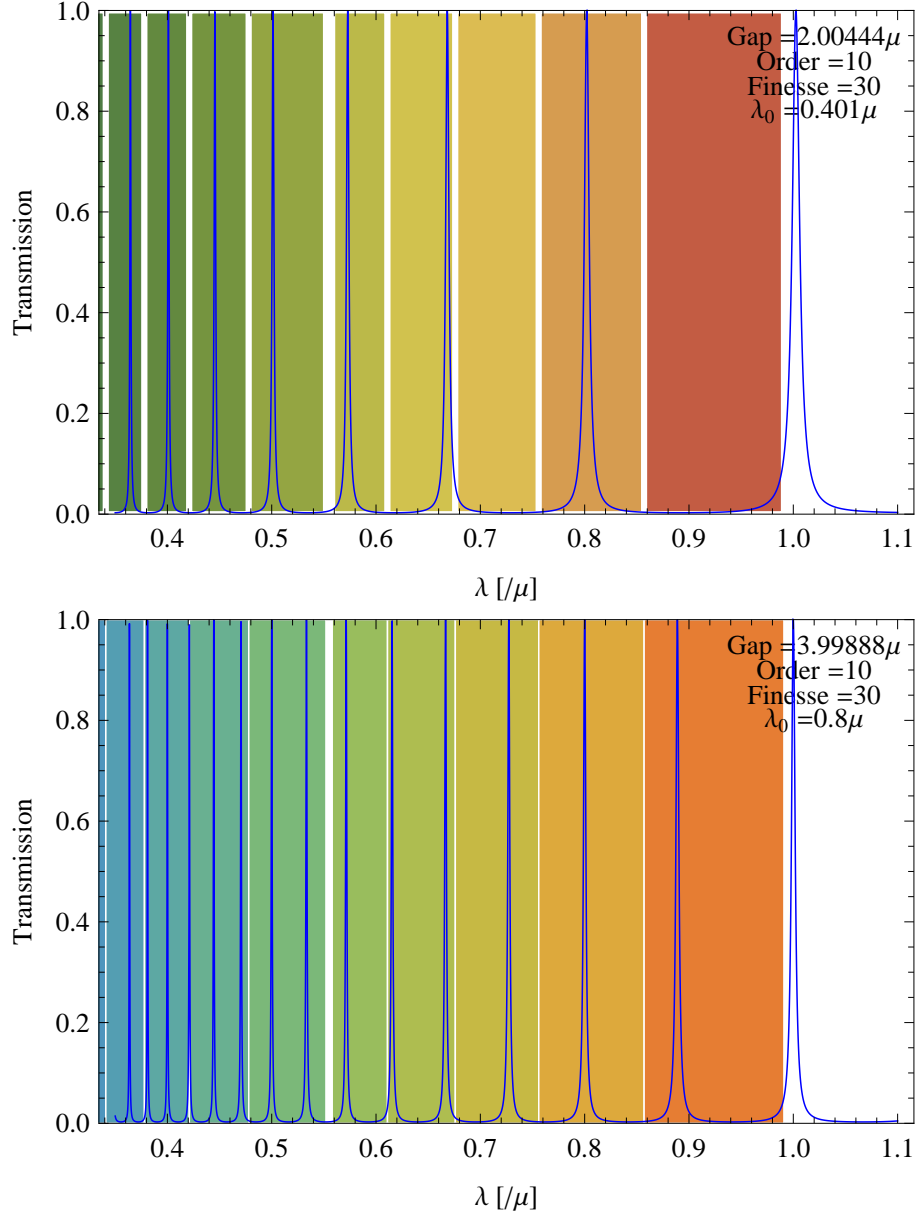


Figure 23: (Top) Tunable filter transmission profile (solid blue line) for an etalon with a finesse of 30 superposed on the reference filter specifications (colored bands) for an etalon operating at 10th order at 401nm. (Bottom) As for the top figure, except for an etalon operating at 10th order at 901nm. In both cases the spectral resolution is 300. The physical gap range spanned by the plates in moving from the top figure to the bottom figure is about 2 μ m.

6 Summary

Table 7 presents a flow-down summary of the science requirements contained within this document.

Table 7: Flow-down of Science Case Requirements

	White dwarfs	Metal Poor Stars	Resolved populations	Dark matter mapping	IGM Tomography I	IGM Tomography II	$z \sim 2 - 5$ Galaxies	QSO Pairs	Transients
Slits/mask	140	< 10	140	140	20	90	20	20	1
Masks/night	2	5	2.5,7	6	2	10	2	3	–
Slit width [arcsec]	0.6	0.75	0.8	0.75	0.75-1.0	0.75-1.0	0.75	0.75	0.75
Typical integration time/exposure [s]	1800	1200	1200	1800	1800	1800	1800	1800	1800
Typical integration time/mask [ks]	15	7.2	9,3	3.6	14.4	3.6	14.4	14.4	3.6
Resolution (blue/red)	2000	8000	8000	2000/5000	5000	1000	5000	8000	1000-8000
Minimum wavelength (blue/red) [nm]	340	380/550	370/830	310/550	310/550	310/550	310/550	310/550	310/550
Maximum wavelength (blue/red) [nm]	550	550/800	550/900	550/900	550/750	550/800	550/1000	550/1000	550/1000
ECH mode needed?	✓	✓	✓	✓	✓		✓	✓	✓
Need very precise flux calibration?				✓					
Needs very precise sky subtraction?			✓	✓	✓	✓			
Uses blue and red arms at same time?		✓	✓	✓	✓	✓	✓	✓	✓

7 References

- Abraham, R.G., et al. 2004, *Aj*, 127, 2455
Adelberger, K.L. 2004, *ApJ*, 612, 706
Adelberger, K.L., & Steidel, C.C 2000, *ApJ*, 544, 218.
Adelberger, K.L. et al. 2005, *ApJ*, 619, 697
Allam et al. 2007, *ApJ*, 662, 51.
Bedin, L. et al. 2005, *ApJL*, 624, 45
Belokurov et al. 2007, *ApJL*, 671, 9.
Belokurov, V., Zucker, D. B., Evans, N. W., et al, 2006, *ApJ*, 654, 897
Bergeron, P., Ruiz, M., & Leggett, S. 1997, *ApJS*, 108, 339
Bergeron, P., Wesemael, F., & Beauchamp, A. 1995, *PASP*, 107, 1047
Bergeron, P., Saffer, R., & Liebert, J. 1992, *ApJ*, 394, 228
Bloom et al. 2006, *ApJ*, 638, 354
Bouwens et al. 2007, *ApJ*, 670, 928.
Brinchmann et al. 2008, *MNRAS*, 385, 769.
Bunker, A.J., Stanway, E.R., Ellis, R.S., & McMahon, R.G. 2004, *MNRAS*, 355, 374
Bullock, J.S., Kravtsov, A.V., & Weinberg, D.H. 2001, *ApJ*, 548, 33
Bullock, J.S., & Johnston, K.V. 2005, *ApJ*, submitted. (astro-ph/0506467)
Castro-Tirado et al. 1997, *Science*, 279, 1011
Cen, R. 2003, *ApJ*, 591, 12
Choi, P.I., Guhathakurta, P., & Johnston, K.V. 2002, *AJ*, 124, 310
Côté, P., Oke, J.B., & Cohen, J.G. 1999, *AJ*, 118, 1645
Côté, P., et al. 2001, *ApJ*, 559, 828
Côté, P., McLaughlin, D.E., Cohen, J.G., & Blakeslee, J.P. 2003, *ApJ*, 591, 850
Daddi et al. 2004, *ApJ*, 617, 746.
Dave, R. 2008, *MNRAS*, 385, 147.
D’Antona, F. 2001, *IAU Symposium Series*, Extragalactic Star Clusters, 207
Ellison, S.L., et al. 1999, *PASP*, 111, 946
Erb, D.K., et al. 2006, *ApJ*, 646, 107
Fardal, M.A., Babul, A., Guhathakurta, P., Gilbert, K.M. & Dodge, C., 2008, *ApJL*, 682, L33
Ferguson, A.M.N., Irwin, M.J., Ibata, R.A., Lewis, G.F., & Tanvir, N.R. 2002, *AJ*, 124, 1452
Font, A.S., Johnston, K.V., Bullock, J.S., & Robertson, B. 2005, *ApJ*, submitted. (astro-ph/0507114)
Geha, M.C., Guhathakurta, P., Rich, R.M., & Cooper, M.C. 2005, *AJ*, in preparation
Gilbert, K.M. et al, 2007, *ApJ*,
Glazebrook, K., & Bland-Hawthorn, J. 2001, *PASP*, 113, 197
Guhathakurta, P., et al. 2005, *Nature*, submitted. (astro-ph/0502366)
Guhathakurta, P., et al. 2005, *AJ*, submitted. (astro-ph/0406145)
Hansen, B. et al. 2004, *ApJS*, 155, 551
Hansen, B. et al. 2002, *ApJL*, 574, 155
Hennawi et al. 2006, *ApJ*, 651, 61
Ibata, R., et al. 2004, *MNRAS*, 351, 117
Kalirai, J. et al. 2005a, *ApJL*, 618, 123
Kalirai, J. et al. 2005b, *ApJL*, 618, 129
Kalirai, J. et al. 2001b, *AJ*, 122, 3239
Kalirai, J. et al. 2001a, *AJ*, 122, 257
Kelson, D. 2003, *PASP*, 115, 688
Kirby, E.N., Guhathakurta, P. & Sneden, C., 2008, *ApJ*, 682, 1217
Kleinman, S. et al. 2004, *ApJ*, 607, 426
Koposov, S., Belokurov, V., Evans, N. W., et al, 2008, *ApJ*, 686, 279
Krauss, L. & Chaboyer, B. 2003, *Science*, 299, 5603, 65
Leitherer et al. 2001, *ApJ*, 550, 724.

Merritt, D., & Tremblay, B. 1993, *AJ*, 106, 2229
 Metzger et al. 1997, *Nature*, 387, 879
 Monelli, M. et al. 2005, *ApJL*, 621, 117
 Nagashima et al. 2005, *MNRAS*, 358, 1247.
 Napolitano, N.R., et al. 2005, *MNRAS*, 357, 691
 Papovich et al. 2001, *ApJ*, 559, 620.
 Peng, E.W., Ford, H.C., & Freeman, K.C. 2004, *ApJ*, 602, 705
 Pettini, M., et al. 2002, *ApJ*, 569, 742
 Pettini et al. 2000, *ApJ*, 528, 96.
 Pettini et al. 2002, *ApJ*, 569, 742.
 Porciani et al. 2004, *MNRAS*, 355, 1010
 Prochaska & Hennawi 2008, arXiv:0806.0862
 Reddy, N.A. et al. 2006, *ApJ*, 644, 792.
 Reddy, N.A. et al 2008, *ApJS*, 175, 48
 Reitzel, D.B., & Guhathakurta, P. 2002, *AJ*, 124, 234
 Reitzel, D.B., Guhathakurta, P., & Rich, R.M. 2004, *AJ*, 127, 2133
 Richer, H. et al. 2004, *AJ*, 127, 2771
 Richtler, T., et al. 2003, *AJ*, 127, 2094
 Rix, S.M. et al. 2004, *ApJ*, 615, 98.
 Rhoads, J.E., et al. 2003, *AJ*, 125, 1006
 Romano-Diaz, E., Shlosman, I., Hoffman, Y. & Heller, C., 2008, *ApJ*, in press
 Rubin, K., Williams, K.A., Bolte, M. & Koester, D., 2008, *AJ*, 135, 2163
 Schiavon, R.P., & Barbuy, B. 1999, *ApJ*, 510, 934
 Seitz et al. 1998, *MNRAS*, 298, 945.
 Shapley et al. 2003, *ApJ*, 588, 65
 Smail et al. 2007, *ApJL*, 654, 33.
 Somerville, R. & Primack, J. 1999, *MNRAS*, 310, 1087
 Steidel et al. 1999, *ApJ*, 519, 1
 Steidel et al. 2003, *ApJ*, 592, 728
 Steidel, et al. 2004, *ApJ*, 604, 534
 van den Bergh, S. & Tammann, G. 1991, *ARA&A*, 29, 363
 Verhamme, A. et al. 2006, *A&A*, 460, 397
 Weidemann, V. 2000, *A&A*, 363, 647
 Williams, K.A., Bolte, M. & Koester, D., 2008, *ApJ*, in press (astro-ph/0811.1577)
 Yan, H., & Windhorst, R.A. 2004, *ApJ*, 600, L1